学位論文

Stacking image analysis of SDSS galaxies in far-infrared and its implications for the Galactic extinction map

(遠赤外領域におけるSDSS銀河のスタック解析と
銀河系減光地図への示唆)

平成26年12月　博士（理学）申請

東京大学大学院理学系研究科
物理学専攻

柏木　俊哉

Abstract

The Galactic extinction map is the most fundamental data in extragalactic astronomy. Since the Galactic dust scatters and absorbs extragalactic light in ultra-violet to near-infrared regimes, one cannot measure any fundamental quantities such as fluxes or colors of extragalactic objects unless the dust extinction is properly corrected for.

The most widely-used Galactic extinction map was constructed by Schlegel, Finkbeiner, & Davis (1998), on the basis of far-infrared (FIR) emission map. Nevertheless, the number count analysis of SDSS DR4 (Sloan Digital Sky Survey Fourth Data Release) galaxies by Yahata et al. (2007) exhibited the anomalous *positive* correlation between the surface number densities of galaxies and the SFD extinction, indicating the existence of unknown systematics in the SFD map. They argued that the origin of the anomaly is due to the FIR emission from galaxies contaminated in the SFD map.

The first question addressed in this thesis is the anomaly in the SFD map. We ask if the observed anomaly is quantitatively explained by the hypothesis of the FIR contamination of galaxies, which was first proposed by Yahata et al. (2007). We present the stacking image analysis of SDSS DR7 galaxies on the SFD map. The stacking analysis directly detect the FIR emission of galaxies contaminated in the SFD map, of the order of 0.1 to 1 mmag in the r-band extinction. We next model the effect of the FIR contamination on the surface number densities of galaxies both numerically and analytically, and compare the model predictions with the observed anomaly. We find that the amount of FIR emission required to reproduce the observed surface number densities is in reasonable agreement with that measured by the stacking analysis. Thus we conclude that the FIR contamination of galaxies quantitatively explains the anomaly in the SFD map. Nevertheless, our attempt to correct the SFD map for the FIR contamination by subtracting the average FIR emission of SDSS galaxies does not remove the anomaly well. This is possibly due to the dependence of the FIR emission on the morphology of galaxies, which is neglected in our present model.

The other question addressed in this thesis is the spatial extent of dust around galaxies. Since dust grains are produced through stellar activities, they are conventionally thought to be confined in the interstellar space of galaxies. A recent measurement by Ménard et al. (2010a, MSFR), however, found that the dust reddening profile around SDSS galaxies extends up to few Mpc, far beyond the typical scale of galactic disks. Thus the measurement of MSFR may appear to suggest the existence of the dust smoothly filling the intergalactic space. In the last part of this thesis, we measure the FIR emission profile of the same galaxy sample as MSFR using the stacking analysis. Combined with the reddening measurement by MSFR, the dust emission to extinction ratio provides a constraint on the dust temperature as $\sim 18 \pm 1$K, which is similar to that of typical interstellar dust. Therefore the extended dust claimed by MSFR is equally explained by the statistical sum of interstellar dust due to spacial clustering of galaxies, at least, from the point of view of the dust temperature. While this result may be supporting our hypothesis, the uncertainties in our constraint need to be further investigated, given several simplification and assumptions that we adopted.

Contents

Chapter 1

Introduction

All extragalactic observations are conducted through the Galactic foregrounds. Since extragalactic light in ultra-violet to near-infrared regimes is dimmed due to the absorption and scattering by the Galactic dust, which is called dust extinction, we cannot measure any fundamental quantities of extragalactic objects, such as their fluxes or colors, unless the dust extinction is accurately corrected for. This is why the Galactic extinction map is one of the most fundamental data throughout the entire fields of astronomy. The dust extinction has been the major source of the systematics in interpreting observational data, and the accuracy of the Galactic extinction map becomes more critical as higher precision is achieved by continuous progress in observational instruments.

Schlegel, Finkbeiner, & Davis (1998, SFD) constructed the Galactic extinction map, which is the most successful and widely-used Galactic extinction map at present. The SFD map is based on the all-sky far-infrared (FIR) data provided by IRAS/ISSA (Infrared Astronomical Satellite/IRAS Sky Survey Atlas) and COBE/DIRBE (Cosmic Background Explorer/Diffuse Infrared Background Experiment). They estimated the Galactic dust extinction assuming the proportionality between the FIR emission and the optical depth of the Galactic dust, and achieved the significant improvements in accuracy and angular resolution relative to the previous extinction map using the HI 21cm flux map (Burstein & Heiles, 1978, 1982, BH map). Nevertheless, it should be noted that the SFD map is not based on any direct measurement of dust extinction, but derived from its emission. Since the FIR emission is converted into the dust extinction relying on several assumptions, the SFD map may suffer from systematic errors if the assumptions are not justified. Therefore the validity of the SFD map must be independently tested by comparison with other observations.

This motivated Yahata et al. (2007) to test the SFD map using the number count analysis of galaxies. They used the photometric galaxies from SDSS DR4 (Sloan Digital Sky Survey Fourth Data Release) and tested the SFD map in low extinction regions. They computed the surface number densities of the SDSS galaxies as a function of the SFD extinction, with/without extinction correction with the SFD map. As a result, they found that the surface number densities exhibit anomalous positive correlation with the SFD dust extinction, in particular, where the r-band extinction is less than 0.1 mag. This is precisely opposite to the expected effect due to the Galactic dust, indicating the presence of unknown systematic errors in the SFD map.

The origin of the anomaly may be attributed to unknown component of Galactic dust that is not traced by the FIR emission. Yahata et al. (2007) did not find, however,

any signature of such a component even in the HI 21cm flux map. Furthermore, they found that the anomalous correlation between the surface number densities and the SFD extinction becomes weaker for more distant spectroscopic galaxies, and quite small for distant quasars ($1 < z < 2$). If the hypothetical component of Galactic dust exists, it should also affect these distant objects as the same as the nearby galaxies. Therefore they concluded that this explanation is not plausible.

In fact, Yahata et al. (2007) proposed a hypothesis that the SFD map is contaminated by the FIR emission from the SDSS galaxies themselves. The SFD extinction was estimated by assuming that it is proportional to the FIR emission. Therefore the positive correlation between the surface number densities of galaxies and the SFD extinction may be ascribed to the intrinsic correlation between the number of galaxies and their FIR emission.

The systematic errors in the SFD map due to the FIR contamination of galaxies are likely to be small, and it appears unlikely that the contamination substantially affects observations targeting individual extragalactic object. Since the contaminated FIR emission of galaxies are correlated with spatial distribution and clustering of galaxies, however, these systematics potentially bias cosmological data in a statistical fashion. Therefore, we further investigate the problem of FIR contamination in Chapter 4 and 5 of this thesis.

The Galactic dust may be not the only source responsible for the dust extinction of extragalactic lights, if the intergalactic space is smoothly filled with dust ejected from the interstellar space of galaxies. Since the optical depth of such intergalactic dust, if it exists, should be increasing with redshift, it would systematically affect the measurements of distant objects and their cosmological implications (Aguirre, 1999; Ménard et al., 2010b; Fang et al., 2011). The spatial distribution of dust itself is of fundamental importance in understanding the star formation and metal circulation history in the universe. Therefore, ever since Zwicky (1962) suggested the existence of dust filling the intracluster within the Coma cluster, many earlier studies investigated the abundance and spatial distribution of dust in different environments.

Recently, Ménard et al. (2010a, MSFR) investigated the distribution of dust around galaxies by measuring the angular correlation between SDSS galaxy distribution and distant quasar colors. They found that the mean reddening profile around the foreground galaxies is well described by a single power-law and, surprisingly, it extends up to a few Mpc from the galaxies. This is far beyond the typical scale of galactic disks, and even larger than the virial radius of typical galaxy clusters.

The MSFR measurement may be interpreted as evidence of intergalactic dust component, which is smoothly surrounding an individual foreground galaxy. The interpretation, however, is rather subtle. The power-law index of the mean reddening profile from their measurement is close to that of the angular correlation function of galaxies. Thus the detected dust reddening may be equally explained by the summation of the dust component associated with the central part of galaxies according to the spatial clustering of those galaxies. In practical, it is rather difficult to distinguish between these interpretation on the basis of the statistical correlation analysis as performed by MSFR. Therefore a complementary and independent methodology to constrain the nature of the dust is needed. This is exactly what we attempt to propose in Chapter 6.

The present thesis is organized as follows.

- Chapter 2 summarizes the definition of dust extinction and derives the basic relations between the dust emission and extinction.

- Chapter 3 presents the procedures of constructing the SFD map and previous studies testing the reliability of the SFD map, with the emphasis on the first discovery of the anomaly by Yahata et al. (2007).

- In Chapter 4, we perform the stacking analysis of the SFD map on the SDSS galaxies and directly detect and measure the FIR contamination due to the SDSS galaxies. This chapter is based on Kashiwagi, Yahata, & Suto (2013).

- Chapter 5 confirms the anomaly of the SFD map using updated SDSS DR7 data set. We numerically and analytically model the effect of the FIR contamination in the SFD map on the surface density of the galaxies. We evaluate the required amount of FIR contamination in order to reproduce the observed anomaly, and discuss its consistency with the FIR emission signals detected by the stacking analysis. We also discuss the future directions for correcting the SFD map for FIR contamination, and prospects for application of the upcoming data by AKARI satellite. This chapter is based on Kashiwagi et al. (2015).

- Chapter 6 applies the stacking analysis above for the galaxy sample as the same as MSFR. Combining the detected FIR emission with the corresponding dust extinction measured by MSFR, we put the constraints on the dust temperature, which would provide complementary information for the interpretation of the MSFR measurement. This chapter is based on Kashiwagi & Suto (2015).

- Chapter 7 is devoted to the summary and conclusion of this thesis.

Chapter 2

Galactic extinction

2.1 Galactic extinction and extinction curve

Light from extragalactic sources is dimmed due to scattering and absorption by dust grains in the Galactic interstellar medium (ISM), which is called dust extinction. The amount of dust extinction is defined in terms of the intrinsic and observed intensity of sources, $I_{\rm int}(\lambda)$ and $I_{\rm obs}(\lambda)$, as

$$A(\lambda) \equiv -2.5 \log_{10} \left[\frac{I_{\rm obs}(\lambda)}{I_{\rm int}(\lambda)} \right] \tag{2.1}$$

Since $I_{\rm int}(\lambda)$ and $I_{\rm obs}(\lambda)$ are related to the dust optical depth, $\tau(\lambda)$, as

$$I_{\rm obs}(\lambda) = I_{\rm int}(\lambda) e^{-\tau(\lambda)}, \tag{2.2}$$

$A(\lambda)$ is simply proportional to $\tau(\lambda)$:

$$A(\lambda) = \frac{2.5}{\ln 10} \tau(\lambda). \tag{2.3}$$

For photometric observations, the dust extinction at passband X is given as

$$A_X = -2.5 \log_{10} \left[\frac{\int d\lambda W_X(\lambda) S(\lambda) e^{-\tau(\lambda)}}{\int d\lambda W_X(\lambda) S(\lambda)} \right], \tag{2.4}$$

where $W_X(\lambda)$ is the response function of the X passband and $S(\lambda)$ denotes the spectral energy distribution (SED) of the observed source per unit wavelength. The observed and intrinsic magnitudes of objects, $m_{X,\rm obs}$ and $m_{X,\rm int}$, are then related as

$$m_{X,\rm obs} = m_{X,\rm int} + A_X. \tag{2.5}$$

The wavelength dependence of the extinction is referred to as extinction curve, or equivalently reddening law, and conventionally defined as

$$k(\lambda) = \frac{A(\lambda)}{A_V}, \tag{2.6}$$

normalized by V-band extinction, A_V. The extinction curve depends on optical properties of dust grains in a complicated fashion as we see in the following subsections. For the

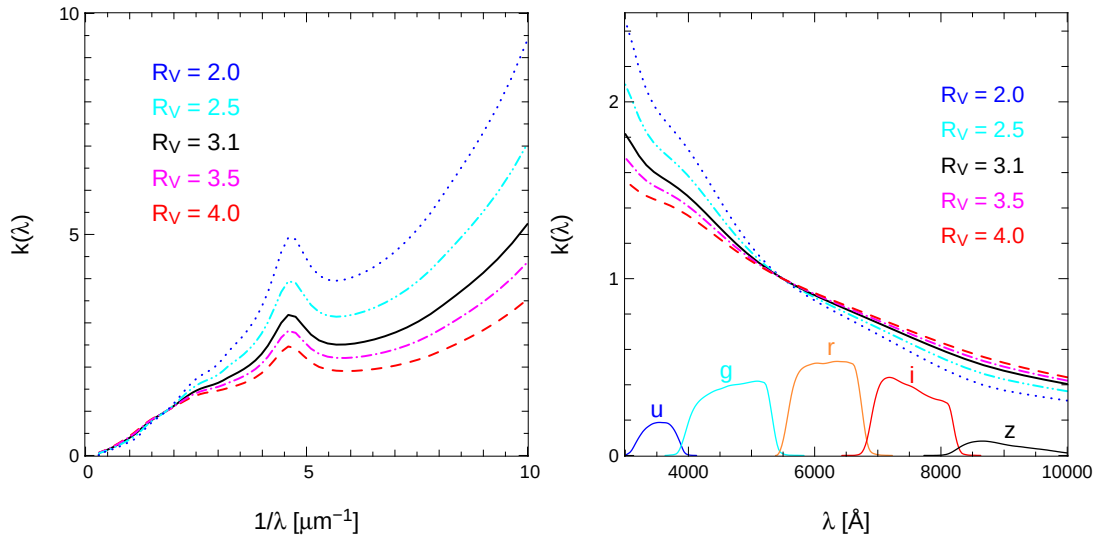

Figure 2.1: Extinction curves of the Galactic dust for $R_V = 2.0, 2.5, 3.1, 3.5$, and 4.0 for $1/\lambda < 10\mu\mathrm{m}^{-1}$ (*left panel*) and optical regime (3000Å $< \lambda <$ 10000Å, *right panel*). The fitting function provided by Cardelli et al. (1989) is adopted. For reference, the response functions of SDSS are shown at the bottom of *right panel* for u, g, r, i, and z-band, where the vertical scale is arbitrary.

Galactic extinction, however, it is empirically known that $k(\lambda)$ is well characterized by a single parameter,

$$R_V \equiv \frac{A_V}{E(B-V)}, \tag{2.7}$$

where $E(B-V) \equiv A_B - A_V$ is the color excess. The Galactic dust in diffuse interstellar medium typically has $R_V \simeq 3.1$, whereas R_V varies and tends to be larger for denser molecular clouds. The l.h.s of equation (2.6) is well approximated by

$$k(x) = a(x) + \frac{b(x)}{R_V}, \tag{2.8}$$

where $a(x)$ and $b(x)$ is the polynomial fitting functions obtained by several studies (Fitzpatrick, 1999; Cardelli et al., 1989; O'Donnell, 1994) in terms of $x \equiv 1/\lambda$ [$\mu\mathrm{m}^{-1}$]. One example of the fitting functions of the extinction curve by Cardelli et al. (1989) is shown in Figure 2.1. The dust extinction is larger for shorter wavelengths, thus the corresponding colors becomes redder (dust reddening).

It is known that the dust and cool gas in ISM are well mixed, thus the dust extinction is approximated as proportional to the hydrogen column density:

$$\frac{N_{\mathrm{H}}}{E(B-V)} = 5.8 \times 10^{21} \mathrm{cm}^{-2}\mathrm{mag}^{-1}, \tag{2.9}$$

where N_{H} denotes the column number density including both HI and molecular hydrogen (Bohlin, Savage, & Drake, 1978). Similarly, Burstein & Heiles (1982) used the HI column density map as the tracer of the dust color excess. If an extinction curve is given, the color excess can be converted into dust extinction at each wavelength.

2.2 Scattering and absorption by dust particles

Consider the source at a distance r with intensity $I(\lambda, r)$. If the dust consists of a single chemical component and has fixed grain size, the increment of the intensity, dI, due to the scattering and absorption by the dust grains is given as

$$\begin{aligned} dI(\lambda, r) &= -I(\lambda, r) n_d(r) C_{\rm sca}(\lambda) dr \\ &\quad -I(\lambda, r) n_d(r) C_{\rm abs}(\lambda) dr \\ &\quad +B[\lambda, T(r)] n_d(r) C_{\rm abs}(\lambda) dr, \end{aligned} \tag{2.10}$$

where $C_{\rm sca}$ and $C_{\rm abs}$ are the scattering and absorption cross sections of dust grains, and $n_d(r)$ is the number density of the grains. The first and second terms in the r.h.s of equation (2.10) represent the decrement of light due to scattering and absorption by dust. The third term denotes the thermal radiation of dust grains themselves given by the blackbody spectrum of equilibrium temperature T but modified by $C_{\rm abs}$. Here we neglect the contribution of light that is scattered into the line of sight from different directions. Since both scattering and absorption by dust grains decrease the light coming along the line of sight, thus cause extinction, the extinction cross sections is defined as

$$C_{\rm ext}(\lambda) \equiv C_{\rm sca}(\lambda) + C_{\rm abs}(\lambda). \tag{2.11}$$

In reality, the dust grains have a variety of chemical composition and broad size distribution. In this case, for the given dust composition, equation (2.10) should be replaced by

$$dI(\lambda, r) = -I(\lambda, r) \frac{d\tau_{\rm sca}(\lambda)}{dr} dr - I(\lambda, r) \frac{d\tau_{\rm abs}(\lambda)}{dr} dr + B[\lambda, T(r)] \frac{d\tau_{\rm abs}(\lambda)}{dr} dr, \tag{2.12}$$

where

$$\frac{d\tau_{\rm sca}(\lambda)}{dr} = \sum_i \int da \frac{dn_i}{da} C_{{\rm sca},i}(\lambda, a) \tag{2.13}$$

$$\frac{d\tau_{\rm abs}(\lambda)}{dr} = \sum_i \int da \frac{dn_i}{da} C_{{\rm abs},i}(\lambda, a), \tag{2.14}$$

$C_{{\rm sca},i}(\lambda, a)$ and $C_{{\rm abs},i}(\lambda, a)$ are the scattering and absorption cross sections for the i-th component of dust grains with a radius a, and dn_i/da denotes the differential number density as a function of a.

For spherical grains, the scatter and absorption cross sections are given by the Mie theory (Mie, 1908; van de Hulst, 1957). Basically, they are calculated by solving the propagation of electromagnetic plane waves following the Maxwell equations with the boundary condition on the surface of grain. The solution is given in terms of the efficiency factors, which are given as the sum of series expansion:

$$Q_{\rm ext}(x) \equiv \frac{C_{\rm ext}}{\pi a^2} = \frac{2}{x^2} \sum_{n=1}^{\infty} (2n+1) \cdot {\rm Re}(a_n + b_n), \tag{2.15}$$

$$Q_{\rm sca}(x) \equiv \frac{C_{\rm sca}}{\pi a^2} = \frac{2}{x^2} \sum_{n=1}^{\infty} (2n+1) \cdot \left[|a_n|^2 + |b_n|^2 \right], \tag{2.16}$$

$$Q_{\rm abs}(x) = Q_{\rm ext}(x) - Q_{\rm sca}(x), \tag{2.17}$$

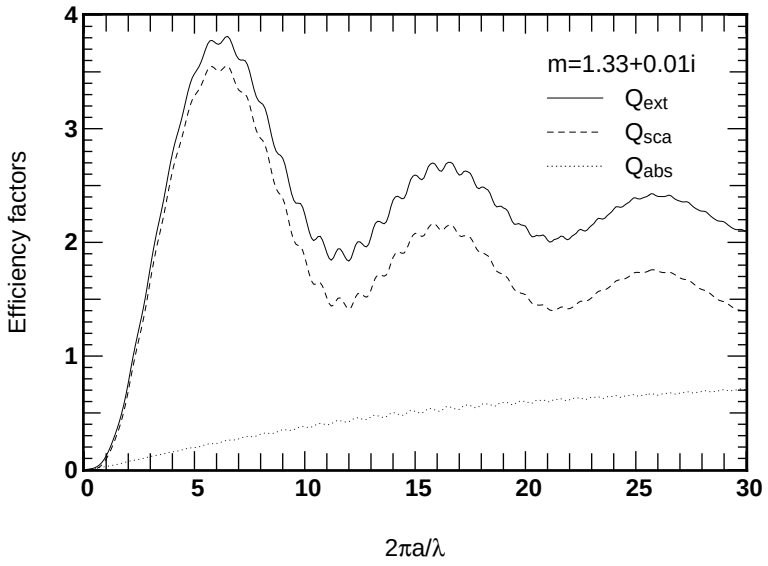

Figure 2.2: Extinction, absorption, and scattering efficiency factors of spherical grain with a constant refractive index, $m = 1.33 + 0.01i$, calculated by Mie theory (Mie, 1908; van de Hulst, 1957), using the publicly available code *bhmie* (Bohren & Huffman, 1983, the *bhmie* code is downloaded from http://www.astro.princeton.edu/˜draine/scattering.html).

where $x = 2\pi a/\lambda$ is the size parameter, and m is the complex refractive index of the grain, which is a function of λ in general. The coefficients a_n and b_n are given as

$$a_n = \frac{\psi_n(x)\cdot\psi_n'(mx) - m\psi_n(mx)\cdot\psi_n'(x)}{\zeta_n(x)\cdot\psi_n'(mx) - m\psi_n(mx)\cdot\zeta_n'(x)}, \tag{2.18}$$

$$b_n = \frac{m\psi_n(x)\cdot\psi_n'(mx) - \psi_n(mx)\cdot\psi_n'(x)}{m\zeta_n(x)\cdot\psi_n'(mx) - \psi_n(mx)\cdot\zeta_n'(x)}, \tag{2.19}$$

where the complex functions are given as

$$\psi_n(z) = zj_n(z) \tag{2.20}$$

$$\psi_n'(z) = \frac{d\psi_n}{dz} = zj_{n-1}(z) - nj_n(z) \tag{2.21}$$

$$\zeta_n(z) = z[j_n(z) + iy_n(z)] \tag{2.22}$$

$$\zeta_n'(z) = \frac{d\zeta_n}{dz} = z[j_{n-1}(z) + iy_{n-1}(z)] - n[j_n(z) + iy_n(z)], \tag{2.23}$$

by the spherical Bessel functions of the first kind (j_n) and the second kind (y_n).

While the efficiency factors are complicated function of x, in the Rayleigh-Jeans limit ($x \ll 1$), they reduce to

$$Q_{\rm abs} = 4x{\rm Im}\left(\frac{m^2-1}{m^2+2}\right) = 12x\frac{\epsilon_2}{(\epsilon_1+2)^2+\epsilon_2^2} \tag{2.24}$$

$$Q_{\rm sca} = \frac{8}{3}x^4\left|\frac{m^2-1}{m^2+2}\right|^2 = \frac{8}{3}x^4\left|\frac{\epsilon-1}{\epsilon+2}\right|^2, \tag{2.25}$$

where $\epsilon = \epsilon_1 + i\epsilon_2$ is the complex dielectric function related to the refractive index as $m^2 = \epsilon$. In the long wavelength limits, the dielectric function asymptote to

$$\epsilon_1 \rightarrow \text{const.} \tag{2.26}$$

$$\epsilon_2 \rightarrow A\frac{2\pi c}{\lambda} + \frac{2\pi\sigma\lambda}{c}, \tag{2.27}$$

where A is constant, and σ is the electrical conductivity (e.g., Draine , 2004; Draine, 2011). In both cases for insulator ($\sigma = 0$) and conductors ($\sigma \neq 0$), the efficiency coefficients scale as

$$Q_{\rm abs} \propto \lambda^{-2} \tag{2.28}$$

$$Q_{\rm sca} \propto \lambda^{-4}, \tag{2.29}$$

for $a \ll \lambda$ (FIR regime), insensitive to the dust chemical composition or sizes. Thus the dust scattering is negligible compared to its absorption at long wavelengths.

On the other hand, in the short wavelength limits, $a \gg \lambda$, $Q_{\rm ext}$ exactly asymptotes to constant, 2, independent of the nature of dust grains. This limiting value exceeds unity due to diffraction, in addition to the geometrical cross section, πa^2. In this regime, the dust reddening does not occur, as called as neutral extinction. Therefore, the fact that the observed extinction curve is increasing even at $10\mu{\rm m}^{-1} < 1/\lambda$ indicates the significant contribution of Galactic dust grains as small as $\sim 0.01\mu$m.

2.3 Dust composition model

When the composition and size distribution of dust grains are given, the extinction curve is straightforwardly calculated by following procedures: (1) compute the dielectric functions (or refractive indices) for each dust grains component (Draine & Lee, 1984; Draine & Li, 2007), (2) calculate the scattering and absorption cross section as functions of grains size using Mie theory , and (3) integrate the cross section over the size distribution following equations (2.13) and (2.14).

Current dust composition models take the silicate and graphite grains as the main component of dust grains, which explain the spectral features in dust extinction and absorption. The bump in extinction curves at $2175\mathring{A}$ (Figure 2.1) is considered due to $\pi \rightarrow \pi^*$ electronic excitation in graphites, and the infrared absorption features at 3.4, 9.7 and 18μm are thought to be the signature of C-H stretch, Si-O stretch, and O-Si-O bending modes.

Mathis, Rumpl, & Nordsieck (1977) found that the observed Galactic extinction curve is well produced assuming the power law size distribution, normalized by the number density of hydrogen $n_{\rm H}$, as

$$\frac{1}{n_{\rm H}}\frac{dn}{da} = Ca^{-3.5}, \tag{2.30}$$

for $50\mathring{\rm A} < a < 0.25\mu$m, where $C = 10^{-25.13}$ and $10^{-25.11}{\rm cm}^{2.5}$ for graphite and silicate grains, respectively. Weingartner & Draine (2001) and Li & Draine (2001) further sophisticated this size distribution function to better reproduce the observed Galactic extinction curve, for which Fitzpatrick (1999) fitting function is adopted, and the FIR emission spectrum measured by COBE and IRTS. Figure 2.3 shows the resulting cross sections of dust grains per unit dust mass.

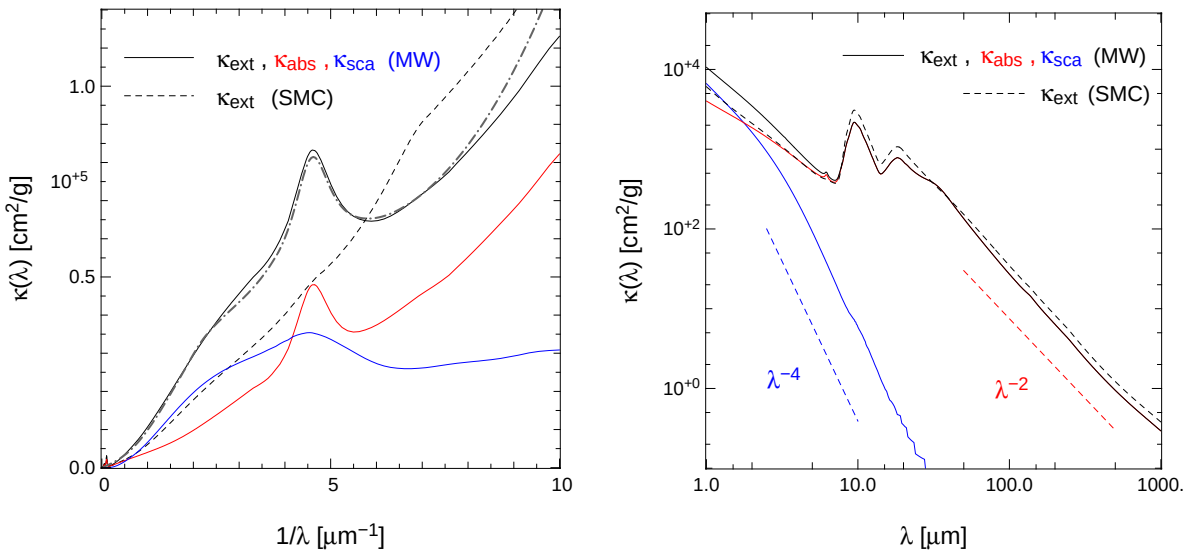

Figure 2.3: Cross sections of dust grains per unit dust mass by Weingartner & Draine (2001) dust model for $1/\lambda < 10\mu\mathrm{m}^{-1}$ (*left panel*) and $1.0\mu\mathrm{m} < \lambda < 1000\mu\mathrm{m}$ (*right panel*). Solid curves indicate the extinction (black), absorption (red), and scattering (blue) cross sections for Milky Way ($R_V = 3.1$) dust model. Dashed curve shows the extinction cross section for SMC dust model. Gray dot-dashed curve in *left panel* shows the Fitzpatrick (1999) fitting function normalized at V-band.

2.4 Relation between dust extinction and FIR emission

Dust grains typically absorb and scatter the UV to optical light of interstellar radiation field (ISRF), and reradiate its energy in FIR regime, where the dust emission peak is determined by the temperature of dust grains. Except for very small grains, for which stochasticity of heating becomes important, dust grains are well in thermal equilibrium. The dust thermal temperature is determined by the balance of heating and cooling.

The radiative heating rate of the dust grains is written as

$$\frac{dE_{\rm h}}{dt} = c\int d\lambda u_\lambda C_{\rm abs}(\lambda, a) \equiv c\pi a^2 \langle Q_{\rm abs}\rangle_{\rm ISRF}\langle u_\lambda\rangle, \tag{2.31}$$

where c is the speed of light, u_λ is the ISRF spectrum, and $\langle Q_{\rm abs}\rangle_{\rm ISRF}$ denotes the ISRF spectrum-averaged absorption cross section:

$$\langle Q_{\rm abs}\rangle_{\rm ISRF} \equiv \frac{\int d\lambda u_\lambda Q_{\rm abs}(\lambda)}{\langle u_\lambda\rangle} \quad , \quad \langle u_\lambda\rangle \equiv \int d\lambda\ u_\lambda. \tag{2.32}$$

On the other hand, the radiative cooling by dust thermal radiation is given as

$$\frac{dE_{\rm c}}{dt} = 4\pi\int d\lambda B(\lambda, T) C_{\rm abs}(\lambda, a) \equiv 4\pi a^2 \langle Q_{\rm abs}\rangle_T \sigma T^4, \tag{2.33}$$

where σ is the Stefan-Boltzmann constant, and $\langle Q_{\rm abs}\rangle_{\rm T}$ is the Planck-averaged absorption cross section:

$$\langle Q_{\rm abs}\rangle_T \equiv \frac{\int d\lambda B_\lambda(T) Q_{\rm abs}(\lambda)}{\int d\lambda B_\lambda(T)}. \tag{2.34}$$

If we assume the absorption cross section is given by a single power-law as $Q_{\rm abs} = Q_0(\lambda/\lambda_0)^{-\beta}$, equation (2.34) reduces to

$$\langle Q_{\rm abs}\rangle_T = \frac{15}{\pi^4}\Gamma(4+\beta)\zeta(4+\beta)Q_0\left(\frac{\lambda_0 k_B T}{hc}\right)^{\beta}, \tag{2.35}$$

where k_B, $\Gamma(x)$, and $\zeta(x)$ denote the Boltzmann constant, the Gamma function, and Riemann zeta function, respectively. Equating the heating and cooling rates, equations (2.31) and (2.33), the thermal equilibrium temperature is solved as

$$T = \left(\frac{hc}{\lambda_0 k_B}\right)^{\beta/(4+\beta)}\left[\frac{c\pi^4\langle Q_{\rm abs}\rangle_{\rm ISRF}}{60\Gamma(4+\beta)\zeta(4+\beta)Q_0\sigma}\right]^{1/(4+\beta)}\langle u_\lambda\rangle^{1/(4+\beta)}. \tag{2.36}$$

In the cases for silicate and graphite grains, adopting the ISRF spectrum in the solar neighborhood, equation (2.32) is approximated by

$$\langle Q_{\rm abs}\rangle_{\rm ISRF} = 0.18\times\left(\frac{a}{0.1\mu{\rm m}}\right)^{0.6} \quad ({\rm silicate}, 0.01<a<1\mu{\rm m}), \tag{2.37}$$

$$\langle Q_{\rm abs}\rangle_{\rm ISRF} = 0.8\times\left(\frac{a}{0.1\mu{\rm m}}\right)^{0.85} \quad ({\rm graphite}, 0.005<a<0.15\mu{\rm m}), \tag{2.38}$$

whereas the absorption cross sections in FIR regimes are well described by

$$Q_{\rm abs} = 1.4\times10^{-3}\left(\frac{a}{0.1\mu{\rm m}}\right)\left(\frac{\lambda}{\lambda_0}\right)^{-2} \quad ({\rm silicate}), \tag{2.39}$$

$$Q_{\rm abs} = 1.0\times10^{-3}\left(\frac{a}{0.1\mu{\rm m}}\right)\left(\frac{\lambda}{\lambda_0}\right)^{-2} \quad ({\rm graphite}), \tag{2.40}$$

where $\lambda_0 = 100\mu$m. Adopting equations (2.37) to (2.40), the equilibrium temperature of equation (2.36) reduces to

$$T = 16.4\left(\frac{a}{0.1\mu{\rm m}}\right)^{-1/15}\left(\frac{\langle u_\lambda\rangle}{\langle u_\lambda\rangle_{\rm MMP}}\right)^{1/6}{\rm K} \quad ({\rm silicate}), \tag{2.41}$$

$$T = 22.3\left(\frac{a}{0.1\mu{\rm m}}\right)^{-1/40}\left(\frac{\langle u_\lambda\rangle}{\langle u_\lambda\rangle_{\rm MMP}}\right)^{1/6}{\rm K} \quad ({\rm graphite}), \tag{2.42}$$

(Draine & Lee, 1984; Draine, 2011). Here $\langle u_\lambda\rangle_{\rm MMP}$ denotes the value for ISRF model by Mathis, Mezger, & Panagia (1983). Thus the dust equilibrium temperature is typically $\sim$ 20K, which results in emission peak at $\sim 150\mu$m, insensitive to the strength of ISRF and dust grain size.

Next we derive the relation between the dust extinction and emission. Equations (2.28) and (2.29) indicate that $C_{\rm sca}$ is much smaller than $C_{\rm abs}$ in the long wavelength limit, therefore equation (2.12) reduces to

$$dI(\lambda_{\rm FIR}, r) = \{B[\lambda_{\rm FIR}, T(r)] - I(\lambda_{\rm FIR}, r)\}d\tau_{\rm abs}(\lambda_{\rm FIR}). \tag{2.43}$$

Assuming T is independent of r, equation (2.43) is analytically solved as

$$I[\lambda_{\rm FIR}, \tau_{\rm abs}(\lambda_{\rm FIR})] = B(\lambda_{\rm FIR}, T)\{1-\exp[-\tau_{\rm abs}(\lambda_{\rm FIR})]\} + I_0(\lambda_{\rm FIR})\exp[-\tau_{\rm abs}(\lambda_{\rm FIR})], \tag{2.44}$$

where I_0 denotes the background intensity. Since the Galactic emission is dominated by dust emission in FIR, I_0 can be reasonably ignored. Therefore, if we consider an optical thin limit ($\tau_{\rm abs} \ll 1$), equation (2.44) reduces to

$$I[\lambda_{\rm FIR}, \tau_{\rm abs}(\lambda_{\rm FIR})] = B(\lambda_{\rm FIR}, T)\tau_{\rm abs}(\lambda_{\rm FIR}). \tag{2.45}$$

In the UV to optical regimes, which is in the Wien tail of the dust blackbody, the dust emission is negligible. In this case, ignoring the third term, equation (2.12) becomes

$$dI(\lambda_{\rm opt}, r) = -I(\lambda_{\rm opt}, r)d\tau_{\rm ext}(\lambda_{\rm opt}), \tag{2.46}$$

and gives

$$I(\lambda_{\rm opt}, r) = I_0(\lambda_{\rm opt}) \exp[-\tau_{\rm ext}(\lambda_{\rm opt})]. \tag{2.47}$$

Combining equations (2.3), (2.45), and (2.47), the relation between the dust extinction at $\lambda = \lambda_{\rm opt}$ and emission at $\lambda = \lambda_{\rm FIR}$ is given as

$$A(\lambda_{\rm opt}) = \frac{2.5}{\ln 10} \frac{\tau_{\rm ext}(\lambda_{\rm opt})}{\tau_{\rm abs}(\lambda_{\rm FIR})} \frac{I(\lambda_{\rm FIR})}{B(\lambda_{\rm FIR}, T)}. \tag{2.48}$$

Thus the observables for dust extinction, $A(\lambda_{\rm opt})$, and FIR emission, $I(\lambda_{\rm FIR})$, are proportional, whereas the conversion coefficient depends on the dust model and temperature.

Chapter 3

The SFD Galactic extinction map

3.1 Early attempts before SFD

It has been a difficult task to construct the dust map, which is equivalent to estimating the dust column density and its optical depth for each line of sight. Hubble (1936) modeled the distribution of the Galactic dust as a uniform disk with a finite height, h, along the Galactic plane. In this model, the path length crossing the dust layer is written as a function of galactic latitude, b, as $h\mathrm{cosec}|b|$. He assumed that the dust extinction is proportional to this length, thus the extinction is given as

$$A_V = h_1 \mathrm{cosec}|b|, \tag{3.1}$$

where h_1 denotes the extinction along the Galactic Pole (Binney & Merrifield, 1998).

Significant improvement from this toy model was achieved by Burstein & Heiles (1978, 1982, hereafter, BH). They estimated the extinction based on the HI column density map with FWHM = 0°.6 derived from 21cm flux map (Heiles, 1975). The relation between the dust reddening and the HI column density was calibrated using the reddening of 84 RR Lyrae stars and 49 globular clusters, as

$$E(B-V) = -0.0372 + 0.357 \times 10^{-3} \left(\frac{N_{\mathrm{H}}}{2.23 \times 10^{18} \mathrm{cm}^2} \right). \tag{3.2}$$

They reported the accuracy of their estimate is of the order of 0.01mag in $E(B-V)$.

3.2 The construction of the SFD map

Twenty years after the BH map, Schlegel, Finkbeiner, & Davis (1998) constructed the SFD Galactic extinction map. They used the IRAS/ISSA (Infrared Astronomical Satellite/IRAS Sky Survey Atlas) 100μm all-sky map, whose angular resolution is FWHM = 5′, as the tracer of the Galactic dust emission. Basically, they derived the dust extinction assuming that the dust FIR emission is proportional to the optical depth. Therefore it is not based on any direct measurement of the dust extinction itself. In order to correct for the dust temperature, as well as calibrate the IRAS 100μm data, they used the COBE/DIRBE (Cosmic Background Explorer / Diffuse Infrared Background Experiment) 100μm and 240μm data (FWHM=0°.7). The DIRBE 25μm data were also used for constructing the template of the zodiacal emission.

The procedure of SFD is summarized as follows:

1. The zodiacal emission, which is irrelevant for the Galactic dust emission, was subtracted from the DIRBE 100μm and 240μm data, using the DIRBE 25μm data as the zodiacal light template.

2. They constructed the dust temperature map from the color temperature estimated from the (zodiacal-subtracted) DIRBE 100μm and 240μm data.

3. The IRAS 100μm data were corrected for the IRAS calibration errors and the striping artifacts, using the DIRBE 100μm map as the calibrator.

4. Bright point sources identified by IRAS were removed.

5. The temperature-corrected IRAS 100μm emission was converted into the dust color excess, $E(B-V)$, using the Mg_2 index of elliptical galaxies as the standard color indicators.

We describe these construction procedures in details below.

3.2.1 Zodiacal light subtraction

The subtraction of the zodiacal light is crucial in constructing the Galactic extinction map from the FIR emission. The typical temperature of interplanetary dust (IPD), which is mainly responsible for the zodiacal light, is $\sim$ 280K, whereas that of the Galactic dust is typically $\sim$ 20K. Therefore the zodiacal emission is much higher than that of the Galactic dust by a factor of $\sim 10^5$ for an equivalent column density. In other words, the contribution of IPD in extinction is negligibly small compared to that of the Galactic dust with the same FIR emission. If the zodiacal emission is not subtracted, the extinction is impossible to be estimated from the FIR emission map should be significantly overestimated.

As the zodiacal light template, SFD used the DIRBE 25μm data, where the IPD emission is the most dominant in the DIRBE passbands, They first confirmed that the IPD temperature does not significantly vary over the all-sky, using the DIRBE 12μm to 60μm color temperature, and modeled the zodiacal-subtracted DIRBE data, D_b^Q, as

$$D_b^Q = D_b - [A_b + Q_b \bar{D}_{25}(\beta)] D_{25} - B_b, \tag{3.3}$$

where D_b ($b = 100\mu\mathrm{m}, 240\mu\mathrm{m}$) is the raw DIRBE data, A_b represents the scaling factor of the zodiacal emission from 25μm to passband b, and the offset B_b is responsible for the possible monopole component from the Galaxy or extragalactic light, *i.e.,* Cosmic Infrared Background (CIB). The quadratic term, $Q_b \bar{D}_{25}(\beta)$, is included to account for the IPD temperature variation as a function of ecliptic latitude, β, where $\bar{D}_{25}(\beta)$ denotes the average 25μm emission. Assuming that the resulting Galactic dust emission, D_b^Q, should be proportional to HI gas at high galactic latitudes, A_b, B_b, and Q_b are determined by minimizing the difference between D_b^L and HI flux by the Leiden-Dwingeloo 21cm Survey (Hartmann & Burton, 1997) at galactic latitude $|b| > 20^\circ$.

The residual scatter of D_{100}^Q against the HI flux is 0.05 MJy/sr in *rms*, which is equivalent to the error of 0.003 mag in r-band extinction, adopting the conversion factor determined as below. The resulting D_{100}^Q and D_{240}^Q are used for the dust temperate map and the calibration of the IRAS below.

3.2.2 Construction of the dust temperature map

Since the Galactic dust temperature varies from 17 to 21K, the dust emission at 100μm varies by a factor of ~ 5 within this temperature range for the same dust column density. Thus it is clearly needed to correct for the dust temperature to estimate the dust column density form FIR emission. Since IRAS data suffer from the significant calibration errors and noises, they used the well-calibrated DIRBE map, though its angular resolution is poor ($\sim 0°.7$), for the dust color temperature estimate. It should be noted that the resolution of the dust temperature correction is limited by that of DIRBE. The DIRBE 140μm data were also not used because its noise level is worse than that of the nearby 100μm data.

Their scheme is essentially equivalent to the spectrum fit to 100μm and 240μm data by the modified blackbody, $\kappa_{\rm abs}(\nu)B_\nu(T)$, where T is the dust temperature and $\kappa_{\rm abs}(\nu)$ is the dust emissivity assumed as $\kappa_{\rm abs}(\nu) \propto \nu^2$. Here they also assumed that the dust temperature is constant along each line of sight. The DIRBE 100μm and 240μm data, however, are still noisy in order to reliably calculate the temperature. Therefore they adopted a filtering scheme as below. They introduced a weight function, $\mathcal{W}$, that minimize the variance of

$$\frac{1}{\mathcal{R}} = \frac{D^S_{240}}{D^S_{100}}, \tag{3.4}$$

where D^S_b is the filtered DIRBE flux:

$$D^S_b = \mathcal{W} D^Q_b + (1-\mathcal{W})\bar{D}^Q_b, \tag{3.5}$$

and $\bar{D}^Q_b$ is the average background level estimated at high galactic latitude. Then they solved

$$\mathcal{R}(T) = \frac{D_{100}}{D_{240}} = \frac{K_{100}(T)I_{100}(T)}{K_{240}(T)I_{240}(T)}, \tag{3.6}$$

for the temperature T, where

$$K_b(T) = \int d\nu B_\nu(T)\nu^2 W_b(\nu), \tag{3.7}$$

$W_b(\nu)$ denotes the DIRBE response function, and I_b is the intrinsic intensity not affected by the response function. The temperature correction factor, $X(T)$, is derived as

$$X(T) = \frac{B_{100}(T_0)K_{100}(T_0)}{B_{100}(T)K_{100}(T)}, \tag{3.8}$$

so as to translate into the reference temperature, $T_0 = 18.2$K. This correction factor is shown in Figure 3.2 as a function of T. Finally, the temperature corrected 100μm flux is given as

$$D^T = D^Q_{100} X(T). \tag{3.9}$$

The assumption that the dust temperature is constant along a single line of sight is not necessarily correct. Therefore they checked the validity of the assumption as follows. They considered the sum of two blackbody spectrum with temperatures 18K and T_B. If it is fitted by a single temperature blackbody, the true column density was systematically, but only 10% underestimated for the range of $15 < T_B < 21.5$K, which well covers the variation of the dust temperature obtained above. The resulting temperature map is shown in Figure 3.3.

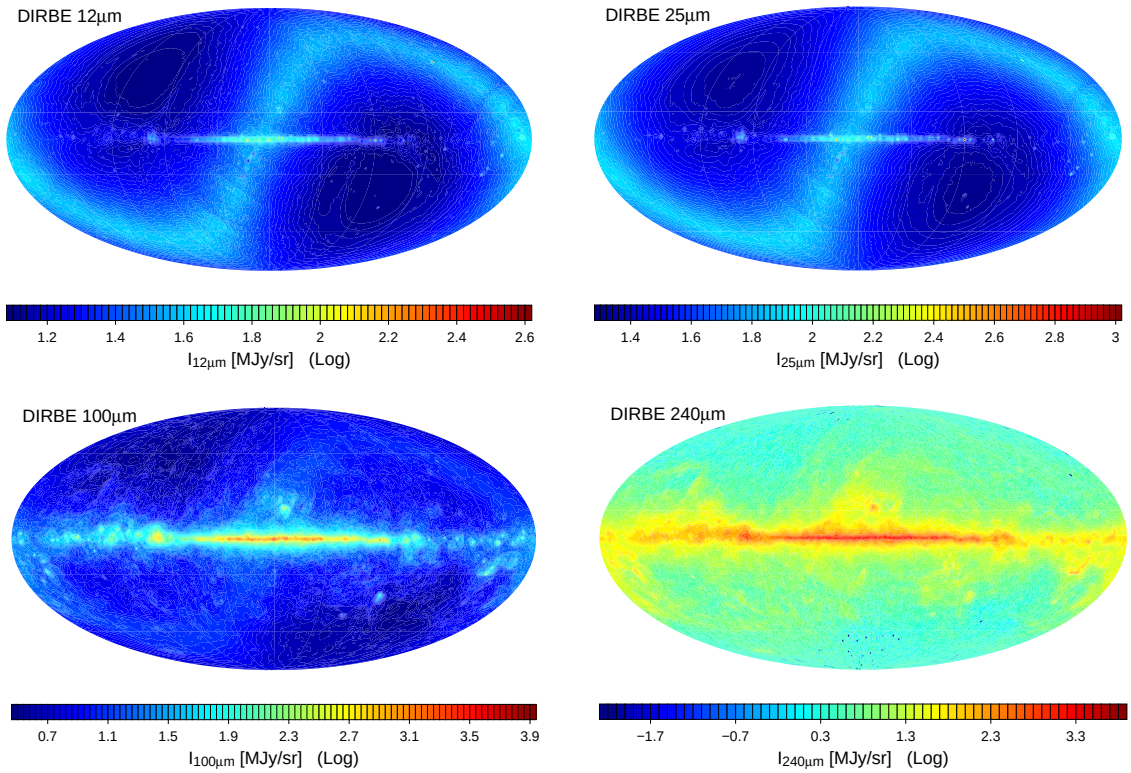

Figure 3.1: The raw data of COBE/DIRBE all-sky map at 12, 25, 100, and 240μm in Galactic coordinates. At 12 and 25μm, the zodiacal emission is clearly dominating over the entire sky. At 100 and 240μm, the Galactic dust emission near the Galactic plane is prominent, but still the significant zodiacal light is visible. The intensities are log scaled. The data are downloaded from NASA/IPAC infrared science archive (http://irsa.ipac.caltech.edu/data/Planck/release_1/external-data/external_maps.html).

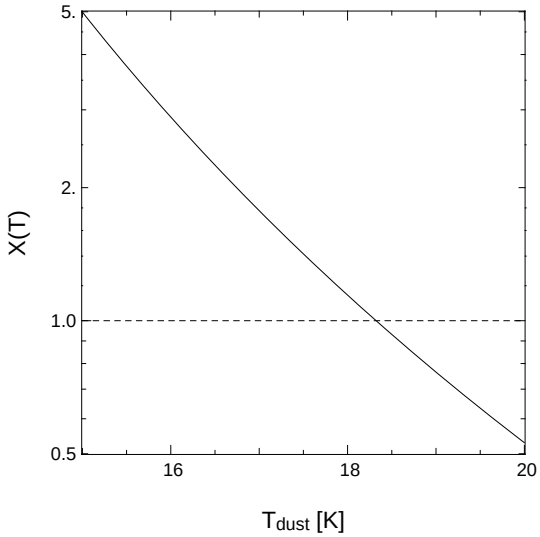

Figure 3.2: Temperature correction factor, $X(T)$, in equation (3.8) as a function of the dust temperature. Derived from equations (16) and (17) in Schlegel, Finkbeiner, & Davis (1998).

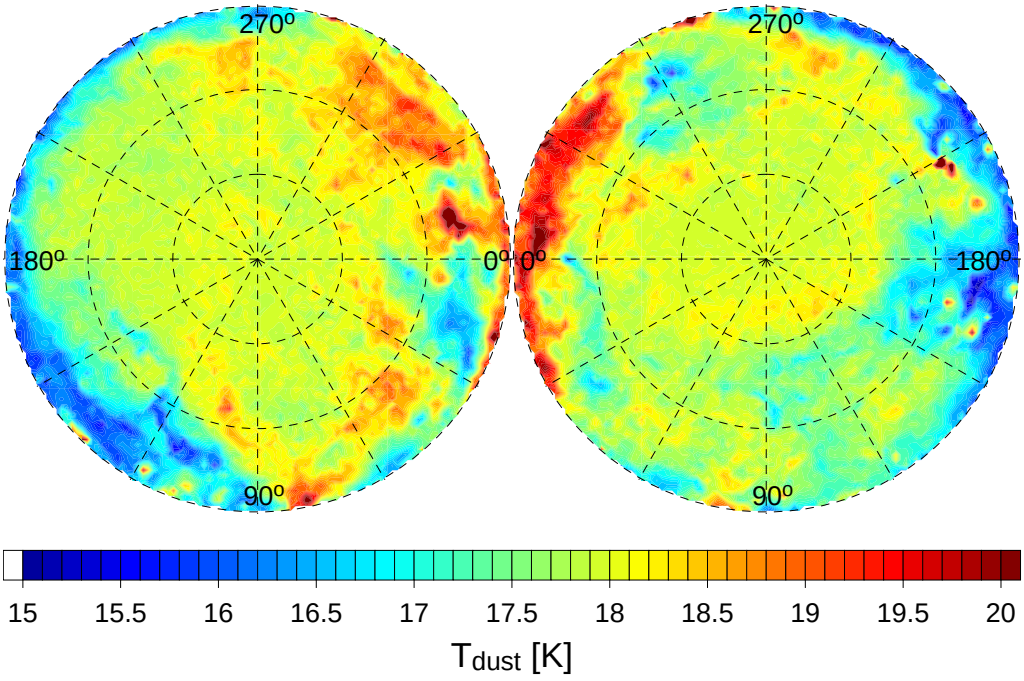

Figure 3.3: Dust temperature map derived from the DIRBE 100 and 240μm data in Galactic coordinate. The centers of Lambert projection are North Galactic Pole (*left panel*) and South Galactic Pole (*right panel*). The dashed lines are drawn by the interval of 30° for Galactic latitudes and longitudes.

3.2.3 Calibration of the IRAS data

The IRAS data suffer from the calibration uncertainties and the striping artifacts, whereas the DIRBE data are better calibrated, but their angular resolution is worse. Therefore, they calibrated the IRAS data at the scale of the DIRBE resolution, keeping the IRAS small scale fluctuations as follows.

They first Fourier transformed each plate of the IRAS 100μm data, and removed the striping artifacts by replacing the fourier modes of striping feature by the modes with the same wavenumber, but different phase. The resulting 100μm data are denoted as $I_{\rm des}$.

Next they convolved the IRAS data with FWHM = 3′.2 Gaussian, and corrected the IRAS gain to match the DIRBE data, multiplying the conversion factor, $C = 0.87$, which is assumed to be constant over the entire sky. Thus the calibrated IRAS data, $I_{\rm corr}$, are written as

$$I_{\rm corr} = C \cdot I_{\rm des} * W^G(3'.2) + \mathcal{I}, \tag{3.10}$$

where they calibrated the IRAS to the DIRBE dat on scales larger than 1°, adding the zero-point difference map

$$\mathcal{I} = [D^Q - C \cdot I_{\rm des} * W^G(3'.2) * W^{\square}(21')] * W^G(40'). \tag{3.11}$$

Here the destriped IRAS data, $I_{\rm des}$, was smoothed with Top-Hat filter of radius 21′, and then the difference from the color-corrected DIRBE data, D^Q, is taken as the zero-point drift of the IRAS. This difference map was further smoothed by FWHM = 40′ Gaussian filter. Since the zodiacal light had been already removed from the DIRBE data, D^Q, the resulting IRAS data, $I_{\rm core}$, are also corrected for the zodiacal emission.

3.2.4 Subtraction of the IRAS point sources

The IRAS 100μm data contain the emission from extragalactic objects and the Galactic stars, which should be removed for estimating the Galactic dust emission. They removed $\sim 10^4$ extragalactic point sources, 70 large galaxies, and ~ 5000 stars, identified by the IRAS 1.2Jy Galaxy Survey and the PSCZ redshift survey. They removed sources selected according to the 60μm fluxes, as $f_{60\mu\mathrm{m}} > 1.2$Jy for the IRAS 1.2Jy Galaxy Survey, and $f_{60\mu\mathrm{m}} > 0.6$Jy for the PSCZ redshift survey. Since the shape of the IRAS PSF is very complex and depends on scan directions, they replaced the pixels that contains the point sources by the median of the neighbor pixels.

They noted that many faint galaxies inevitably remain in the IRAS map. Those galaxies just below the adopted flux cut, however, has roughly $f_{100\mu\mathrm{m}} \sim 1.2$Jy, thus the contamination of those sources contribute at most ~ 0.01mag in r-band.

3.2.5 Converting the 100μm emission to extinction

Assuming the proportionality between the dust 100μm emission and column density, the reddening is written as

$$E(B-V) = pI_{\mathrm{corr}}X, \tag{3.12}$$

where X is the temperature correction factor derived above. The remaining task is to determine the normalization factor, p. They used the Mg_2 indices of ~ 400 elliptical galaxies (Faber et al., 1989) for this purpose. The Mg_2 index is the absorption strength at 5200Å, and known to tightly correlate with the colors of elliptical galaxies, therefore it can be used as the indicator of the intrinsic color of ellipticals. They determined the normalization, p, so that the residual of the correlation between the Mg_2 indices and the colors of the ellipticals corrected with their $E(B-V)$ is minimized. They found $p = 0.0184 \pm 0.0014$ from this calibration, and reported the residual of the elliptical colors is $\sim 10\%$, which is a factor of 2 smaller than that for the BH maps.

Figure 3.4 is the final extinction map, in terms of $E(B-V)$. They also presented the conversion factor from $E(B-V)$ to a set of other passbands that cover the range from 3300Å to 3.8μm, assuming O'Donnell (1994) and Cardelli et al. (1989) reddening law with $R_V = 3.1$.

3.3 Previous attempts to study the SFD map accuracy

Since the SFD map achieved higher angular resolution and accuracy than the BH map, it has been widely-used in all branches of extragalactic astronomy. Nevertheless, it is not based on direct measurement of dust extinction, and therefore it is important to check the reliability of the SFD map through independent observations.

3.3.1 High extinction regions

In high-extinction regions, such as molecular clouds, nebulae, or near the Galactic plane, many earlier studies examined the reliability of the SFD map by independently estimating the amount of dust extinction.

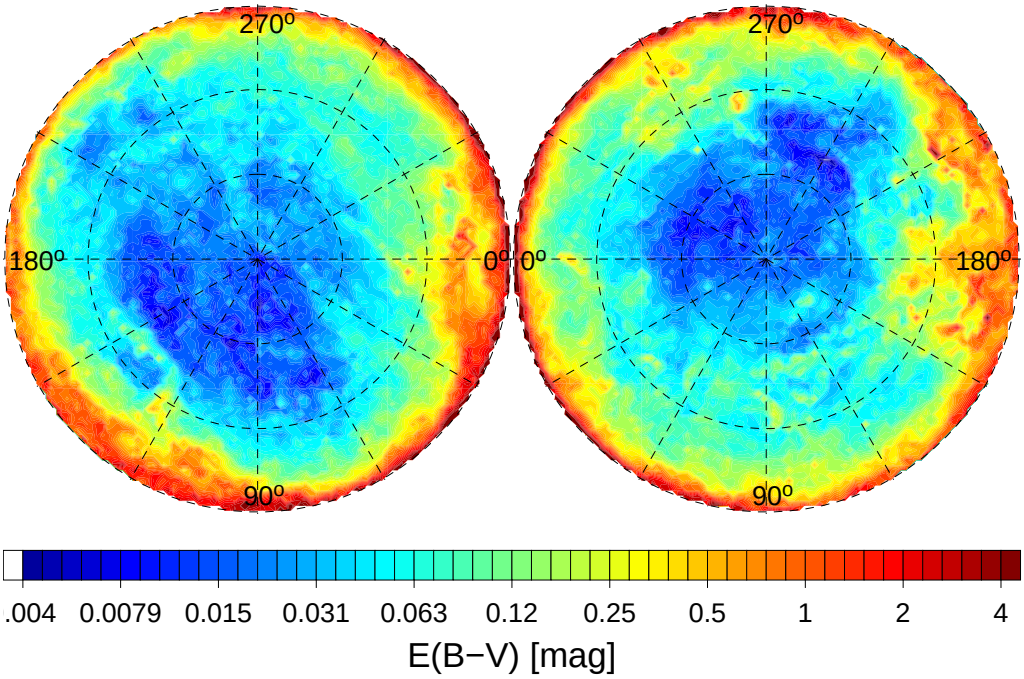

Figure 3.4: The SFD Galactic extinction map in $E(B-V)$ with logarithmic color scale. The projection is the same as Figure 3.3.

Arce & Goodman (1999a,b) derived the dust extinction, A_V, towards the Taurus dark cloud complex using four independent methods. Their results suggest that the SFD map over-predicts the extinction by a factor of 1.3–1.5 in the Taurus cloud region with $A_V > 0.5$ mag. They also found that the SFD map under-predicts the extinction towards those regions where the extinction sharply peaks.

Cambrésy et al. (2001) estimated the B-band extinction towards the Polaris molecular cirrus cloud using a star-count method, and found that the SFD extinction is $\sim$ 2 to 3 times larger than that from the star counts. They further confirmed that the SFD map over-predicts extinction by a factor of 1.3 where $A_V > 1.0$ mag, compared to that estimated by NIR galaxy colors of 2MASS (Two Micron All Sky Survey) Extended Source Catalog (Jarrett et al., 2000).

Yasuda et al. (2007) applied the galaxy number count method for the SDSS low Galactic latitude sample (Finkbeiner et al., 2004) and estimated extinction where $E(B-V) > 0.15$. They found that the SFD map overestimates reddening by a factor up to 1.4.

Several other studies also found that the SFD map overestimates the amount of dust extinction at high extinction regions (Chen et al., 1999; Dobashi et al., 2005; Rowles & Froebrich, 2009). The origin of the SFD over-estimate is often attributed to the relatively poor angular resolution of the temperature map, which cannot trace the complex structure of ISM in such high extinction regions. Another possible origin is the variation of dust grain components, which SFD assume to be uniform over the entire sky and along the line of sights. Indeed, Cambrésy et al. (2001, 2005) argued that the discrepancies between the SFD prediction and their estimation would be explained by introducing the cold dust components with higher FIR emissivity.

3.3.2 Low extinction regions

In contrast, the reliability of the SFD map in low-extinction regions has not been carefully examined until the large data set with very accurate photometry became available, including the Sloan Digital Sky Survey (SDSS), and more recently PAN-STARRS1. Earlier studies usually validated the accuracy of the SFD map in low-extinction region (Fukugita et al., 2004; Mörtsell, 2013; Tian et al., 2014; Green et al., 2014; Schlafly et al., 2014), while the possible systematic trends were often reported by several studies as follows.

Fukugita et al. (2004) tested the SFD map at low extinction regions where $E(B-V) < 0.15$, using number counts of the SDSS DR1 (Abazajian et al., 2003) galaxies. They measured the differential number count of the SDSS galaxies as a function of $r-$band magnitude, dN/dm_r, and compared its spatial variation with the SFD extinction. As a result, they found that the results are consistent with the SFD map. On the other hand, Yahata et al. (2007) revealed the systematic errors in the SFD map using SDSS DR4 galaxies, which is the main topic of this thesis. In the following section, we describe their results and interpretation in detail.

Using the SDSS stars, Schlafly et al. (2010) measured dust reddening from the shift of the bluer edge of the stellar locus as standard color indicator. They found that the SFD map over-predicts $E(B-V)$ by $\sim 14\%$ in southern sky, possibly due to the errors in the dust temperature map. They also pointed out that the extinction curve of the Galactic dust is better described by the Fitzpatrick (1999) reddening law with $R_V = 3.1$ rather than that by O'Donnell, which is recommended by SFD. These results are confirmed using the colors of the SDSS/SSPP (The Sloan Extension for Galactic Understanding and Exploration Stellar Parameter Pipeline; Lee et al., 2008) stars (Schlafly & Finkbeiner, 2011), and using SDSS and 2MASS starts (Berry et al., 2012).

Peek & Graves (2010) compared the SFD map and the colors of the passively evolving galaxies which are selected from the SDSS DR7 spectroscopic Main Galaxy Sample (Strauss et al., 2002) according to their emission lines. The passively evolving galaxies are known to populate a tight sequence in the color-magnitude diagram, thus they compared the shift of galaxy colors from the sequence with the SFD map. As a result, their measurement and the SFD map is consistent for most of the sky area, within 3 mmag in $E(B-V)$. Nevertheless, they found that the SFD map under-predicts reddening in some regions, at most by 0.045 mag in $E(B-V)$. They noted that the SFD map tends to under-predict reddening where the SFD dust temperature is low, possibly because the dust temperature varies along the line of sight in those regions, whereas SFD assumed it to be constant. They corrected the SFD map for those deviations and constructed a corrected Galactic extinction map at $4^\circ.5$ resolution. Figure 3.5 shows their correction map, which is also tested in section 5.6.2 as well as the SFD map.

3.4 Discovery of the anomaly in the SFD map by SDSS DR4 analysis

Yahata et al. (2007) tested the SFD map by the galaxy number count analysis using the SDSS DR4 data sets. They used $\sim 3 \times 10^6$ photometric galaxies with $17.5 < m_r < 19.4$ from the SDSS DR4 catalog, which covers $\sim 6600\mathrm{deg}^2$ of sky area.

They first divided the entire SDSS DR4 sky area into small pixels with the area of

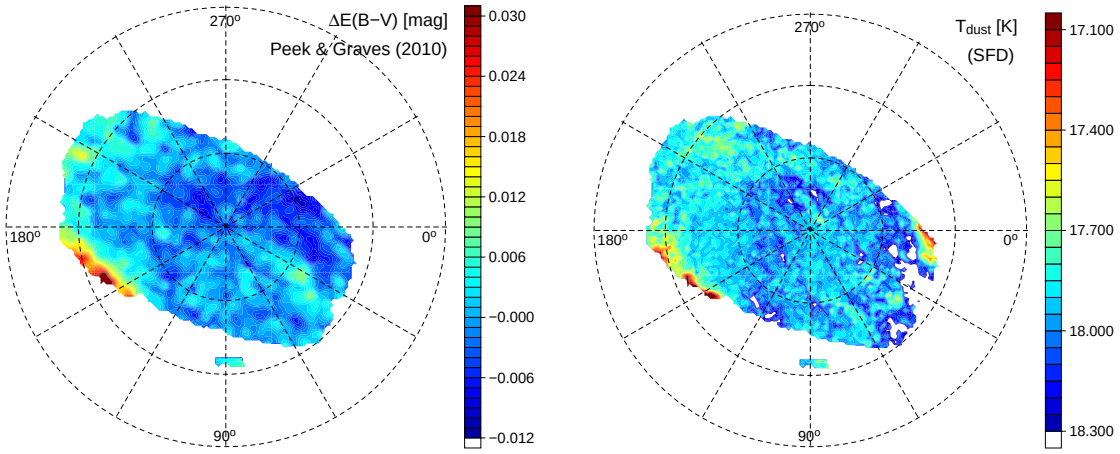

Figure 3.5: *Left panel*; Correction to the SFD map in $E(B-V)$ provided by Peek & Graves (2010) at the resolution of $\sim 4'.5$. This correction term, $\Delta E(B-V)$, is to be added to the SFD map extinction. The projection is the same as Figure 3.3, but the data are only available for the SDSS sky area in the north galactic hemisphere. *Right panel*; Dust temperature map by SFD as the same as Figure 3.3, but only the SDSS sky area is shown for visual comparison with *left panel*.

$(2'.37)^2$, which corresponds to the resolution of the SFD map. Those pixels are grouped into 69 bins according to the values of the SFD map extinction. This results in the 69 subregions with almost equal areas, $\sim 100\mathrm{deg}^2$, where each subregion is spatially discontinuous (see Figure 5.3 for the schematic example of the discontinuous subregions). They next counted the number of the galaxies in each subregion, whose observed (extinction-uncorrected) and extinction-corrected r-band magnitudes are within the fixed range, 17.5 and 19.4. Finally they calculated the surface number density of galaxies as a function of the SFD extinction.

If the SFD map is perfect, the surface number densities without extinction correction should decrease against the SFD extinction, since more objects are dimmed and exceed the fainter magnitude limit in the higher extinction region. On the other hand, if the dust extinction is properly corrected using the SFD map, the surface number densities should be constant and independent of the SFD extinction. The resulting surface number densities shown in Figure 3.6 indicated the expected behavior at relatively high extinction regions, $A_{r,\mathrm{SFD}} > 0.1$ mag. At low extinction regions with $A_{r,\mathrm{SFD}} < 0.1$ mag, however, the surface number densities exhibited the *positive* correlation with the SFD extinction, exactly opposite to the expected behavior of dust extinction.

One may naively consider that the observed anomaly of the SFD map is due to unknown dust components that are not traced by FIR emission, in the low extinction region. They found, however, that the SFD extinction tightly correlates with the HI 21cm flux, and no signature of such unknown components is seen in the HI flux. Furthermore, they performed the same number count analysis using the SDSS spectroscopic galaxies and photometric quasars (Richards et al., 2004). The results are shown in Figure 3.7. Interestingly, the spectroscopic galaxies with $z > 0.1$ exhibited a weaker anomaly compared to those with $z < 0.1$, and the photometric quasars, if any, indicated a quite weak correlation with the SFD extinction. If the anomaly is due to unknown component of the

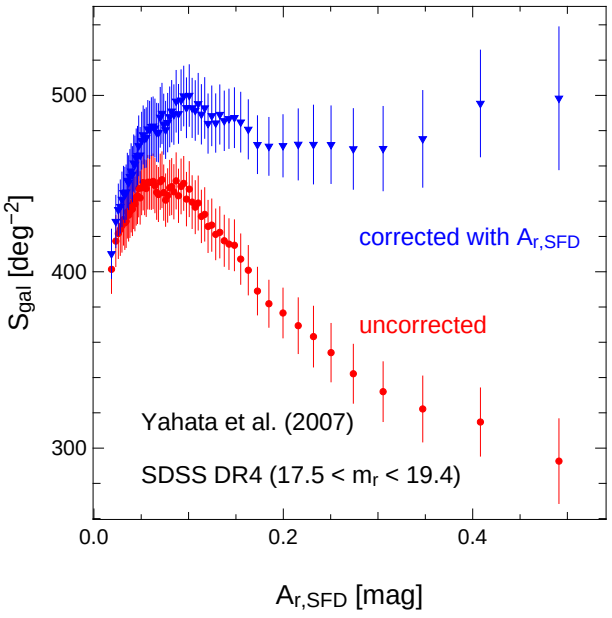

Figure 3.6: Surface number densities of the SDSS DR4 photometric galaxies with $17.5 < m_r < 19.4$, as a function $A_{r,\mathrm{SFD}}$ (Yahata et al., 2007). The circles/triangles indicate the surface number densities calculated with extinction un-corrected/corrected magnitudes, respectively. At low extinction region, $A_{r,\mathrm{SFD}} < 0.1$ mag, the surface number densities *positively* correlate with $A_{r,\mathrm{SFD}}$, opposite to the expected effect of dust extinction.

Galactic dust, the surface number densities of the extragalactic objects should indicate the similar anomaly as the photometric galaxies, independent of the distance to the objects. Therefore, these results imply that the origin of the anomaly is related to the galaxies themselves, especially to nearby galaxies, rather than the Galactic dust itself.

Instead, they proposed a hypothesis that the observed anomaly is due to the contamination of the FIR emission of galaxies that are too faint to be individually removed from the SFD map. Since the SFD map is constructed from the assumption of the simple proportionality to 100μm emission, the anomalous *positive* correlation between the surface number density of galaxies and the SFD extinction can be interpreted as the correlation between the surface density of the galaxies and their FIR emission. For distant objects, fluctuations of their FIR emission and surface densities should be small, if averaged over the relatively large pixels of the SFD map, which would result in the absence of the anomaly for those objects.

We note that the hypothesis of the FIR contamination would explain why the number count analysis by Fukugita et al. (2004) did not found any signature of the anomaly, despite that their methodology is essentially equivalent to that of Yahata et al. (2007). Fukugita et al. (2004) divided the sky area of SDSS DR1 into patches with the area of $2^\circ.5 \times 2^\circ.5$, which is much larger than the pixels adopted by Yahata et al. (2007), and counted the number of galaxies in each patch. Due to the variance of the Galactic extinction in the relatively large area of the patches, the correlation between the dust extinction and the number of galaxies would be smoothed out.

SFD reported that the amount of the cosmic infrared background is $\nu I_\nu \sim 25\mathrm{nWm}^{-2}\mathrm{sr}^{-1}$ at 100μm, which corresponds to 0.04 mag in r-band extinction. Yahata et al. (2007) dis-

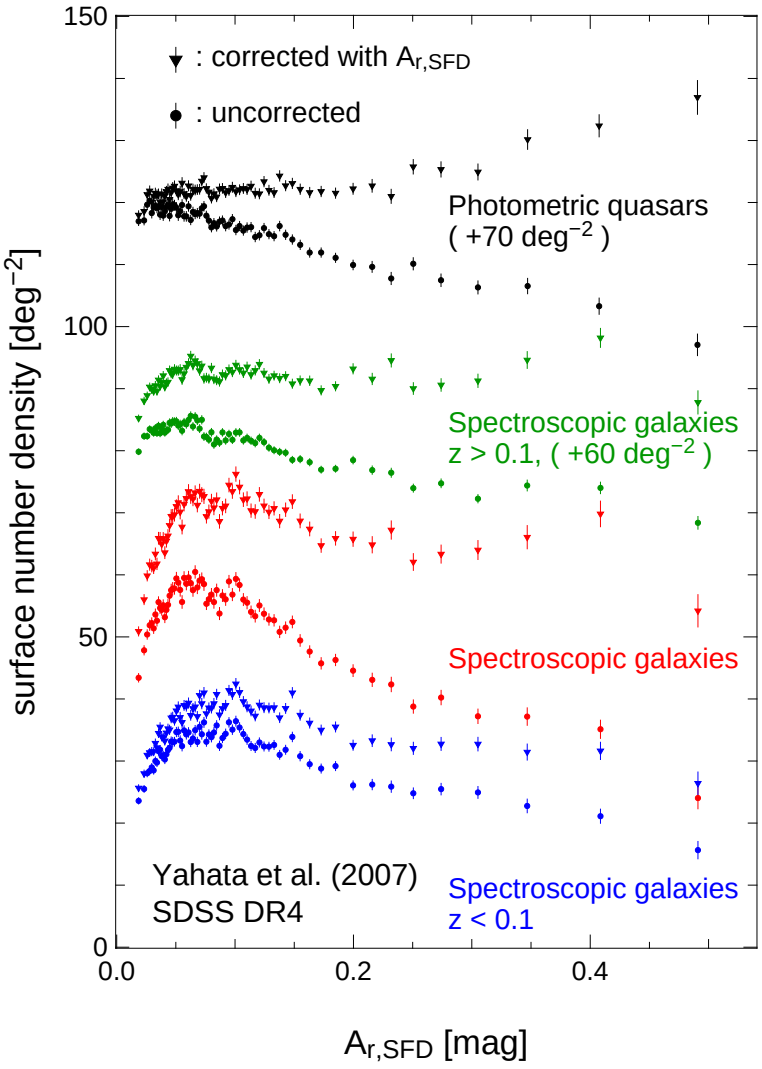

Figure 3.7: Surface number densities of the SDSS DR4 spectroscopic galaxies (blue: $z < 0.1$, green: $z > 0.1$, red: all) and photometric quasars (black) as a function of $A_{r,\mathrm{SFD}}$ (Yahata et al., 2007). The circles/triangles indicate the surface number densities calculated with extinction un-corrected/corrected magnitudes, respectively. The error bars reflects the Poisson noise alone. The surface number densities of the spectroscopic galaxies with $z > 0.1$ and photometric quasars are shifted by $+60\mathrm{deg}^{-2}$ and $+70\mathrm{deg}^{-2}$, for clarity.

cussed that the amount of the FIR contamination due to SDSS galaxies should be smaller than that level, maybe less than 0.01 mag. They performed a simple numerical experiment and showed that even such a quite small contamination could qualitatively reproduce the observed anomaly. Thus, the possible systematic in the SFD map due to FIR contamination would not cause a significant problem for most purposes. Since it is directly associated with the spatial distribution of galaxies, however, it may systematically affect the cosmological interpretations of the large scale structure of the universe. This is why we investigate the origin of the anomaly carefully in Chapter 4 and 5.

Chapter 4

Detection of the FIR emission from SDSS galaxies by stacking analysis

This Chapter presents the stacking image analyses of SDSS DR7 galaxies over the SFD map, aiming at the direct detection of the FIR emission of galaxies in the SFD map. Since SFD subtracted the detectable extragalactic sources, the FIR emission of most galaxies in the SFD map cannot be individually detected. The stacking analysis using the large data set of SDSS, however, enables us to measure the average FIR emission of those galaxies in a statistical fashion. The detection of the FIR emission in the SFD map presented below directly confirms the hypothesis of the FIR contamination first proposed by Yahata et al. (2007).

4.1 Sloan Digital Sky Survey DR7

In the following analysis, we use the Sloan Digital Sky Survey (SDSS) DR7 photometric galaxy catalog. SDSS DR7 covers 11663 deg^2 of sky area, with photometry in five passbands; u, g, r, i, and z (Stoughton et al., 2002; Gunn et al., 1998, 2006; Fukugita et al., 1996; Hogg et al., 2001; Ivezić et al., 2004; Smith et al., 2002; Tucker et al., 2006; Padmanabhan et al., 2008; Pier et al., 2003). The photometric data is corrected for the Galactic extinction using the SFD map (Stoughton et al., 2002). They calculated the extinction in each passband adopting the conversion factors from the SFD color excess, $E(B-V)$:

$$k_x \equiv \frac{A_{x,\mathrm{SFD}}}{E(B-V)}, \tag{4.1}$$

where $x = u$, g, r, i, and z. They adopted the values provided in Table 6 of SFD, which is computed assuming the Cardelli et al. (1989) and O'Donnell (1994) extinction curve with $R_V = 3.1$, and the spectral energy distribution of elliptical galaxies.

Since the spatial distribution of stars in the SDSS catalogue is likely to be correlated with the Galactic dust distribution, the contamination of stellar objects in the galaxy sample systematically affects our results. For the reliable star-galaxy separation, we carefully select our galaxy sample following Yahata et al. (2007) as follows.

We note that our analysis below does not exclude the galaxies that are also detected by IRAS PSCz (Saunders et al., 2000) that are removed in the SFD map. We made sure, however, that this has a negligibly small effect on our result because of the small number

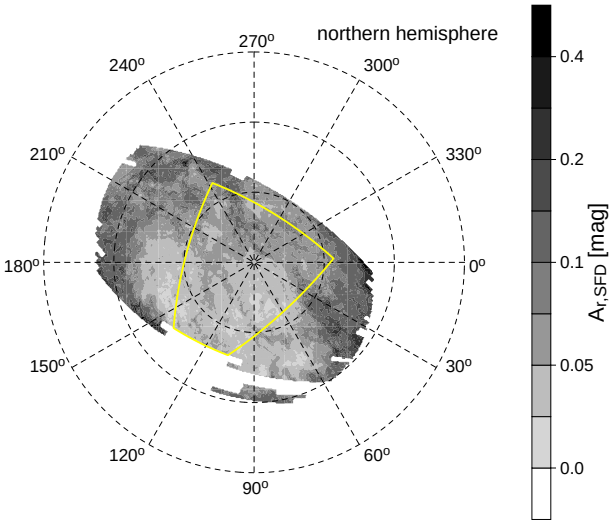

Figure 4.1: The region of the sky used for the present analysis, which is shaded according to the extinction value $A_{r,\mathrm{SFD}}$. The yellow lines indicate the inner regions used for comparison in Subsection 4.2.2.

of overlapped galaxies.

4.1.1 Sky area selection

We choose the regions of SDSS DR7 survey area labeled "PRIMARY". Indeed we found that the "PRIMARY" regions in the southern Galactic hemisphere are slightly different from the area where the objects are actually located. We are not able to understand why, and thus decide to use the regions in the northern Galactic hemisphere alone to avoid possible problems.

To ensure the quality of good photometric data, we exclude masked regions. The SDSS pipeline defines the five types of masked regions according to the observational conditions. We remove the four types of the masked regions, labeled "BLEEDING", "BRIGHT_STAR", "TRAIL" and "HOLE" from our analysis. The masked regions labeled "SEEING" is not removed, since relatively bad seeing does not seriously affect the photometry of relatively bright galaxies that we use in the present analysis. The total area of the removed masked regions is about 340 deg^2, which comprises roughly 4.5% of the entire "PRIMARY" regions in the northern Galactic hemisphere.

The resulting survey area used in this thesis is shown in Figure 4.1, which covers $\sim 7270\mathrm{deg}^2$.

4.1.2 Removing false objects

We remove false objects according to photometry processing flags. We first remove fast-moving objects, which are likely in the Solar system or associated with the interplanetary dust. We also discard objects that have bad photometry or were observed in the poor condition. A fraction of objects suffers from deblending problems, *i.e.*, the decomposition of photometry images consisting of superimposed multi-objects is unreliable or failed. We remove such objects as well.

4.1.3 Magnitude range of galaxies

The SDSS catalogue defines the type of objects according to the differences between the *cmodel* and PSF magnitudes, where the former magnitude is computed from the composite flux of the linear combination of the best-fit exponential and de Vaucouleurs profiles. An object is classified as a galaxy if

$$m_{\rm PSF} - m_{\rm cmodel} > 0.145, \tag{4.2}$$

and otherwise classified as a star. Since the reliability of this star-galaxy separation method depends on the model magnitude *before* extinction correction, we choose the magnitude ranges of our sample for the analysis as follows. In r-band, the star-galaxy separation is known to be reliable for galaxies brighter than $\sim$21 mag (Yasuda et al., 2001; Stoughton et al., 2002), while the saturation of stellar images typically occurs for objects brighter than 15 mag in r-band. Therefore, we use the galaxies selected by r-band magnitude as $15.5 < m_r < 20.5$, where m_r denotes the extinction-corrected magnitude. Since the r-band extinction predicted by SFD is at most 0.5mag, the reliable star-galaxy separation criteria, $m_r < 21$, is satisfied even for the faintest galaxies in the highest extinction regions.

4.2 Stacking analysis

4.2.1 Stacking Method

As discussed by Yahata et al. (2007), the amount of FIR emission from SDSS galaxies is expected to be very small, and it is impossible to detect for individual galaxies. Therefore we stack those regions of the SFD map centered at the positions of SDSS photometric galaxies and quasars over their appropriate magnitude bins.

The original SFD map divides all sky area into $2'.37 \times 2'.37$ pixels and the extinction value is provided for the central position of each pixel. The histograms of $A_{r,\rm SFD}$ evaluated at those pixels as a function of the number of galaxies with $15.5 < m_r < 20.5$ within the pixel, $N_{\rm g,pix}$, are shown in Figure 4.2. While the overall shapes of the histograms are very similar for different $N_{\rm g,pix}$, the normalized probability density function (PDF) plotted in Figure 4.3 exhibits the small but systematic shift toward the larger $A_{r,\rm SFD}$ with increasing $N_{\rm g,pix}$. This indicates the correlation of the Galactic extinction and the background galaxies that will be extensively discussed in what follows.

First we show the result of stacked SFD map images centered at photometric galaxies in the r-band magnitude range of $17.5 < m_r < 19.4$ randomly selected from a contiguous region in Figure 4.1. In this procedure we evaluate the value of $A_{\rm r,SFD}$ on $0'.2 \times 0'.2$ pixels over $40' \times 40'$ images by cloud-in-cell interpolation of the 4 nearest neighbors in the original SFD pixels. Each image is stacked after randomly rotated. Upper panels of Figure 4.4 clearly show the presence of the strong feature of $A_{r,\rm SFD}$ around SDSS galaxies, which becomes more pronounced as increasing the number of stacked galaxies. For reference, lower panels of Figure 4.4 show the stacked SFD map images centered at the same number of randomly chosen positions from the same region of the corresponding top panels. Figure 4.5 shows the radial profiles of the stacked images for the randomly selected SDSS galaxies. This result directly confirms the interpretation of Y07 that the SFD map is contaminated by the FIR emission from SDSS galaxies.

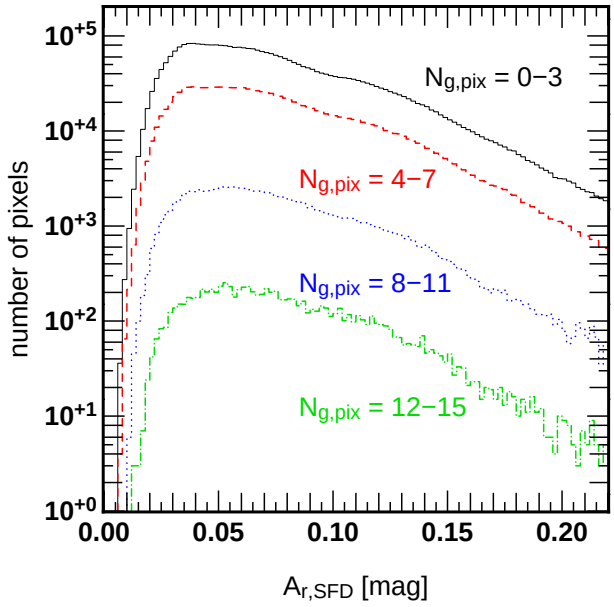

Figure 4.2: Histograms of $A_{r,\mathrm{SFD}}$ for $2'.37 \times 2'.37$ pixels over our selected survey region of SDSS DR7 as a function of the number of galaxies within the pixel, $N_{\mathrm{g,pix}}$; $N_{\mathrm{g,pix}} = 0-3$ in black, $4-7$ in red, $8-11$ in blue, and $12-15$ in green.

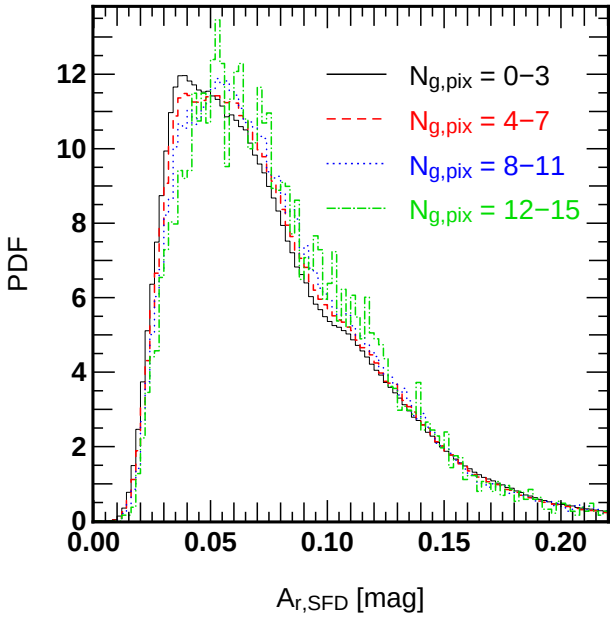

Figure 4.3: The normalized probability density function (PDF) of $A_{r,\mathrm{SFD}}$ corresponding to Figure 4.2.

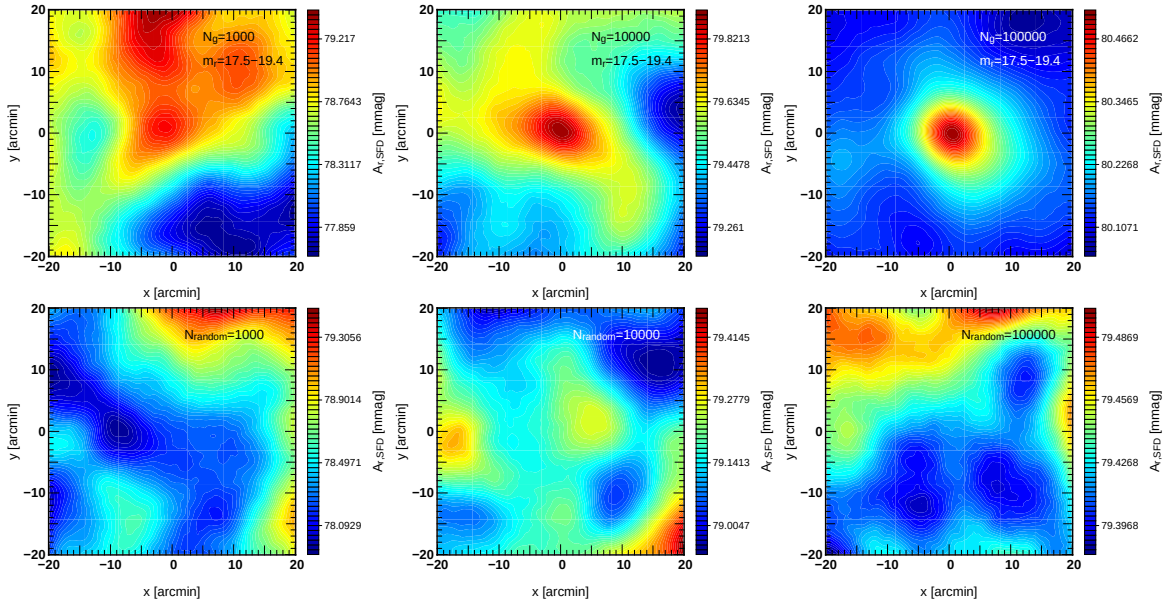

Figure 4.4: Stacked images of the SFD map for $40' \times 40'$ regions; *Upper panels* are centered at the positions of SDSS galaxies of $17.5 < m_r < 19.4$, and *lower panels* show the reference images centered at randomly selected positions. Left, middle and right panels correspond to images stacking $10^3, 10^4, 10^5$ images.

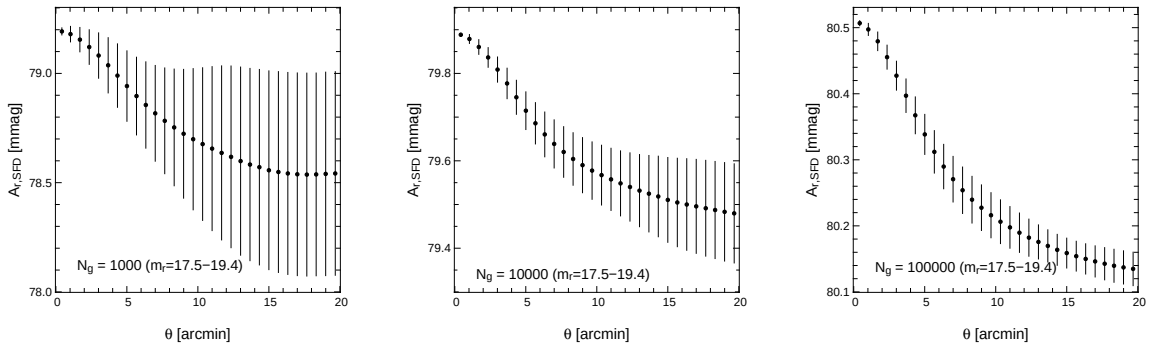

Figure 4.5: Radial profiles of the stacked images for randomly selected SDSS galaxies shown in upper panels of Figure 4.4. Left, middle, and right panels correspond to images stacking $10^3, 10^4, 10^5$ images. The error-bars indicate rms in each circular bin.

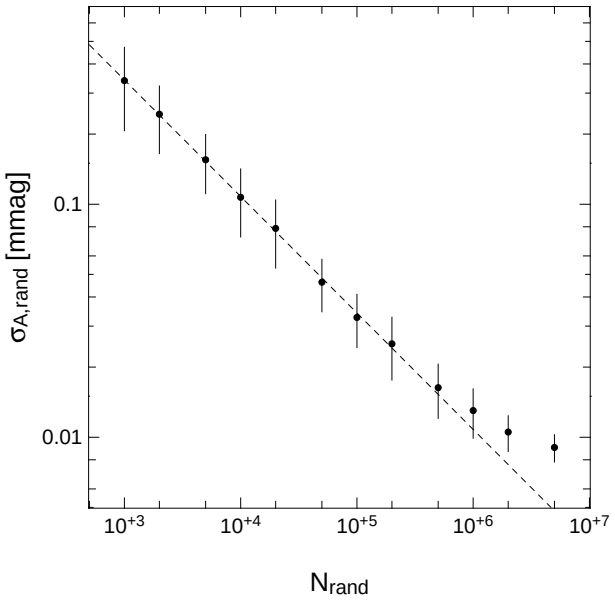

Figure 4.6: Statistical noise due to the Galactic foreground in the stacked images for randomly chosen positions. The symbols and the error-bars are computed from 100 stacked images centered at $N_{\rm rand}$ random positions. The dashed line indicates equation (4.3).

In order to evaluate the detection significance of the signal from SDSS galaxies, we repeat the stacking analysis centered at the random positions 100 times for each fixed value of $N_{\rm rand}$. We then compute rms of $A_{r,\rm SFD}$ over each stacked image, and define the average of the rms for the 100 stacked images as $\sigma_{A,\rm rand}$. Figure 4.6 shows $\sigma_{A,\rm rand}$ as a function of $N_{\rm rand}$. We find that $\sigma_{A,\rm rand}$ is well approximated by

$$\sigma_{A,\rm rand}(N_{\rm rand}) = \frac{10.8 \text{ mmag}}{\sqrt{N_{\rm rand}}}, \tag{4.3}$$

for $N_{\rm rand} < 10^6$, whereas $\sigma_{A,\rm rand}$ departs from equation (4.3) for $N_{\rm rand} > 10^6$. This is due to overlapping of the sampled regions of the SFD map, thus the $N_{\rm rand}$ random images are not independent in the case of large values of $N_{\rm rand}$. [1] Adopting $\sigma_{A,\rm rand}$ as the statistical noise due to the Galactic foreground, we evaluate the signal-to-noise ratio of the detected FIR emission of galaxies by

$$\frac{S}{N} = \frac{A_{r,\rm SFD}(\theta = 0') - A_{r,\rm SFD}(\theta = 20')}{\sigma_{A,\rm rand}(N_{\rm g})}, \tag{4.4}$$

where $A_{r,\rm SFD}(\theta)$ denotes the observed radial profile of the stacked images. For the cases of the randomly selected SDSS galaxies shown in upper panels of Figure 4.4, $S/N = 1.9, 3.8, 10.9$ for $N_{\rm g} = 10^3, 10^4, 10^5$, respectively.

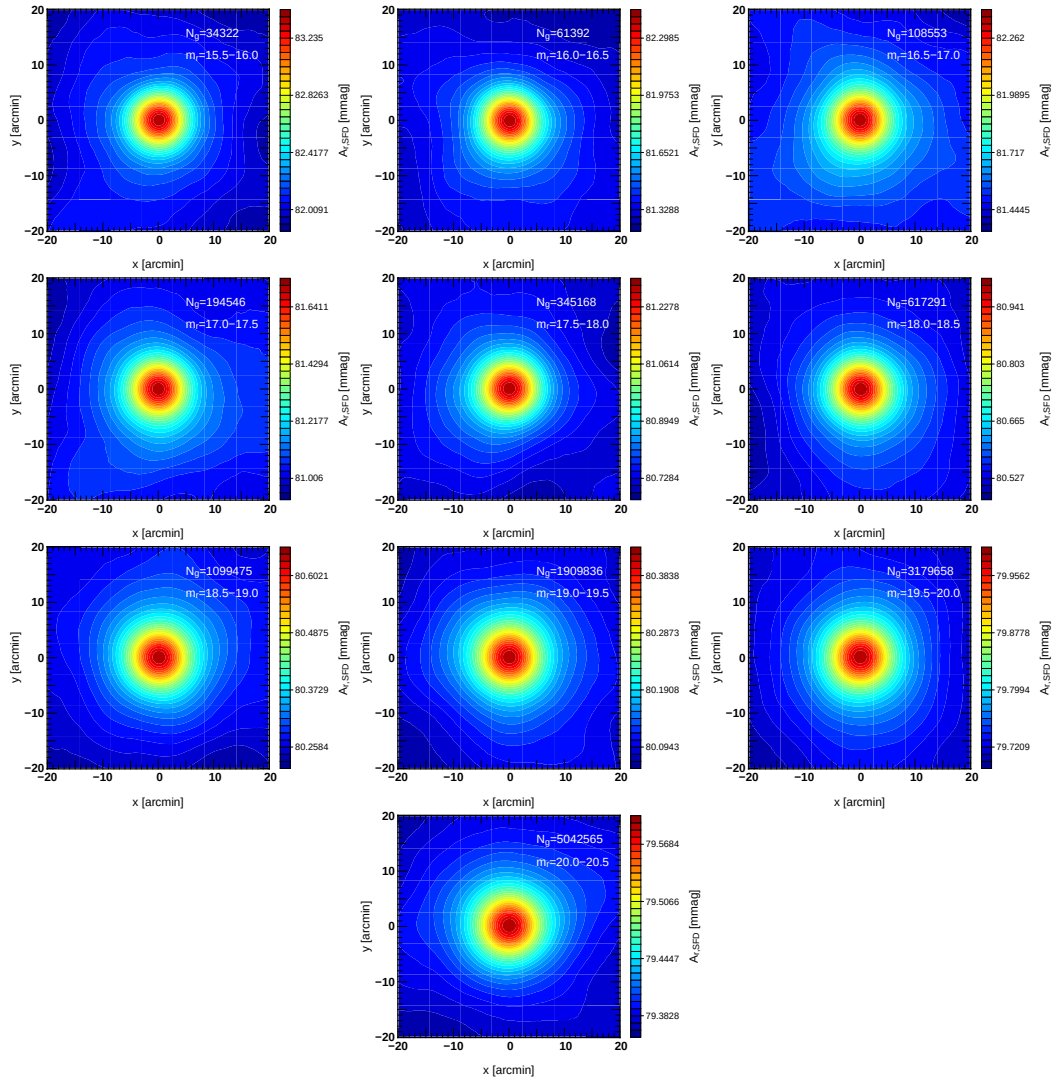

Figure 4.7: Stacked images of the SFD map for $40' \times 40'$ centered at SDSS galaxies of different r-band magnitudes ($m_r = 15.5 \sim 20.5$mag.) in 0.5 magnitude bin. The magnitude range and the number of galaxies in the range are denoted in each panel. The signal-to-noise ratio evaluated by equation (4.4) is 23.6, 26.2, 27.2, 26.9, 28.9, 30.4, 29.8, 29.9, 27.1, and 22.8, respectively, for the brightest to faintest sample.

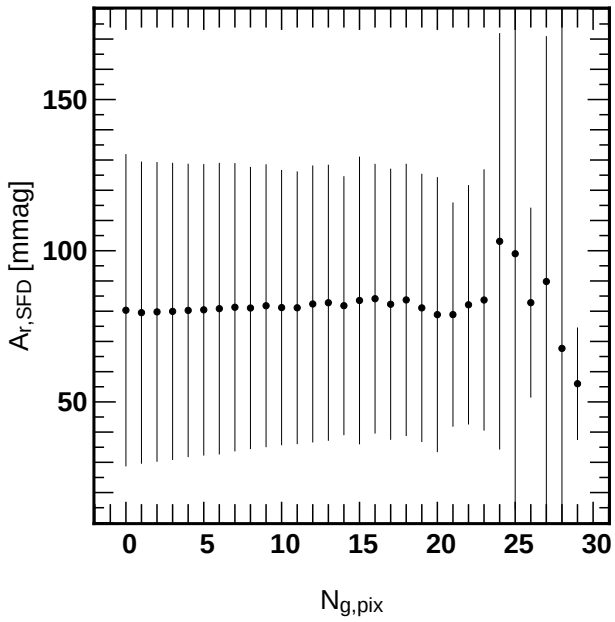

Figure 4.8: Mean values of $A_{r,\mathrm{SFD}}$ of pixels containing $N_{\mathrm{g,pix}}$ plotted against $N_{\mathrm{g,pix}}$. The quoted error bars indicate the corresponding rms.

4.2.2 Radial profiles of galaxies

To estimate the dependence of the contribution to $A_{r,\mathrm{SFD}}$, or equivalently the amount of the FIR emission, on galaxy r-band magnitudes, we stack the images at the location of galaxies according to their r-band magnitudes. The results are plotted in Figure 4.7. Thanks to the significantly large number of the SDSS galaxies, those images are highly circular, assuring that the signals do not originate from the Galactic foreground. All the angular radii of the images are very similar to the expected smoothing length of the SFD map (= $6'.1$ FWHM), and one may naively interpret that the central signal is dominated by the contribution of single galaxies at the image centers. As we will show below, however, this is not the case; in most cases the signal is rather dominated by the contribution from the nearby galaxies due to galaxy spatial clustering. Qualitatively this is understood from Figure 4.3 that shows the systematic increase of $A_{r,\mathrm{SFD}}$ as a function of numbers of galaxies in the pixel whose size is much smaller than the overall smoothing size of the SFD map.

To proceed more quantitatively, we attempt to model the radial profile of the stacked images as follows. Denote the angular profile of a single galaxy with r-band magnitude m_r as $\Sigma_{\mathrm{g}}^{\mathrm{s}}(\boldsymbol{\theta}; m_r)$. Then the statistically averaged profile of the stacked images centered at the galaxy is given by

$$\Sigma_{\mathrm{g}}^{\mathrm{tot}}(\boldsymbol{\theta}; m_r) = \Sigma_{\mathrm{g}}^{\mathrm{s}}(\boldsymbol{\theta}; m_r) + \Sigma_{\mathrm{g}}^{\mathrm{c}}(\boldsymbol{\theta}; m_r) + C, \tag{4.5}$$

where $\Sigma_{\mathrm{g}}^{\mathrm{c}}(\boldsymbol{\theta}; m_r)$ denotes the clustering term corresponding to the contribution from the nearby galaxies, and C represents the background level of the extinction. Naively, C is

[1]If we approximate the entire SDSS survey region, whose area is 7270deg^2, as a square with the side of $\sim$ 85deg, it contains the $\sim 2000 \times 2000$ pixels of the SFD map. Therefore, the number of random images that are independent each other is $N_{\mathrm{rand}} \sim 4 \times 10^6$, at most.

expected to be independent of m_r and computed from the PDF of the extinction $P(A)$ (see Figure 4.3) as

$$C = \langle A \rangle \pm \frac{\sigma_A}{\sqrt{N_{\rm g}}}, \tag{4.6}$$

where $N_{\rm g}$ is the number of stacked galaxy images, and the mean and rms are given by

$$\langle A \rangle = \int_0^\infty AP(A)dA, \tag{4.7}$$

$$\sigma_A^2 = \int_0^\infty A^2 P(A)dA - \langle A \rangle^2. \tag{4.8}$$

As we see below, however, this is not the case. Therefore we treat C as a free parameter for each magnitude bin in the fitting analysis described below. Figure 4.8 plots $\langle A \rangle$ with quoted error-bars of σ_A as a function of $N_{\rm g,pix}$.

The clustering term is written as

$$\Sigma_{\rm g}^{\rm c}(\boldsymbol{\theta}; m_r) = \iint dm' d\boldsymbol{\varphi}\ \Sigma_{\rm g}^{\rm s}(\boldsymbol{\theta} - \boldsymbol{\varphi}; m') w_{\rm g}(\boldsymbol{\varphi}; m', m_r) \frac{dN_{\rm g}(m')}{dm'}, \tag{4.9}$$

where $w_{\rm g}(\boldsymbol{\varphi}; m', m_r)$ is the angular galaxy cross-correlation function between magnitudes m' and m_r, and $dN_{\rm g}(m')/dm'$ is the differential galaxy number density.

Given the large smoothing length of the SFD map (6′.1 FWHM), a single galaxy profile is expected to be approximated by the circular Point Spread Function (PSF), independently of its intrinsic profile. Thus we adopt the Gaussian PSF profile:

$$\Sigma_{\rm g}^{\rm s}(\boldsymbol{\theta}; m_r) = \Sigma_{\rm g}^{\rm s0}(m_r) \exp\left(-\frac{\theta^2}{2\sigma^2}\right), \tag{4.10}$$

where σ is the Gaussian width of the PSF. The Gaussian approximation of the PSF is justified in Appendix A. Also we assume that the angular cross-correlation function is given as

$$w_{\rm g}(\boldsymbol{\varphi}; m', m_r) = K(m', m_r)(\varphi/\varphi_0)^{-\gamma}, \tag{4.11}$$

where the constants φ_0 and γ are assumed to be independent of m' and m_r. We adopt $\gamma = 0.75$ (Connolly et al., 2002; Scranton et al., 2002), which is valid for $\varphi < 1^\circ$. With equations (4.10) and (4.11), equation (4.9) reduces to

$$\Sigma_{\rm g}^{\rm c}(\boldsymbol{\theta}; m_r) = \Sigma_{\rm g}^{\rm c0}(m_r) \exp\left(-\frac{\theta^2}{2\sigma^2}\right) {}_1F_1\left(1 - \frac{\gamma}{2}; 1; \frac{\theta^2}{2\sigma^2}\right), \tag{4.12}$$

where ${}_1F_1(\alpha; \beta; x)$ is the confluent hypergeometric function, and

$$\Sigma_{\rm g}^{\rm c0}(m_r) = 2\pi\sigma^2 \left(\frac{\varphi_0}{\sqrt{2}\sigma}\right)^\gamma \Gamma\left(1 - \frac{\gamma}{2}\right) \int dm' \Sigma_{\rm g}^{\rm s0}(m') K(m', m_r) \frac{dN_{\rm g}(m')}{dm'}. \tag{4.13}$$

Equation (4.12) results in the extended tail due to the clustering term in addition to the Gaussian tail of the single central galaxy. The latter is negligible at $\theta \gg \sigma$, and the observed tail of the profile around galaxies is basically dominated by the clustering term.

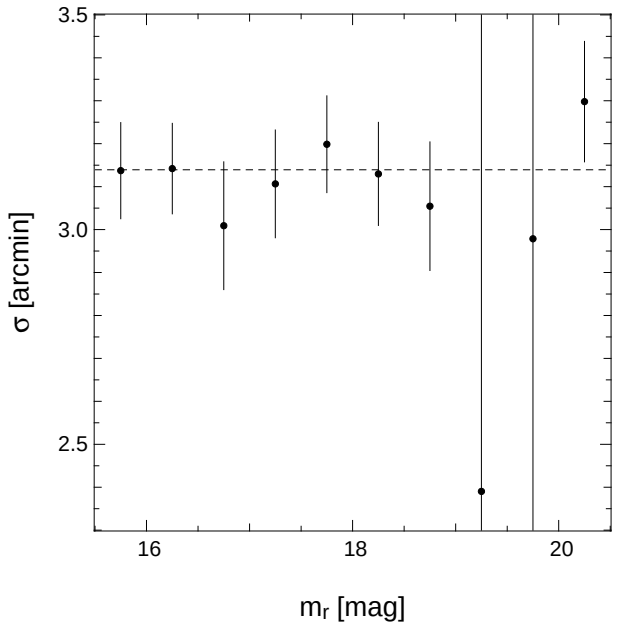

Figure 4.9: Best-fit values of the Gaussian PSF width, σ, in the case that σ is treated as a free parameter separately for different magnitudes. The error-bars computed from 400 jackknife resamplings. The dashed line indicates the error-weighted average of the all magnitude bins.

The average radial profiles of the stacked images centered at photometric galaxies are plotted in Figure 4.10. Filled circles and triangles correspond to galaxies in the different r-band magnitude ranges in Figure 4.7, and the quoted error-bars represent rms in each circular bin of $\Delta\theta = 0'.66$. The signal-to-noise ratio evaluated by equation (4.4) is $S/N = 23.6$ for the brightest sample ($15.5 < m_r < 16.0$), and $S/N = 22.8$ for the faintest sample ($20.0 < m_r < 20.5$).

We fit the observed radial profiles by equations (4.5), (4.10), and (4.12), treating $\Sigma_{\rm g}^{\rm s0}$, $\Sigma_{\rm g}^{\rm c0}$, and C as free fitting parameters for each magnitude bin. The Gaussian width of PSF, σ, is also an uncertain, since the SFD map is constructed after smoothing the IRAS data in a complicated fashion. Therefore we determine the value of σ by the radial profile fitting as follows. We first perform the model-fit to the observed profile treating σ as another free parameter separately for different magnitudes, $\sigma(m_r)$, in addition to $\Sigma_{\rm g}^{\rm s0}$, $\Sigma_{\rm g}^{\rm c0}$, and C. The resulting best-fit values of $\Sigma_{\rm g}^{\rm s0}$ and $\Sigma_{\rm g}^{\rm c0}$ are shown in Figure 4.11. The results return small negative values for $\Sigma_{\rm g}^{\rm s0}$, in the cases of $m_r > 19.0$. This would be simply due to the fact the total signal is dominated by the clustering term; the unambiguous extraction of the single galaxy contribution in those cases is difficult if we add another degree of freedom in σ for each magnitude bin. Figure 4.9 shows the best-fit values and the statistical errors of σ. In the case of $m_r < 19$, the best-fit values of σ are indeed almost independent of m_r and $\sigma = 3'.1$ as expected from our model assumption. This value of $\sigma = 3'.1$ is reasonable, given the resolution of the SFD map ($2'.59$ in Gaussian width) and the additional smoothing due to the $2'.37$ pixelization and our cloud-in-cell interpolation. This is why we constrain σ to be independent of m_r and fix as $\sigma = 3'.1$ in the actual fitting procedure below. We will discuss to what extent the result of the profile fit is affected by the fixed value of σ later.

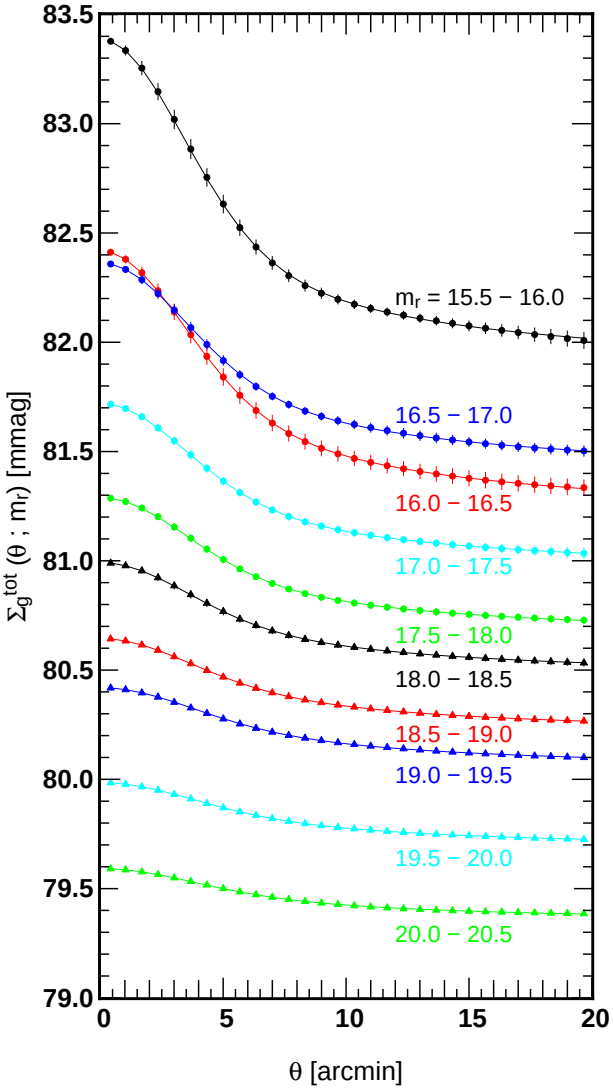

Figure 4.10: Radial profiles of stacked galaxy images corresponding to Figure 4.7. Solid curves indicate the best-fit model of equation (4.5), (4.10), and (4.12).

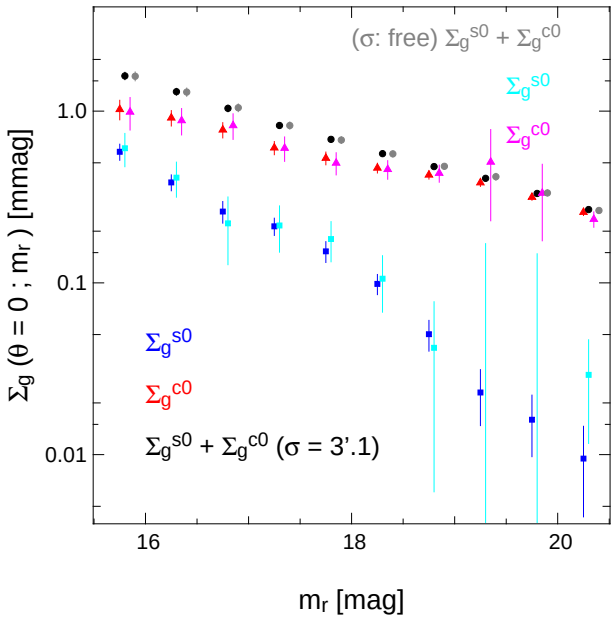

Figure 4.11: Best-fit parameters characterizing the FIR emission of galaxies against their r-band magnitude. Blue crosses, red triangles, and black circles indicate the best-fit value of Σ_g^{s0}, Σ_g^{c0}, and $\Sigma_g^{s0}+\Sigma_g^{c0}$, respectively, assuming $\sigma = 3'.1$ and $\gamma = 0.75$. The same symbols in cyan, magenta, and gray indicate the best-fit values in the case that σ is treated as a free parameter separately for each magnitude bin.

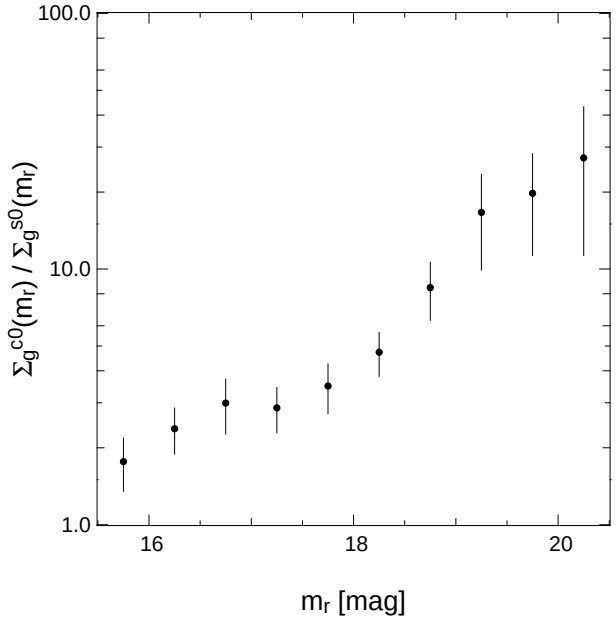

Figure 4.12: Ratio of the clustering term and the central galaxy contribution as a function of the r-band magnitude of the central galaxy.

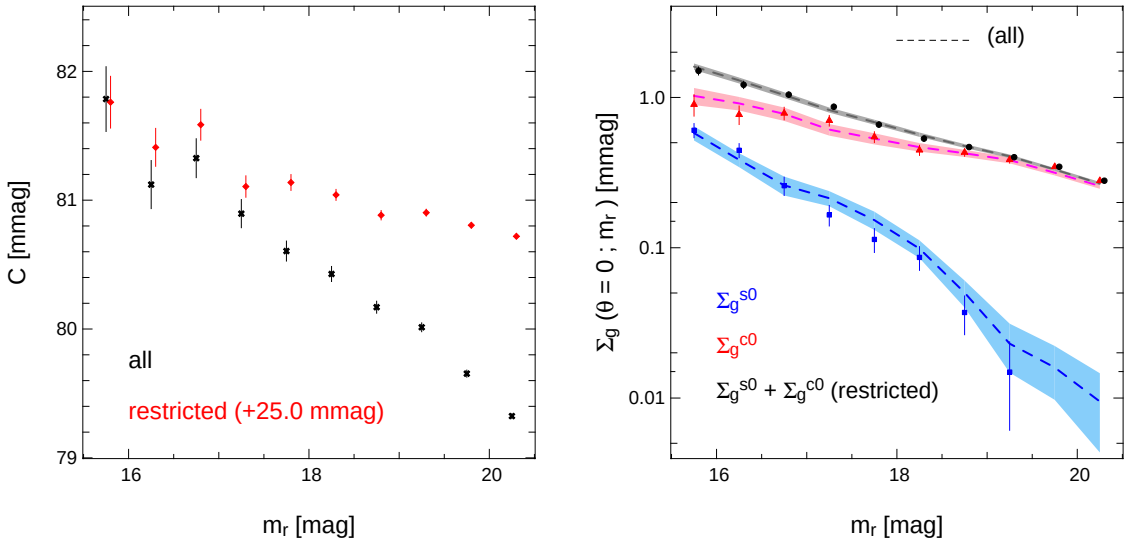

Figure 4.13: *Left panel;* The background noise level C against the r-band magnitude of the central galaxy. Black crosses indicate the results for all our sample and red ones are restricted in the inner regions shown as yellow lines in Figure 4.1. *Right panel;* The best-fit values of Σ_g^{s0} (cyan), Σ_g^{c0} (magenta), and $\Sigma_g^{s0} + \Sigma_g^{c0}$ (gray) for the restricted region. The shaded regions indicate the best-fit values for all our sample as the same as shown in Figure 4.11.

The solid curves in Figure 4.10 indicate the best-fit model of equations (4.5), (4.10), and (4.12), where we treat Σ_g^{s0}, Σ_g^{c0}, and C as the free parameters for each magnitude bin. The best-fit parameters for $\Sigma_g^{s0}(m_r)$ and $\Sigma_g^{c0}(m_r)$ are plotted in Figure 4.11. The statistical uncertainties of the best-fit parameters are evaluated from the 400 subsamples of the random jackknife resampling. The quoted error bars for each parameter are computed by marginalizing the other parameters. Since we fix the value of $\sigma = 3'.1$, the error bars are smaller than those for the case that we treat σ as a free parameter. Even at the central position of the stacked images, the FIR signals are indeed dominated by the clustering term Σ_g^c rather than the single galaxy term (see Figure 4.12).

The fitted values of the background offset term C are plotted against m_r in the left panel of Figure 4.13. Although our model assumes that C is independent of m_r, it is not the case at all; a systematic decrease of C against m_r is clearly seen. We repeated the same analysis by selecting those galaxies located in the inner contiguous regions ($160° < \alpha < 220°$, $5° < \delta < 80°$; see Figure 4.1). The results are plotted in red crosses after shifting 25 mmag, just for the ease of visual comparison. While the values of C is sensitive to the region of the map and their dependence on m_r is weaker in this case, the best-fit values for other quantities are hardly changed due to the particular choice of subregions in the SFD map as shown in the right panel of Figure 4.13. We discuss the possible origins of the systematic dependence of C on m_r in Appendix B.

Incidentally the small value of C with respect to the general trend at $16.0 < m_r < 16.5$ is the reason why the corresponding profile in Figure 4.10 does not follow the systematic trend of the other profiles.

Figure 4.14 shows to what extent the results of the profile fit are affected by the choice of γ and σ. Since the value of γ is somewhat uncertain and also depends on magnitudes, m_r

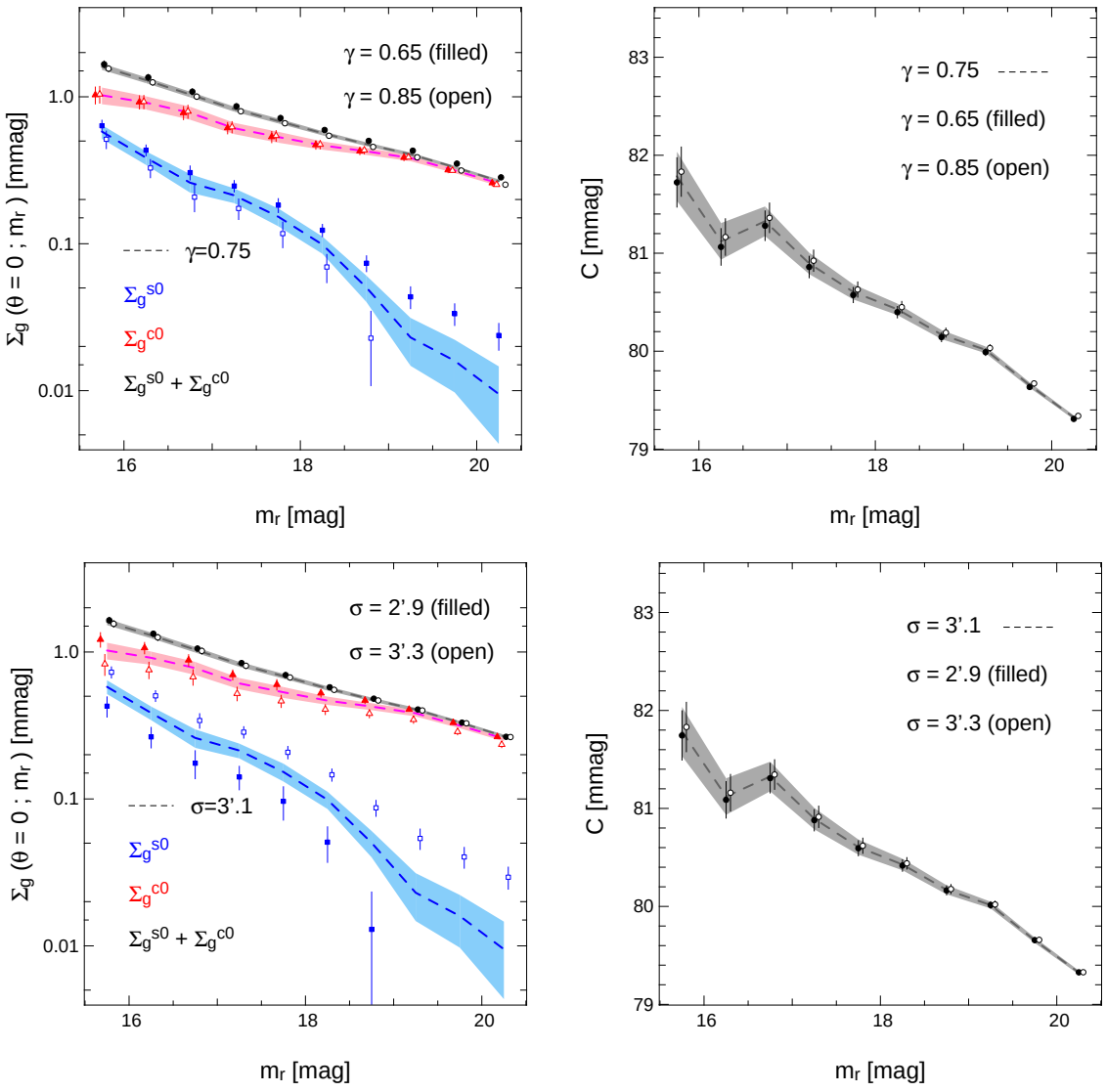

Figure 4.14: Best-fit parameters of the radial profile fit by varying the values of γ (upper panels) and σ (bottom panels). Left panels indicate the best-fit values of Σ_g^{s0} (squares), Σ_g^{c0} (triangles), and $\Sigma_g^{s0} + \Sigma_g^{c0}$ (circles). Right panels indicate the best-fit values of C. The best-fit values shown as filled (open) symbols for $\gamma = 0.65$ (0.85) and $\sigma = 2'.9$ ($3'.3$). The shaded regions indicate the best-fit value for all our sample as the same as shown in Figure 4.11.

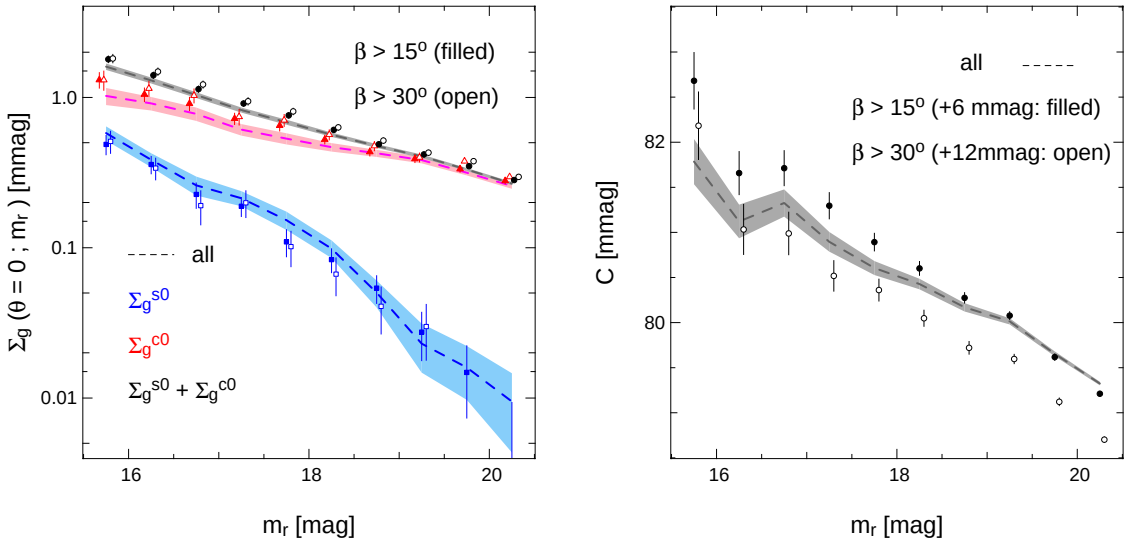

Figure 4.15: Best-fit parameters of the radial profile fit for the analysis using restricted sky area by ecliptic latitude as, $\beta > 15^{\circ}$ (filled symbols), $\beta > 30^{\circ}$ (open). Left panel indicates the best-fit values of Σ_g^{s0}, Σ_g^{c0}, and $\Sigma_g^{s0} + \Sigma_g^{c0}$. Right panel shows the best-fit values of C, which are shifted by +6 and +12 mmag, just for the ease of visual comparison. The shaded regions indicate the best-fit value for all our sample as the same as shown in Figure 4.11.

and m_r', we performed the same fitting analysis by varying the value for $0.65 < \gamma < 0.85$, which roughly covers the range of γ for our sample magnitudes. The results are shown in the upper panels of Figure 4.14, where the filled symbols show best-fit values for $\gamma = 0.65$, and open symbols for $\gamma = 0.85$. Although the best-fit values of $\Sigma_g^{s0}(m_r)$ are affected by the choice of γ, especially for the faint magnitudes, the results for $\Sigma_g^{c0}(m_r)$ hardly change.

Similarly, we repeat the fitting analysis by varying σ as $\sigma = 2'.9$ and $3'.3$, and the resulting best-fit parameters are shown in the bottom panels of Figure 4.14. The choice of σ affects the best-fit values of both $\Sigma_g^{s0}(m_r)$ and $\Sigma_g^{c0}(m_r)$, whereas the sum of those values, $\Sigma_g^{s0}(m_r) + \Sigma_g^{c0}(m_r)$, is hardly changed. This result indicates that decomposing the total signal into single and clustering terms certainly degenerates with σ, while the clustering term still dominates the single term in both cases of $\sigma = 2'.9$ and $3'.3$.

We also examine the possible effects of the residual zodiacal light in the SFD map. Figure 4.15 shows the results of the radial profile fit using the data restricted by ecliptic latitude as $\beta > 15^{\circ}$ (filled symbols) , and $\beta > 30^{\circ}$ (open). Although the best-fit values of Σ_g^{s0}, Σ_g^{c0} are not significantly affected, a closer look reveals that Σ_g^{c0} slightly increase with ecliptic latitude, which may indicate that the residual of zodiacal light systematically affects and dilutes the signal of the clustering term. The offset level C significantly varies by the choice of β, but the systematic trend against m_r still remains.

4.3 Implications

The fitting results presented in the previous section are model-independent in a sense that it does not assume any *a priori* relation between the r-band magnitude and the FIR

emission of galaxies. Therefore, the empirical relation between the optical and FIR fluxes presented in Figure 4.11 would provide the method for correcting the SFD extinction for FIR emission of galaxies, as we attempt in §5.7.

It is interesting to consider the underlying connection between the FIR emission and r-band magnitude of galaxies on the basis of the present result. Consider a galaxy with intensity profile $I_{100\mu\mathrm{m}}(\boldsymbol{\theta})$[MJy/sr]. Then its contribution to the r-band extinction should be

$$\Sigma_{\mathrm{g}}^{\mathrm{s}}(\boldsymbol{\theta}; m_r) = \left[\frac{A_r}{E(B-V)}\right] \times p \times I_{100\mu\mathrm{m}}(\boldsymbol{\theta}), \tag{4.14}$$

where $A_r/E(B-V)$ and p are the conversion factors from the color excess $E(B-V)$ to the r-band extinction and from 100μm intensity to $E(B-V)$, and are given as 2.751 and 0.0184, respectively. Integrating equation (4.14) over $\boldsymbol{\theta}$ assuming the Gaussian profile, we obtain

$$2\pi\sigma^2\Sigma_{\mathrm{g}}^{\mathrm{s0}}(m_r) = \left[\frac{A_r}{E(B-V)}\right] \times p \times f_{100\mu\mathrm{m}}\ [\mathrm{MJy}]. \tag{4.15}$$

Finally the 100μm flux, $f_{100\mu\mathrm{m}}$ is translated to the 100μm magnitude:

$$m_{100\mu\mathrm{m}} = -2.5\log(f_{100\mu\mathrm{m}}/3.63\times10^{-3}[\mathrm{MJy}]), \tag{4.16}$$

and equation (4.15) is rewritten in terms of m_r as

$$\Sigma_{\mathrm{g}}^{\mathrm{s0}}(m_r) = 36.0\times10^{-0.4m_{100\mu\mathrm{m}}}\left(\frac{3'.1}{\sigma}\right)^2. \tag{4.17}$$

Since those magnitudes, m_r and $m_{100\mu\mathrm{m}}$, should correspond to the same galaxy, their difference is equivalent to the ratio of their absolute luminosities, $L_{100\mu\mathrm{m}}/L_r$. Thus estimated ratios are plotted in Figure 4.16. The fact that the ratio for a single galaxy is approximately constant indicates that the statistically averaged ratio of FIR and optical luminosities of galaxies are independent of the r-band magnitude, which is very reasonable. For comparison, we plot the ratio for adding the clustering term in FIR. In this case the integration of $\Sigma_{\mathrm{g}}^{\mathrm{c}}(\boldsymbol{\theta}; m_r)$ over $\boldsymbol{\theta}$ does not converge because our assumed value of $\gamma(=0.75)$ is valid only for angular separation less than 1°. Thus we evaluate the flux simply by multiplying $2\pi\sigma^2$ as in the case of the Gaussian profile. Therefore $L_{100\mu\mathrm{m}}$ includes the contribution of other galaxies, but the total amplitude is subject to change depending on the more accurate profile at larger angular scales. The total ratio follows a clear single power-law and we believe that the wiggles of the ratio for single galaxies is not real but comes from the difficulty in separate the single galaxy contribution from the total signal as mentioned at the end of the previous section.

The relation between FIR and optical luminosities of galaxies can be directly probed from the sample of galaxies overlapped in the SDSS and PSCz (IRAS Point Source Catalog Redshift Survey; Saunders et al., 2000). Yahata (2007) constructed the PSCz/SDSS overlapped sample, selecting the brightest SDSS galaxy locating within 2 arcmin from each PSCz galaxy as its counterpart. In this procedure, they found SDSS optical counterpart for $\sim$ 95% of the PSCz galaxies that are located in the SDSS survey region, and the resulting sample consists of 3304 galaxies in total. For this overlapped sample, we apply the K-correction based on the "K-corrections calculator" service (Chilingarian, Melchior, & Zolotukhin , 2010) for r-band, and extrapolate the FIR spectral energy densities using second-order polynomials determined from 25, 60 μm flux for 100 μm (Takeuchi et al.,

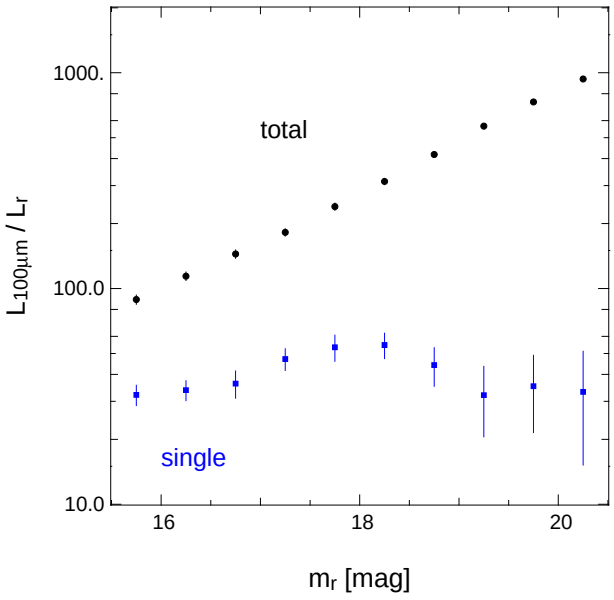

Figure 4.16: Ratio of FIR and r-band luminosities as a function of the r-band magnitude of the central galaxy. Crosses indicate the ratio for single galaxy term, while circles include the clustering term as well.

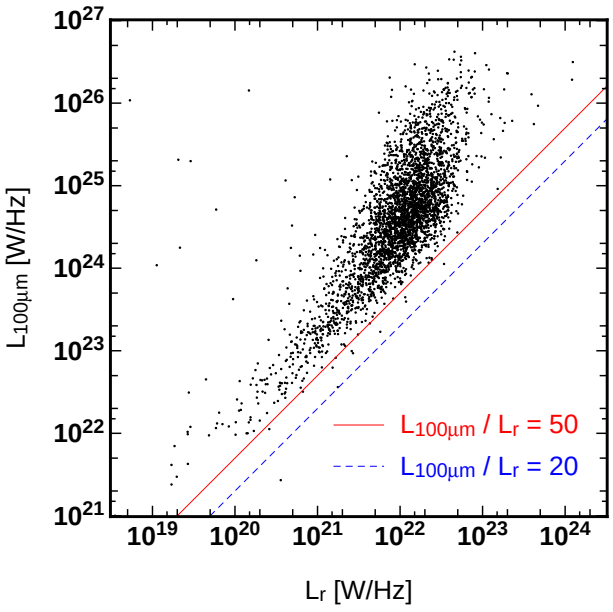

Figure 4.17: Relation between $L_{100\mu m}$ and L_r for the IRAS/SDSS overlapped galaxies. The solid and dashed lines indicate $L_{100\mu m}/L_r = 20$, and 50, respectively.

2003). Figure 4.17 is a scatter plot of $L_{100\mu\mathrm{m}}$ (PSCz) and L_r (SDSS) for the PSCz–SDSS overlapped sample of galaxies. Figure 4.17 indicates an approximate linear relation between $L_{100\mu\mathrm{m}}$ and L_r albeit with considerable scatters. The solid lines correspond to $L_{100\mu\mathrm{m}}/L_r = 20$ and 50 for reference. Thus the approximate linear relation implied from Figure 4.16 is largely consistent with Figure 4.17 since the IRAS galaxies may be preferentially biased toward the FIR brighter ones than average. In turn, this confirms that our interpretation that $\Sigma_{\mathrm{g}}^{\mathrm{s}}$ represents the contribution of a single galaxy.

4.4 Stacking analysis of SDSS DR6 quasars

Yahata et al. (2007) did not find any definite anomaly between the quasar surface densities and A_{SFD} beyond the statistical errors. Nevertheless it is interesting to repeat the stacking analysis to SDSS quasar sample as well. Indeed as we show below, we found that a weaker but similar pattern of the enhanced extinction around stacked quasar images.

For this purpose, we use the SDSS DR6 photometric quasar sample (Richards et al., 2009a,b). The analysis method is basically identical to that performed in subsection 4.2.2 except that we have to use the larger magnitude bins ($\Delta m_r = 1.0$) due to the limited number of the quasars as well as the weaker signature of the effect. The stacked images are plotted in Figure 4.18. As in the case of galaxies, we fit the radial profile to equations (4.5), (4.10), and (4.12) assuming that σ is independent of m_r. We find the best-fit value of $\sigma = 3'.13$, which is similar to that for galaxy radial profile. The radial profiles and the best-fit curves are plotted in Figure 4.19. The signal-to-noise ratio evaluated by equation (4.4) are $S/N = 1.5, 3.4, 5.0, 3.8$, and 3.2, for the brightest to the faintest magnitude sample.

Unlike galaxies, the profiles are not completely circular, and also the best-fit parameters do not exhibit regular behavior as a function of m_r. Part of the behavior may be due to the contamination of non-quasars objects in the photometric quasar sample. Therefore it would be better to repeat the analysis for the spectroscopic quasar sample, which we plan to do in due course. Nevertheless the results indicate a clear signal around the center of all the stacked images. If we look at Figure 3.7 carefully, a very weak anomaly may be recognized for photometric quasars as well. This would be consistent with our current finding of the FIR emission around those quasars in the SFD map.

It is interesting to ask if the detected FIR emission around quasars originated from (1) quasars themselves, (2) their host galaxies, (3) neighbor galaxies due to the quasar-galaxy and/or quasar host galaxy-galaxy correlation, and/or (4) some other effects (lensing, for instance). Observational studies of quasar V-band luminosity M_{q} and that of the host galaxy M_{g} imply a very weak correlation, at most, with significant scatters. Typically a quasar is one or two magnitudes brighter than its host galaxy (Hamilton, Casertano, & Turnshek, 2008; Letawe, Letawe, & Magain, 2010). Given those combined with the results for galaxies discussed in §4.3, the signal may be ascribed to the possibility (3). Recent high resolution diffuse FIR data by AKARI (Murakami et al., 2007), WISE (Wright et al., 2010), etc., will enable us to further investigate the quasar-galaxy correlation in FIR with higher statistical significance.

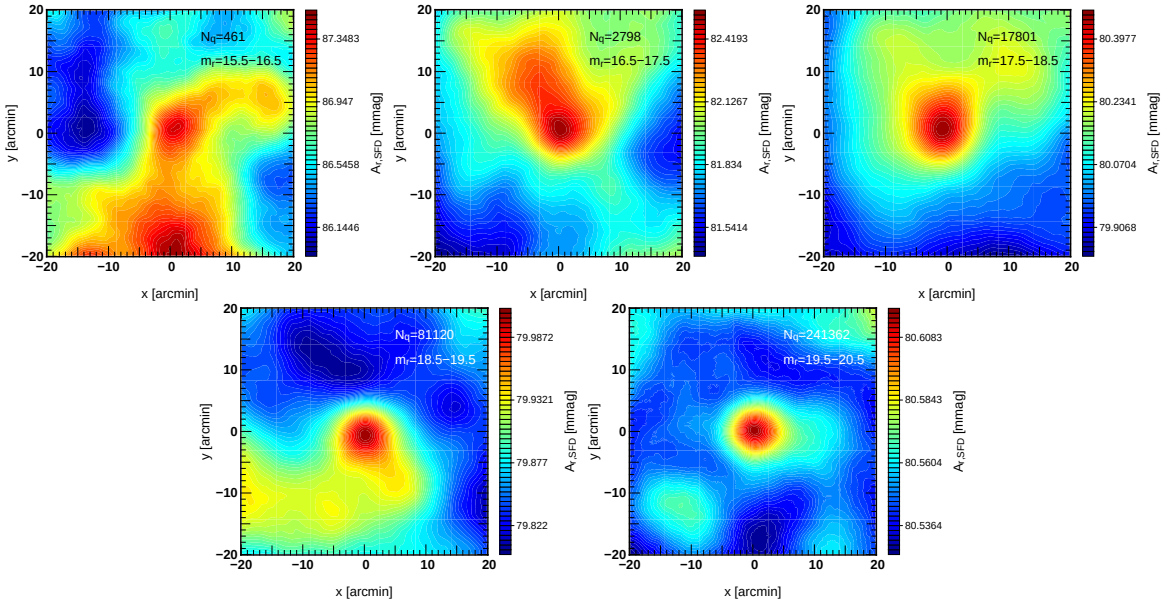

Figure 4.18: Stacked images of the SFD map for $40' \times 40'$ centered at SDSS quasars of different r-band magnitudes ($m_r = 15.5 \sim 20.5$ mag) in 1.0 magnitude bin. The magnitude range and the number of quasars in the range are denoted in each panel.

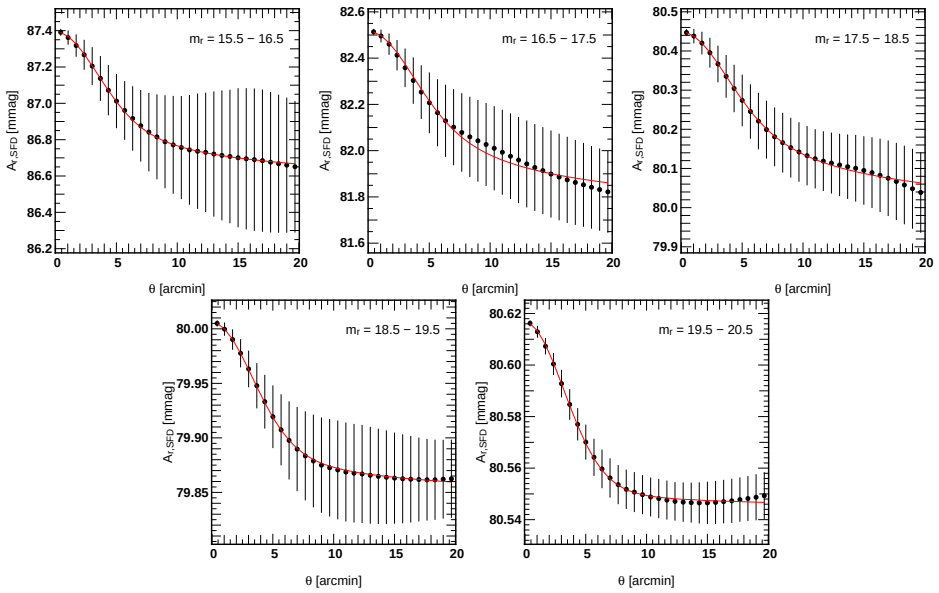

Figure 4.19: Radial profiles of stacked quasar images corresponding to Fig. 4.18. Solid curves indicate the best-fit model of equation (4.5), (4.10), and (4.12).

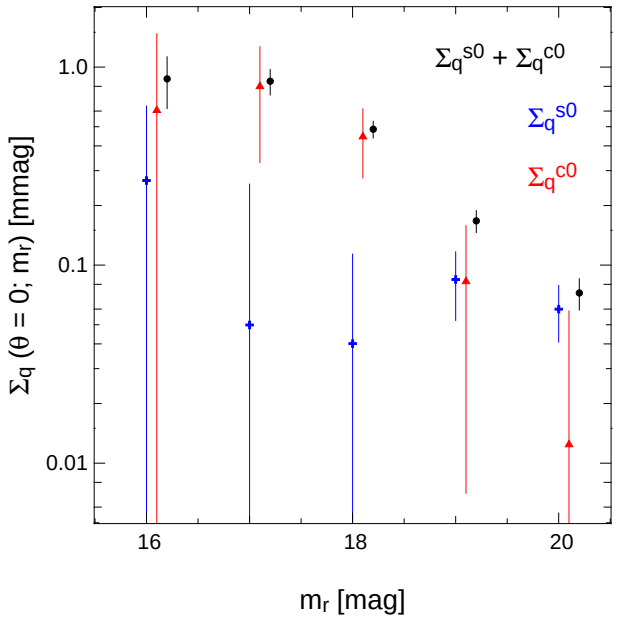

Figure 4.20: Best-fit parameters characterizing the FIR emission of quasars against their r-band magnitude.

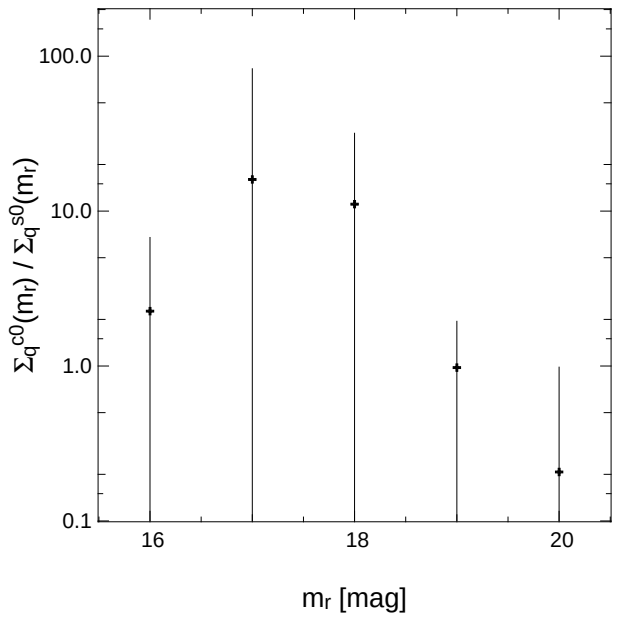

Figure 4.21: Ratio of the clustering term and the central quasar contribution as a function of the r-band magnitude of the central quasar.

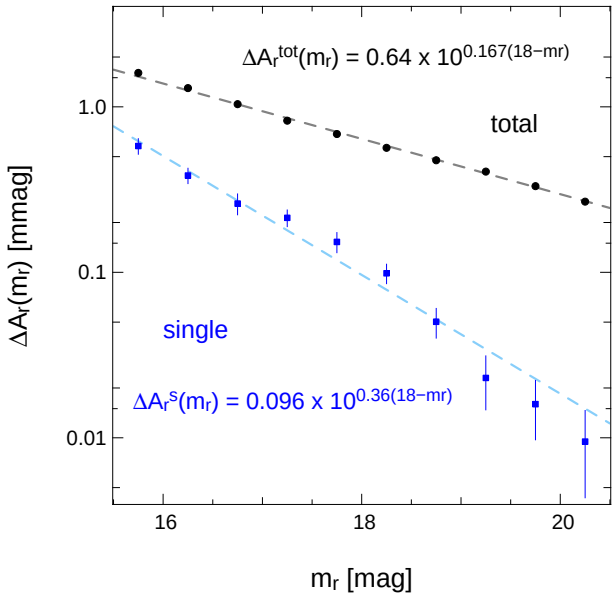

Figure 4.22: ΔA_r as a function of r-band magnitude of the central galaxy. Crosses indicate the single galaxy term, while circles include the clustering term as well.

4.5 Summary

We have detected the small but systematic contamination in the SFD Galactic extinction map due to FIR emission from galaxies. This result confirms the hypothesis of FIR contamination first suggested by Yahata et al. (2007). The amount of the contamination of the order of mmag is very small and may be negligible for most astronomical purposes. Nevertheless, the contamination is intrinsically correlated with the large-scale structure of the universe traced by galaxies, and therefore should be kept in mind in precision cosmological measurements.

The major result in this Chapter is that a galaxy of r-band magnitude m_r has an additional *contribution* to the SFD Galactic extinction by an amount of

$$\Delta A_r(m_r) = (0.096 \pm 0.008) \times 10^{(0.36\pm0.02)\times(18-m_r)} \text{ [mmag]}, \tag{4.18}$$

due to the FIR emission from itself (single term), and

$$\Delta A_r(m_r) = (0.64 \pm 0.01) \times 10^{(0.167\pm0.005)\times(18-m_r)} \text{ [mmag]}, \tag{4.19}$$

including the contribution from nearby galaxies (clustering term: Figure 4.22). Note that since the SFD determination of conversion factor p has statistical and systematic uncertainties of approximately 8%, equation (4.18) and (4.19) would have the similar level of uncertainties.

The detection of the FIR emission of galaxies is the direct evidence of the FIR contamination in the SFD map, and qualitatively consistent with the hypothesis proposed by Yahata et al. (2007) as the origin of the anomaly in the SFD map. This empirical relation provides the model-independent constraints on the amount of FIR contamination in the SFD map, which is confronted to the observed anomaly in the surface number densities of galaxies in the next Chapter.

Chapter 5

Modeling the anomaly of the SFD map on the contamination of galaxy FIR emission

In the previous chapter, we detected and measured the FIR emission of galaxies contaminated in the SFD map, which is of the order of 0.1 to 1 mmag in r-band extinction. Our next task is to ask if the detected amount of the FIR emission of galaxies properly accounts for the observed anomaly in the surface number density of SDSS galaxies.

For that purpose, we first repeat the surface number density analysis of galaxies using the SDSS DR7 data set. Next we construct an analytic method to compute the surface density of galaxies taking account of the contamination of their FIR emission. Then we consider the required amount of FIR emission of galaxies to reproduce the observed anomaly, which can be directly compared to that measured by the stacking analysis. We also present our attempts to correct the SFD map for the FIR contamination.

5.1 The Sloan Digital Sky Survey DR7

In the following number count analysis, we use the photometric galaxy sample from SDSS DR7, selected according to each five passband of SDSS; u, g, r, i, and z. Following Yahata et al. (2007), we impose a magnitude range as $17.5 < m_r < 19.4$ for r-band, which is more conservative than that adopted in the previous Chapter.

Figure 5.1 shows the differential number counts of SDSS galaxies as a function of m_x for each bandpass. The faint-end threshold of our r-band selected sample, $m_r = 19.4$, is ~ 2 mag brighter than the turnover of the differential number count. We similarly determine the faint-end of magnitude range for the other bandpasses as 2 mag brighter than the turnover magnitude. We confirmed that shifting the upper or lower limits by ± 1.0mag does not significantly change our conclusions below. We adopt the same value of upper/lower limits for both extinction-uncorrected and corrected magnitudes.

We adopt the same criteria for the sky area (§4.1.1) and the photometry flags (§4.1.2) as in the previous Chapter. We summarize the magnitude range and the number of galaxies with and without photometry flag selection for each bandpass in Table 5.1.

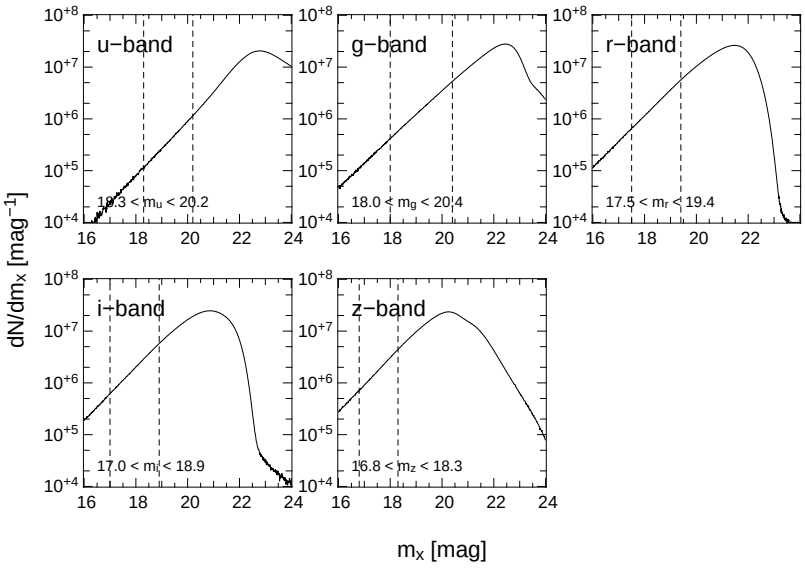

Figure 5.1: Differential number counts of the photometric galaxy sample as functions of extinction uncorrected magnitudes for each band (solid lines). The vertical dashed lines indicate the magnitude ranges within which we use for the analysis.

Table 5.1: The magnitude range and the number of SDSS galaxies for each bandpass. The third column shows the number of all SDSS galaxies within the magnitude range. The fourth column shows the number of the galaxies after photometry flag selection described in §4.1.2, which are used in our measurement in §5.2. The numbers of galaxies are counted without extinction correction.

bandpass	magnitude range	# of galaxies (w/o flag selection)	# of galaxies (w/ flag selection)	rejection rate
u	$18.3 < m_u < 20.2$	1200586	633319	0.472
g	$18.0 < m_g < 20.4$	4891030	3428064	0.299
r	$17.5 < m_r < 19.4$	4347881	3205638	0.263
i	$17.0 < m_i < 18.9$	4450724	3140684	0.295
z	$16.8 < m_z < 18.3$	2984104	2136639	0.284

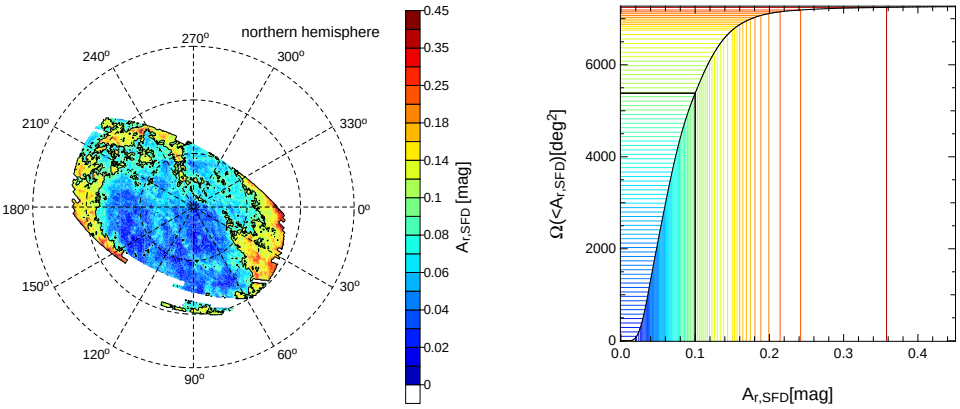

Figure 5.2: Photometric survey area of the SDSS DR7 in Galactic coordinates (*left panel*), and the cumulative distribution of the area as a function of $A_{r,\mathrm{SFD}}$ (*right panel*). The left panel is color-coded according to the value of $A_{r,\mathrm{SFD}}$. The thick lines in the both panels indicate $A_{r,\mathrm{SFD}} = 0.1$mag, corresponding to 74 % of the entire survey. The thin lines correspond to each bin of 84 subregions color-coded as the same as the left panel.

5.2 Surface number densities of SDSS DR7 photometric galaxies

5.2.1 Methodology

In this section, we extend the previous analysis of Yahata et al. (2007), and re-examine the anomaly in the surface number density of galaxies using the SDSS DR7 photometric galaxies, instead of DR4. The left panel of Figure 5.2 plots the sky area of the SDSS DR7 that is employed in our analysis, where the color scale indicates the value of the r-band extinction provided by SFD, $A_{r,\mathrm{SFD}}$.

Since most of the increased survey area of DR7 relative to DR4 corresponds to regions with $A_{r,\mathrm{SFD}} < 0.1$mag, we can study the anomaly in such low-extinction regions discovered by Yahata et al. (2007) with higher statistical significance.

We first divide the entire sky area of the SDSS DR7 (right panel of Figure 5.2) into 84 subregions according to the value of $A_{r,\mathrm{SFD}}$. Each subregion is chosen so as to have an approximately same area ($\sim 100\mathrm{deg}^2$), and consists of spatially separated (disjoint) small patches over the sky. (Figure 5.3 illustrates the example of disjoint subregions in the case that the entire sky area is divided into three.) The right panel of Figure 5.2 shows the cumulative area fraction of the sky as a function of $A_{r,\mathrm{SFD}}$. Note that approximately 74 % of the entire sky corresponds to $A_{r,\mathrm{SFD}} < 0.1$mag, in which we are interested.

Next we count the number of galaxies with the specified range of magnitudes in each subregion, and obtain their surface number densities as a function of the extinction. Since the spatial distribution of galaxies is expected to be homogeneous when averaged over a sufficiently large area, the surface number densities of galaxies should be constant, and should not correlate with the extinction. In other words, any systematic trend with respect to $A_{r,\mathrm{SFD}}$ should indicate to a problem of the SFD map.

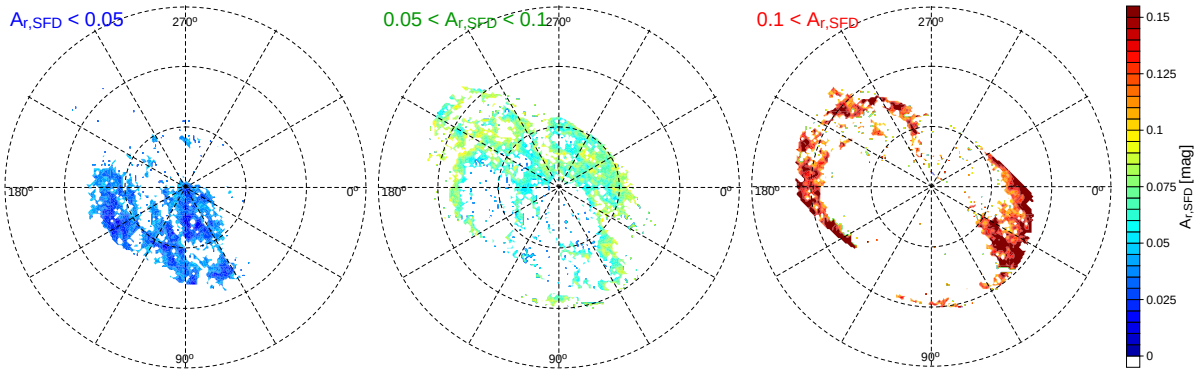

Figure 5.3: Examples of disjoint subregions in the case that all the SDSS sky area is divided into three subregions. *Left, center,* and *right panel* correspond to the subregions where $A_{r,\mathrm{SFD}} < 0.05$, $0.05 < A_{r,\mathrm{SFD}} < 0.1$, and $0.1 < A_{r,\mathrm{SFD}}$, respectively.

5.2.2 Results

Figure 5.5 shows the surface number densities of galaxies, S_{gal}, in the 84 subregions for the five passbands. The red filled circles indicate S_{gal} uncorrected for dust extinction, while the blue filled triangles are the results after extinction correction using the SFD map. Note that the surface number densities of galaxies in different passpands are plotted against their corresponding r-band extinction, $A_{r,\mathrm{SFD}}$.

Following Yahata et al. (2007) again, we estimate the statistical error of the surface number density, σ_S^2, as follows:

$$\frac{\sigma_S^2}{S^2} = \frac{1}{N} + \frac{1}{\Omega^2}\int_\Omega\int_\Omega w(\theta_{12})d\Omega_1 d\Omega_2, \tag{5.1}$$

where N and S denote the number and the surface number density of the galaxies in the subregion of area Ω, and $w(\theta_{12})$ is the angular correlation function of galaxies with θ_{12} being the angular separation between two solid angle elements, $d\Omega_1$ and $d\Omega_2$. The first term in equation (5.1) denotes the Poisson noise, while the second term comes from galaxy clustering.

For definiteness, we adopt the double power-law model (Scranton et al., 2002; Fukugita et al., 2004) for $w(\theta_{12})$:

$$w(\theta_{12}) = \begin{cases} 0.008(\theta_{12}/\mathrm{deg})^{-0.75} & (\theta_{12} \leq 1\mathrm{deg}) \\ 0.008(\theta_{12}/\mathrm{deg})^{-2.1} & (\theta_{12} > 1\mathrm{deg}). \end{cases} \tag{5.2}$$

Strictly speaking, the integration in the second term of equation (5.1) should be performed over a complex and disjoint shape of each subregion. For simplicity, however, we substitute the integration over a circular region whose area is equal to that of the actual subregion. Although this approximation may overestimate the true error, it does not affect our conclusion at all. Figure 5.4 shows the fractional error, σ_S/S, computed from equation (5.1) and (5.2) as a function of Ω, where we adopted $S = 500$ deg^{-2}. For the typical value of $\Omega \sim 100\mathrm{deg}^2$, the second term is larger by two orders of magnitude than the first Poisson-noise term.

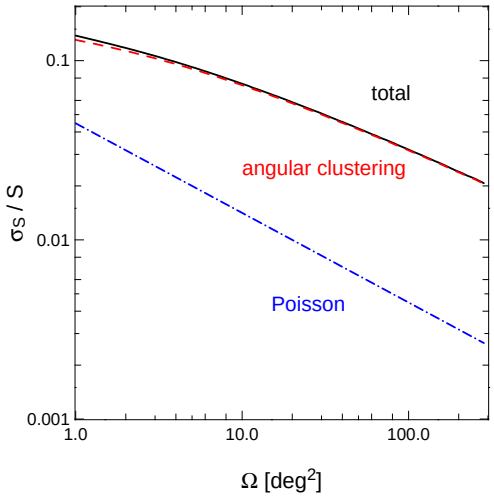

Figure 5.4: Fractional error of the surface number densities computed from equation (5.1) and (5.2), assuming $S = 500\mathrm{deg}^2$ (solid line). Dott-dashed and dashed lines indicate the contributions of the first term (Poisson noise) and the second term (galaxy angular clustering) of equation (5.1).

Figure 5.5 suggests that the SFD correction works well in relatively high-extinction regions, *i.e.,* $A_{r,\mathrm{SFD}} > 0.1$; before corrected for extinction, the surface number density of galaxy, S_{gal}, monotonically decreases against $A_{r,\mathrm{SFD}}$ as naturally expected. It becomes roughly constant within the statistical error after extinction correction.

In low-extinction regions ($A_{r,\mathrm{SFD}} < 0.1$), however, the uncorrected S_{gal} *increases* with $A_{r,\mathrm{SFD}}$, which is opposite to the behavior expected from the Galactic dust extinction. The anomalous positive correlation between surface number densities and extinction is even more enhanced after the extinction correction. Apart from the slight quantitative differences, these results are consistent with the trend discovered for the SDSS DR4 by Yahata et al. (2007), especially for the positive correlations in $A_{r,\mathrm{SFD}} < 0.1$.

In what follows, we examine to what extent the FIR emission of galaxies detected by the stacking analysis (Chapter 4) accounts for the observed anomaly that we described here. Hereafter, we consider the surface number density of the galaxies measured in r-band alone, simply because it is the central SDSS passband, and the result is equally applicable to the other passbands.

5.3 Mock numerical simulation to compute the FIR contamination effect of galaxies on the extinction map

In this section, we present the results of mock numerical simulations that take into account the effect of the FIR emission of mock galaxies in a fairly straightforward manner. First we randomly place mock galaxies over the SDSS DR7 sky area so that they have the same number density and the same r-band magnitude distribution of the SDSS DR7 sample. Next, we assign a 100μm flux to each mock galaxy according to the probability distribution

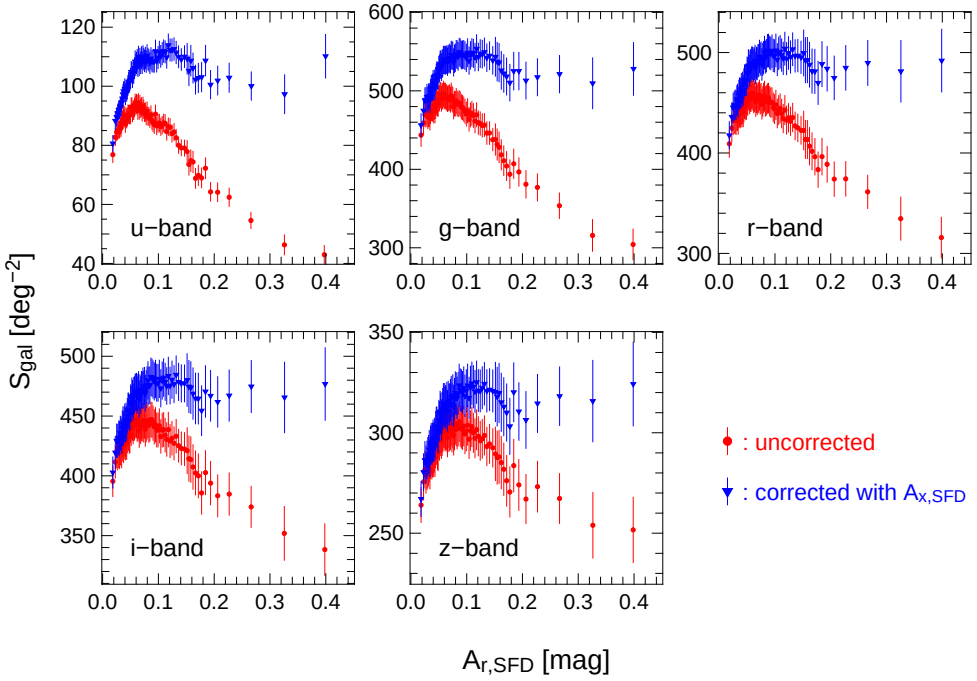

Figure 5.5: Surface number densities of the SDSS DR7 photometric galaxy sample corresponding to Figure 5.1, against $A_{r,\mathrm{SFD}}$. The circles/triangles indicates the surface number densities calculated with extinction un-corrected/corrected magnitudes, respectively. The statistical errors are calculated from equation (5.1). The horizontal axis is the mean of $A_{r,\mathrm{SFD}}$ over the galaxies in each subregion.

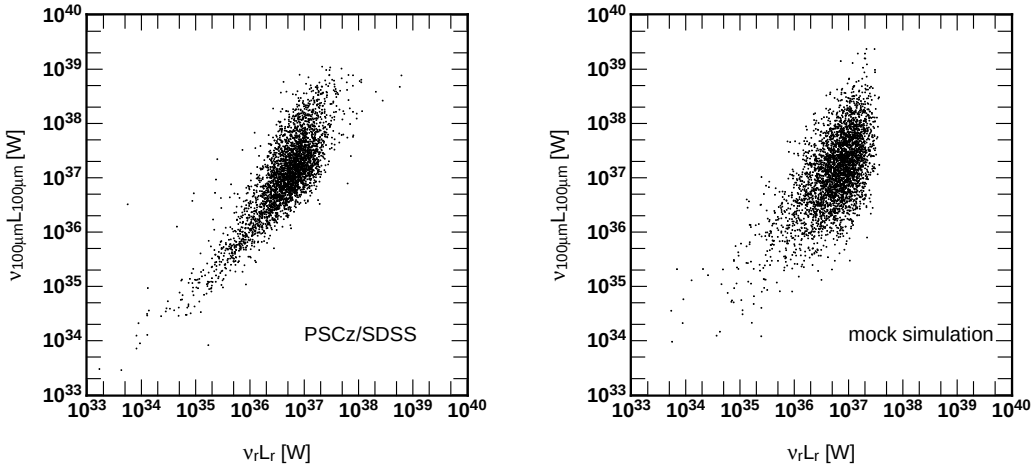

Figure 5.6: *Left panel*; Relation between $\nu_{100\mu\mathrm{m}}L_{100\mu\mathrm{m}}$ and $\nu_r L_r$ for the PSCz/SDSS overlapped galaxies. *Right panel* same as the left panel, but for the mock particles generated based on r-band luminosity function (equation 5.7), the log-normal PDF of y adopting the parameters in equation (5.13), and the flux cut $f_{100\mu\mathrm{m}} < 1.0$Jy.

function discussed in §5.3.1. We sum up the 100μm fluxes of the mock galaxies over the raw SFD map that is assumed to be *not contaminated* by the FIR emission of mock galaxies, and construct a *contaminated* mock extinction map. Finally, we compute the surface number densities of mock galaxies exactly as we did for the real galaxy sample. Further details are described below.

5.3.1 Empirical correlation between 100μm and r-band luminosities of PSCz/SDSS galaxies

In order to assign 100μm emission to each mock galaxy with a given r-band magnitude, we need an empirical relation between the two luminosities, $L_{100\mu\mathrm{m}}$ and L_{r}. For that purpose, we use the sample of 3304 galaxies that are detected both in SDSS and PSCz (Yahata, 2007, See §4.3 for more details). Note, however, that the sample is biased towards the FIR luminous galaxies since SDSS optical magnitude-limit is significantly deeper than that of PSCz galaxies.

The left panel of Figure 5.6 shows the relation between $\nu_{100\mu\mathrm{m}}L_{100\mu\mathrm{m}}$ (PSCz) and $\nu_r L_r$ (SDSS) of the PSCz/SDSS overlapped sample. The resulting scatter plot indicates that $L_{100\mu\mathrm{m}}$ and L_r are approximately proportional, albeit with considerable scatter. So we compute the probability distribution function (PDF) of the luminosity ratio,

$$y \equiv \frac{\nu_{100\mu\mathrm{m}}L_{100\mu\mathrm{m}}}{\nu_r L_r}, \tag{5.3}$$

for the sample (solid histogram in Figure 5.7), and find that the PDF is reasonably well described by a log-normal distribution:

$$P_{\mathrm{ratio}}(y)dy = \frac{1}{y\ln 10\sqrt{2\pi\sigma^2}}\exp\left[-\frac{(\log_{10} y-\mu)^2}{2\sigma^2}\right]dy, \tag{5.4}$$

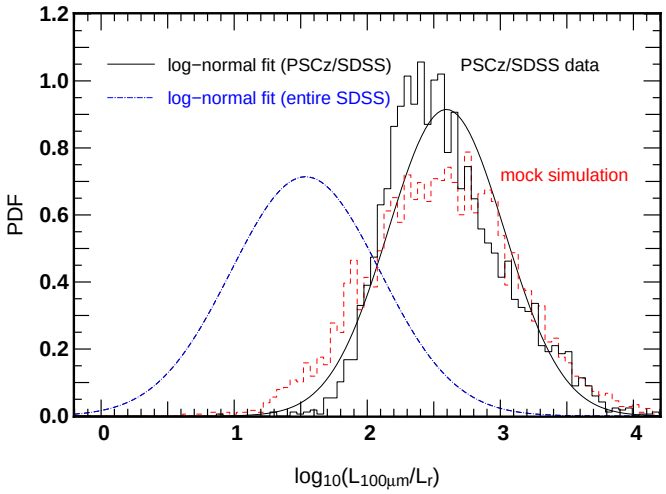

Figure 5.7: The probability distribution function of $L_{100\mu m}/L_r$; the PSCz/SDSS overlapped sample (histogram), the best-fit log-normal function (black solid curve), flux-limited mock galaxies (red dashed histogram), and the best-fit log-normal function estimated for the entire SDSS galaxies (blue dot dashed curve).

where $\mu = 0.393$ and $\sigma = 0.428$ are the mean and dispersion of $\log_{10} y$ (solid curve in Figure 5.7).

Since the PSCz/SDSS overlapped sample is a biased sample in a sense that these galaxies are selected towards the FIR luminous galaxies, the above log-normal distribution is not necessarily applicable for the entire SDSS galaxies. Therefore we assume the FIR-optical luminosity ratio of the *entire* SDSS galaxies also follows a log-normal distribution, and estimate the values of μ and σ for the entire sample by considering the PSCz detection limit. Although the flux limit of PSCz is defined through $f_{60\mu m} > 0.6$Jy, we roughly estimate the corresponding effective flux limit at 100μm is $f_{100\mu m} > 1.0$Jy from the distribution of $f_{100\mu m}$ for the PSCz/SDSS galaxies (Left-panel of Figure 5.6).

Armed with these assumptions, the number of the galaxies that are detected by this flux cut and have the luminosity between $L_r \sim L_r + dL_r$ and $L_{100\mu m} \sim L_{100\mu m} + dL_{100\mu m}$ is calculated as,

$$N^{\rm obs}(L_r, L_{100\mu m}) dL_r dL_{100\mu m} = \frac{\Omega_s}{4\pi}\left[\int_0^\infty dz \frac{dV(<z)}{dz}\Theta(L_{100\mu m}, z)\Phi(L_r)P(L_{100\mu m}|L_r;\mu,\sigma)\right] dL_r dL_{100\mu m}, \quad (5.5)$$

where Ω_s is the solid angle of the PSCz/SDSS overlapped survey area, and $V(<z)$ denotes the co-moving volume up to redshift z. The step function $\Theta(L_{100\mu m}, z)$ describes the flux cut of PSCz:

$$\Theta(L_{100\mu m}, z) = \begin{cases} 1 & (L_{100\mu m}/4\pi d_L^2(z) > 1.0\text{Jy}) \\ 0 & (else), \end{cases} \quad (5.6)$$

where $d_L(z)$ is the luminosity distance at redshift z.

We adopt the double-Schechter luminosity function in r-band measured from the SDSS

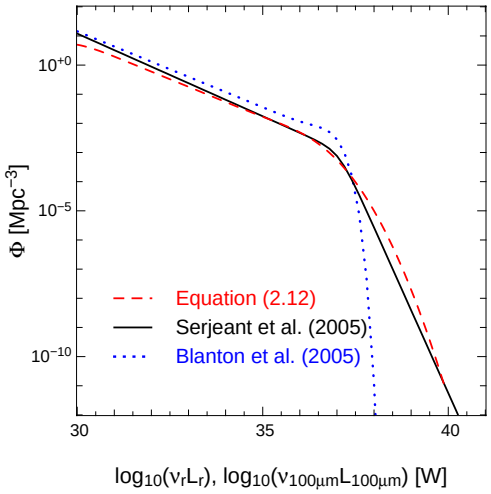

Figure 5.8: Luminosity function (LF) of galaxies at 100μm and r-band. Solid line is 100μm LF directly measured from the PSCz data (Serjeant & Harrison, 2005), while dashed line shows our estimate of 100μm LF based on equation (5.9) with the best-fit μ, σ and r-band LF (Blanton et al., 2005b, blue dotted line).

DR2 data (Blanton et al., 2005b) for $\Phi(L_r)$:

$$\Phi(L_r)dL_r = \frac{dL_r}{L_{r,*}} \exp\left(-\frac{L_r}{L_{r,*}}\right)\left[\phi_{*,1}\left(\frac{L_r}{L_{r,*}}\right)^{\alpha_1} + \phi_{*,2}\left(\frac{L_r}{L_{r,*}}\right)^{\alpha_2}\right]. \tag{5.7}$$

The conditional probability density function of $L_{100\mu\mathrm{m}}$ for given L_r is assumed to be log-normal:

$$\begin{aligned} P(L_{100\mu\mathrm{m}}|L_r;\mu,\sigma)dL_{100\mu\mathrm{m}} &= \frac{1}{\ln 10\sqrt{2\pi\sigma^2}} \exp\left(-\frac{[\log(\nu_{100\mu\mathrm{m}}L_{100\mu\mathrm{m}}/\nu_r L_r) - \mu]^2}{2\sigma^2}\right)\frac{dL_{100\mu\mathrm{m}}}{L_{100\mu\mathrm{m}}} \\ &= yP_{\mathrm{ratio}}(y;\mu,\sigma)\frac{dL_{100\mu\mathrm{m}}}{L_{100\mu\mathrm{m}}}. \end{aligned} \tag{5.8}$$

We use equation (5.5) to find the best-fit μ and σ in equation (5.8) for the *entire* SDSS galaxies that reproduce the observed distribution of the PSCz/SDSS overlapped sample. The resulting values are $\mu = -0.662$ and $\sigma = 0.559$ as plotted in blue dot-dashed line in Figure 5.7. This result indicates that the mean value of y of the PSCz/SDSS overlapped sample is biased by an order of magnitude relative to that for the entire galaxies; see equation (5.12) and (5.13).

Adopting now the best-fit log-normal distribution, the luminosity function at 100μm is calculated as

$$\Phi(L_{100\mu\mathrm{m}}) = \int_0^\infty dL_r \Phi(L_r) P(L_{100\mu\mathrm{m}}|L_r;\mu,\sigma). \tag{5.9}$$

As plotted in Figure 5.8, the above best-fit indeed agrees well with the luminosity function independently measured from the PSCz data (Serjeant & Harrison, 2005).

In order to make sure if the above FIR log-normal PDF combined with the FIR flux cut reproduces the left panel of Figure 5.6, we generate particles and assign z, L_r, and $L_{100\mu\mathrm{m}}$ following the redshift distribution $dV(<z)$, and equations (5.7) and (5.8).

Then we exclude those particles with $f_{100\mu\mathrm{m}} < 1.0$Jy to mimic the flux cut. The right panel of Figure 5.6 and the dashed histogram in Figure 5.7 show the resulting luminosity distribution and the PDF of y for those particles. Although not perfect, the mock particles reproduce the observed distribution reasonably well. We suspect that the discrepancy between the observed data and the mock simulation is mainly due to the limitation of our log-normal approximation neglecting the dependence of the ratio $L_{100\mu\mathrm{m}}/L_{60\mu\mathrm{m}}$ on $L_{100\mu\mathrm{m}}$.

For simplicity of the procedure, however, we adopt the best-fit log-normal distribution as the fiducial model of the 100 μm flux of the SDSS galaxies in what follows. In doing so, we parametrize the distribution by y_{avg} and y_{rms} instead of μ and σ:

$$y_{\mathrm{avg}} = e^{\mu \ln 10 + (\sigma \ln 10)^2/2}, \tag{5.10}$$

$$y_{\mathrm{rms}} = e^{\mu \ln 10 + (\sigma \ln 10)^2/2} \sqrt{e^{(\sigma \ln 10)^2} - 1}, \tag{5.11}$$

since the anomaly is basically determined by y_{avg} as will be shown in Figure 5.11 below. For definiteness, the PSCz/SDSS overlapped sample is characterized by

$$\mu = 0.393, \sigma = 0.428, y_{\mathrm{avg}} = 4.015, y_{\mathrm{rms}} = 5.143, \tag{5.12}$$

while the entire SDSS sample is estimated to have

$$\mu = -0.662, \sigma = 0.559, y_{\mathrm{avg}} = 0.499, y_{\mathrm{rms}} = 1.026. \tag{5.13}$$

5.3.2 Simulations

Now we are in a position to present our mock simulations that exhibit the effect of the FIR contamination of galaxies. In this subsection, we neglect the spatial clustering of galaxies and consider the case for Poisson distributed mock galaxies. The effect of spatial clustering of galaxies will be discussed separately in §5.6.1. Our mock simulations are performed as follows.

1. We distribute random particles as mock galaxies over the SDSS DR7 survey area. The number of the particles is adjusted so as to approximately match that of the SDSS photometric galaxies.

2. We assign an intrinsic apparent magnitude in r-band to each mock galaxy so that the resulting magnitude distribution reproduces that of the SDSS galaxies (Figure 5.1).

3. Assign 100μm flux to each mock galaxy adopting the log-normal PDF for the 100μm-to-r-band flux ratio, y. The PDF is characterized by y_{avg} and y_{rms}.

4. We convolve the 100μm fluxes of the mock galaxies with a FWHM = 5$'$.2 Gaussian filter, so as to mimic the SFD resolution, FWHM = 6$'$.1 (see also Appendix C). Those mock galaxies with 100 μm flux being larger than 1.0Jy are excluded, since SFD individually subtracted the 100μm emission of those bright galaxies. We include only the contribution of the mock galaxies with $17.5 < m_{\mathrm{r}} < 19.4$ so as to be consistent with our analysis in §5.2.2. We note, however, that in reality the FIR contamination would be likely contributed by galaxies outside the magnitude range (not only SDSS galaxies but non-SDSS galaxies that do not satisfy the SDSS

selection criteria). Therefore the current mock simulation should be interpreted to see the extent to which the SDSS galaxies in that magnitude range alone account for the observed anomaly in their surface number density.

5. We superimpose the 100μm intensity of the mock galaxies on a true extinction map and construct a contaminated extinction map after subtracting the background (*i.e.,* mean) level of the mock galaxy emission. In what follows, the resulting extinction with mock galaxy contaminated is denoted as A'_r.

6. Finally, we calculate $S_{\rm mock}$, surface number densities of mock galaxies whose corrected/uncorrected magnitudes lie between 17.5 and 19.4 mag, repeating the same procedure discussed in §5.2, but using A'_r instead.

Note that our mock analysis uses the SFD map as the true extinction map without being contaminated by FIR emission of *mock* galaxies. Of course, the SFD map is contaminated by FIR emission from *real* galaxies, and thus cannot be regarded as a *true* extinction map for them. Nevertheless the contamination of real galaxies should not be correlated at all with the mock galaxies. This is why the SFD map can be used as the true extinction map for the current simulation.

The *observed* magnitude of each mock galaxy, *i.e.,* affected by the Galactic dust absorption alone, is calculated from the true, in the present case the SFD map, but the extinction correction is done using A'_r. Note that the difference between the true map and the contaminated map affects the value of extinction of regions where mock galaxies are located. Therefore, surface number densities of mock galaxies *before* the extinction correction are also influenced by the FIR contamination.

Figure 5.9 shows the surface number densities of mock galaxies as a function of A'_r. Here we adopt $y_{\rm avg} = 0.499$ and $y_{\rm rms} = 1.026$, i.e., equation (5.13) which are estimated for the entire SDSS galaxy sample. The quoted error bars in the panel reflect the Poisson noise alone. The results exhibit a similar, but significantly weak correlation with $A_{r,{\rm SFD}}$ at $A_{r,{\rm SFD}} < 0.1$ compared to the observed one (Fig.5.5), especially for the extinction-uncorrected surface densities.

Figure 5.10 would help us to understand the origin of the anomaly intuitively. (In this plot, we have adopted $y_{\rm avg} = 10$ and $y_{\rm rms} = 5$ just to clearly visualize the trends discussed in the following.) The dashed line indicates the differential distribution of the sky area as a function of $A_{r,{\rm SFD}}$, $\Omega(A_{r,{\rm SFD}})$, which corresponds to the derivative of the left panel of Figure 5.2. The black solid line shows the same distribution, but as a function of A'_r. The resulting $\Omega'(A'_r)$ slightly differs from $\Omega(A_{r,{\rm SFD}})$ due to the FIR contamination of mock galaxies.

The blue and red solid lines in Figure 5.10 show the differential number counts of galaxies, $N'_{\rm gal,uncorr}$ and $N'_{\rm gal,corr}$, as a function of A'_r calculated from magnitudes uncorrected/corrected for extinction with A'_r. The shapes of $N'_{\rm gal,uncorr}$ and $N'_{\rm gal,corr}$ are slightly shifted towards the right relative to $\Omega'(A'_r)$, because the pixels with more galaxies suffer from the larger contamination and thus have larger values of A'_r.

Although the amount of this shift is quite small on average, the differences between Ω' and the differential number counts for the same A'_r become larger in low-extinction regions because Ω' is a rapidly increasing function of A'_r. Therefore the surface number densities, $N'_{\rm gal,uncorr}$ or $N'_{\rm gal,corr}$ divided by Ω', drastically change especially in low-extinction regions. In other words, the correlation between the surface number densities and A'_r is significantly

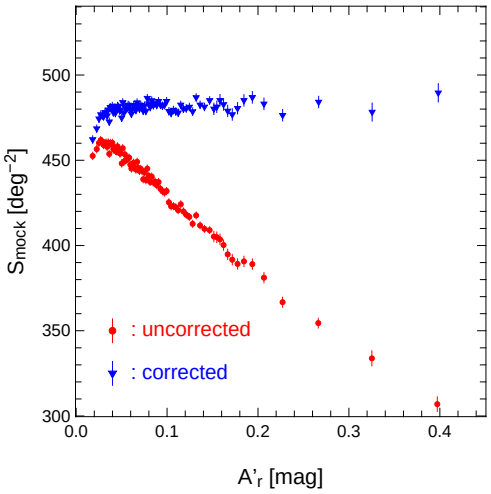

Figure 5.9: The surface number densities of the randomly distributed mock galaxies with assigned magnitude of $17.5 < m_r < 19.4$. The symbols are the same as in Figure 5.5. The values of $y_{\rm avg}$ and $y_{\rm rms}$ estimated for the entire SDSS galaxies are adopted, instead of those for the PSCz/SDSS overlapped sample. The error bars reflect the Poisson noise alone.

enhanced due to the nature of the SDSS sky area and the SFD map. This also implies that the shape of the anomaly in $S_{\rm gal}$ is basically determined by the functional form of $\Omega(< A)$.

We also investigate how this result is affected by the 100μm emission of galaxies outside the magnitude range. We incorporate the 100μm flux of mock galaxies within a wider magnitude range ($15.0 < m_r < 21.0$), but the result is almost indistinguishable. This is mainly because that the additional contamination is not directly correlated with the surface number densities that we measure, partly because we neglect spatial clustering of galaxies. Therefore it affects only as the statistical noise in the extinction map, and does not contribute to the systematic correlation.

Finally we examine the dependence of the surface number densities on the parameters of $y_{\rm avg}$ and $y_{\rm rms}$ for log-normal PDF of y (Fig. 5.11). The results indicate stronger correlations for larger $y_{\rm avg}$, but turn out to be relatively insensitive to $y_{\rm rms}$. This is why we choose $y_{\rm avg}$ and $y_{\rm rms}$, instead of μ and σ, to parametrize the log-normal PDF. A closer look reveals that larger $y_{\rm rms}$ shows slightly weaker anomaly, since a larger fraction of the mock galaxies are brighter than the IRAS/PSCz flux limit and does not contribute to FIR contamination. This effect of flux limit becomes critical for very large $y_{\rm avg}$ and $y_{\rm rms}$, as we will see in §5.5.1.

As seen above, the mock result adopting equation (5.13) estimated for the *entire* SDSS galaxies (Fig 5.9) indicates disagreement with the observed anomaly (Fig 5.5). This result may appear to imply that the hypothesis of galaxy FIR contamination fails to explain the observed anomaly. This is, however, not the case because we have neglected spatial clustering of galaxies. The previous parameters for the entire SDSS are estimated from the contribution of each single galaxy itself, but in the presence of galaxy clustering, the FIR emission associated with that galaxies can be significantly enhanced by the neighbor galaxies. In fact, the stacking analysis in the previous Chapter revealed that the FIR

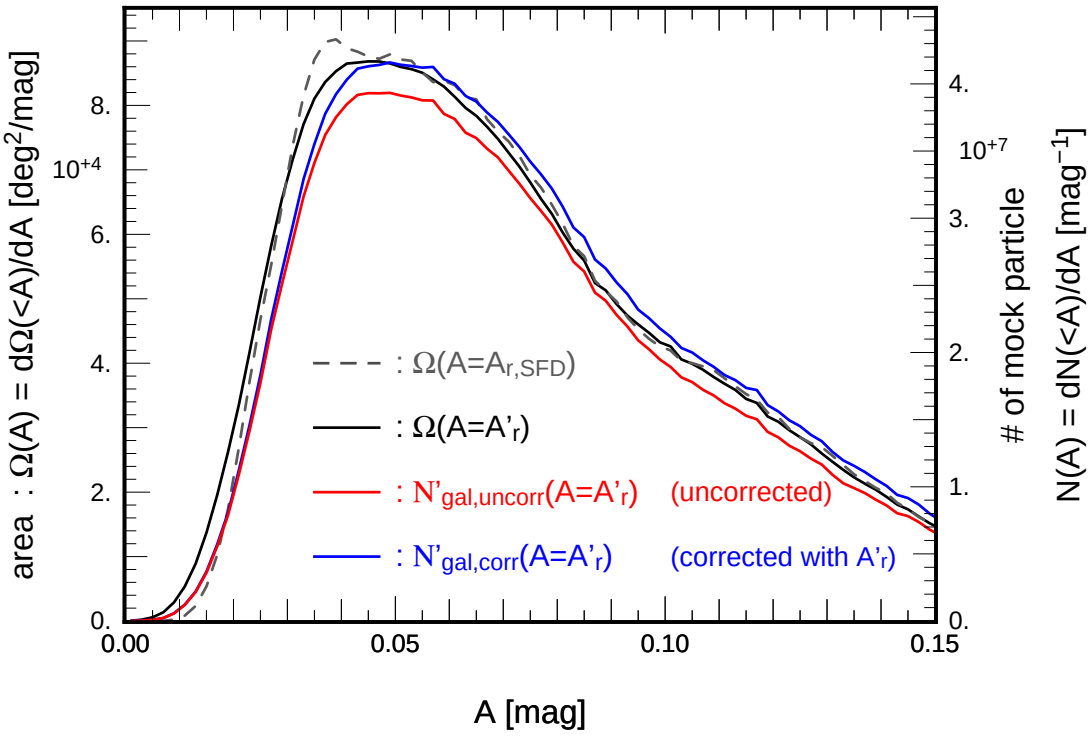

Figure 5.10: The distribution of sky area and mock galaxies. The dashed line is the distribution of sky area as a function of *true* extinction, A, and the solid black line is calculated as a function of contaminated extinction, $A+\Delta A$. The red (blue) line indicates the distribution of number of galaxies as a function of contaminated extinction, $A+\Delta A$, with uncorrected (corrected) using the contaminated extinction. The distributions of number of galaxies are divided by the average surface number density, therefore surface number densities are equal to the average at the points where the distribution of sky area and number of galaxies cross. We have adopted $y_{\rm avg} = 10$ and $y_{\rm rms} = 5$ for clear visualization of the differences between each lines.

emission of neighbor galaxies dominate the central galaxy even by an order of magnitude. Therefore, we should adopt $y_{\rm avg}$ and $y_{\rm rms}$ that represent the total contribution both for each single galaxy and clustering neighbor galaxies, in order to reproduce the observed anomaly by our Poisson mock simulation.

In principle, we can probe such FIR fluxes from the comparison between mock simulations and observations, but the simulations are very time-consuming. Thus we develop an analytic model that reproduces the mock results in the next section.

5.4 Analytic model of the FIR contamination

In this section, we develop an analytic model that describes the anomaly of surface number densities of galaxies due to their FIR emission. The reliability of the analytic model is checked against the result of the numerical simulations presented in the previous section. We present a brief outline in the next subsection, and the details are described in Appendix D.

5.4.1 Outline

Let A define the *true* Galactic extinction, not contaminated by the galaxy emissions. We denote the sky area whose value of the *true* extinction is between A and $A+dA$ by $\Omega(A)dA$, and the number of galaxies that are located in the area $\Omega(A)dA$ by $N_{\rm gal}(A)dA$. Since there is no spatial correlation between galaxies and the Galactic dust, the corresponding surface number densities of the galaxies as a function of A:

$$S(A) \equiv \frac{N_{\rm gal}(A)}{\Omega(A)} \tag{5.14}$$

should be independent of A and constant within the statistical error.

If the FIR emission from galaxies contaminates the *true* extinction, however, the above quantities should depend on the contaminated extinction, A', which are defined as $\Omega'(A')$ and $N'_{\rm gal}(A')$, respectively. Thus the *observed* surface number densities, $S'(A')$, should be

$$S'(A') = \frac{N'_{\rm gal}(A')}{\Omega'(A')}. \tag{5.15}$$

The essence of our analytic model is how to compute the expected $\Omega'(A')$ and $N'_{\rm gal}(A')$ under the presence of the FIR contamination of galaxies, which are distorted from the given *true* $\Omega(A)$ and $N_{\rm gal}(A)$.

Due to its angular resolution, the FIR emission of multiple galaxies contaminate to the extinction in the SFD map at a given position. Thus we need to sum up the FIR emission contribution of those galaxies located within the angular resolution scale:

$$A' = A + \Delta A, \tag{5.16}$$

where the additional extinction, ΔA, is computed by summing up the contribution of the i-th galaxies ($i = 1 \sim N$) located in the pixel:

$$\Delta A = \sum_{i=1}^{N} \Delta A_i. \tag{5.17}$$

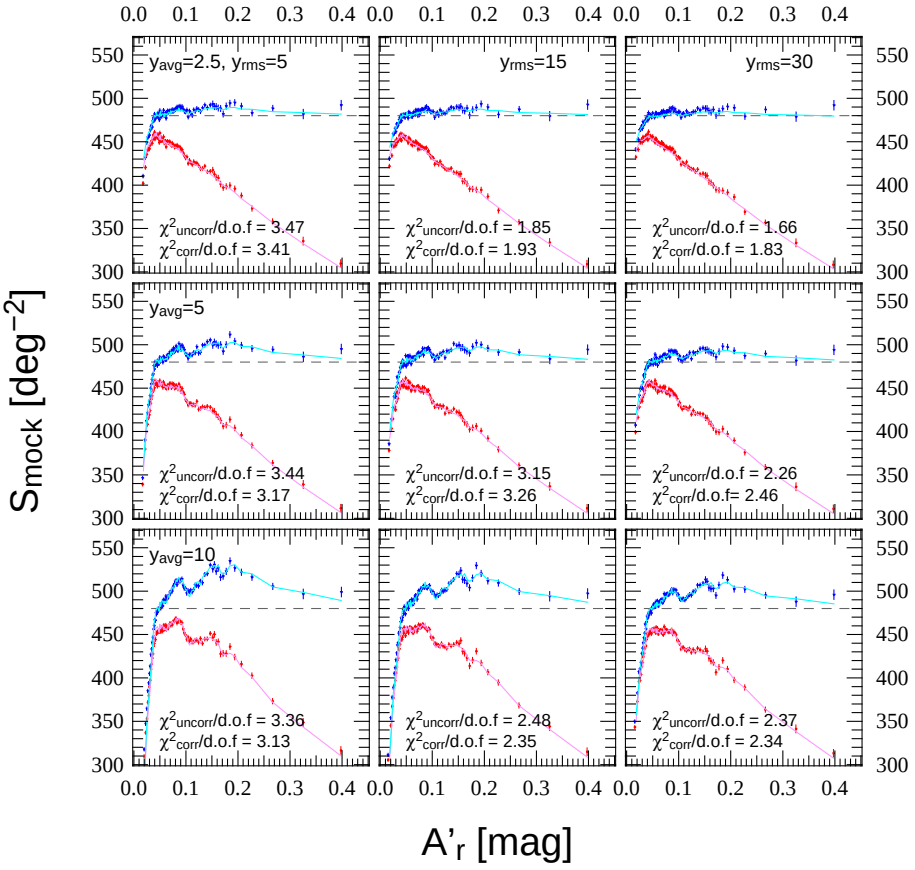

Figure 5.11: The results of the mock simulations with Poisson distributed sample for various parameters of the log-normal PDF of y. The symbols indicate the results of the simulation for the mock Poisson sample, the same as Figure 5.9. The error bars reflect the Poisson noise alone. The cyan and pink lines indicate the analytic model prediction from equations (5.18) and (5.19) in §5.4. The lines and symbols are the same as Figure 5.9. The goodness of agreement between Poisson mock simulation and analytic model are evaluated by reduced χ^2 for extinction un-corrected/corrected one, where only Poisson noise is considered. For all panels, the same average surface number density, $\bar{S} = 480\mathrm{deg}^{-2}$, is assumed and shown as gray dashed lines.

In order to perform the summation analytically, we need a joint probability distribution function, $P_{\rm joint}(\Delta A, N)$, corresponding to the situation where there are N galaxies in a pixel of the dust map, and the total contribution of those galaxies is ΔA. In Appendix D, we present a prescription to compute $P_{\rm joint}(\Delta A, N)$, and provide the integral expressions for $\Omega'(A')$ and $N'_{\rm gal}(A')$.

5.4.2 Application of the analytic model

The analytic expressions for $\Omega'(A')$, $N'_{\rm gal,corr}(A')$ and $N'_{\rm gal,uncorr}(A')$ are given in equations (D.8), (D.19) and (D.20) in Appendix D. Thus one can compute the surface number densities for the i-th subregion of the extinction between A'_i and A'_{i+1} as

$$S'_{\rm corr,i} = \frac{\int_{A'_i}^{A'_{i+1}} N'_{\rm gal,corr}(A')dA'}{\int_{A'_i}^{A'_{i+1}} \Omega'(A')dA'}, \tag{5.18}$$

$$S'_{\rm uncorr,i} = \frac{\int_{A'_i}^{A'_{i+1}} N'_{\rm gal,uncorr}(A')dA'}{\int_{A'_i}^{A'_{i+1}} \Omega'(A')dA'}, \tag{5.19}$$

where $S'_{\rm corr}$ and $S'_{\rm uncorr}$ are the extinction-corrected and uncorrected surface number densities, respectively. The solid lines in Figure 5.11 show the surface number densities calculated from equations (5.18) and (5.19) adopting 9 parameter sets of $y_{\rm avg}$ and $y_{\rm rms}$. The horizontal axis, an average extinction in each subregion, is calculated as

$$A'_{\rm corr,i} = \frac{\int_{A'_i}^{A'_{i+1}} A' N'_{\rm gal,corr}(A')dA'}{\int_{A'_i}^{A'_{i+1}} N'_{\rm gal,corr}(A')dA'}, \tag{5.20}$$

$$A'_{\rm uncorr,i} = \frac{\int_{A'_i}^{A'_{i+1}} A' N'_{\rm gal,uncorr}(A')dA'}{\int_{A'_i}^{A'_{i+1}} N'_{\rm gal,uncorr}(A')dA'}. \tag{5.21}$$

Figure 5.11 clearly indicates that the analytic predictions and the simulation results are in good agreement. Strictly speaking, the agreement is not perfect in a sense that the reduced χ^2 is as large as ~ 3.5 for the worst cases, when only the Poisson noise is considered. The statistical errors for the observed SDSS surface number densities (Figure 5.5), however, includes the variance due to spatial clustering and are larger than the Poisson noise by an order of magnitude. Thus the discrepancy between the mock simulation and the analytic model is negligible for the parameter-fit analysis to the observational result in the following section.

5.5 Comparison of FIR contamination with the observed anomaly

Given the success of the analytic model described above, we compare the model prediction with the observed SFD anomaly. Our discussion in this section is organized as follows.

(1) We attempt to find the optimal values of $y_{\rm avg}$ and $y_{\rm rms}$ by fitting the analytic model prediction to the observed anomaly. It turns out that the observed anomaly is reproduced fairly well with a relatively wide range of $y_{\rm avg}$ and $y_{\rm rms}$ as long as $y_{\rm avg}$ is larger than ~ 4.

(2) This value should be compared with with the empirical, and thus model-independent, result $y_{\rm avg} \approx 2.8$ obtained from the stacking analysis in Chapter 5. The fact that the rough agreement of the two independent estimates for the average FIR to r-band fluxes is interpreted as a supporting evidence for our FIR explanation of the observed SFD anomaly.

(3) Finally, we attempt to reproduce the FIR flux of SDSS galaxies required above within our framework of the simplified modeling for FIR-to-optical relation. This estimate qualitatively explains the result (2), but not quantitatively. We suspect that this is due to the limitation of our FIR assignment model for galaxies, and not the basic flaw of the FIR explanation for the SFD anomaly. Namely, given the fact that the stacking analysis already indicates the barely required value for $y_{\rm avg}$, we have to refine the FIR assignment model for SDSS galaxies, rather than to rule out the FIR explanation itself.

5.5.1 Estimating of the FIR emission of galaxies from the observed anomaly

Given the success of the analytic model described above, we attempt to find the best-fit parameters, $y_{\rm avg}$, and $y_{\rm rms}$, to the observed anomaly by minimizing

$$\chi^2(y_{\rm avg}, y_{\rm rms}, \bar{N}) = \sum_i \frac{(S^{\rm obs}_{\rm uncorr,i} - S'_{\rm uncorr,i})^2}{\sigma^2_{\rm obs,i}}, \tag{5.22}$$

where $S^{\rm obs}_{\rm uncorr,i}$ is the extinction-*uncorrected* surface number densities in the i-th subregion of extinction, $\sigma_{{\rm obs},i}$ is its statistical errors, and $S'_{\rm uncorr,i} = S'_{\rm uncorr,i}(y_{\rm avg}, y_{\rm rms}, \bar{N})$ is the analytic model prediction given by equation (5.19). In the present fit, we use the extinction-uncorrected surface number densities, but the result is almost the same even if we use $S_{\rm corr}$ instead. In addition to $y_{\rm avg}$ and $y_{\rm rms}$, we include another free parameter, the intrinsic average number of galaxy in a pixel, $\bar{N}$, which is also unknown since the extinction correction is not necessarily reliable. It turns out that $\bar{N}$ is in the range of 480 to 500[deg^{-2}] and the results below is not sensitive to this value.

In reality, however, the resulting constraints are not so strong as shown in the top-left panel in Figure 5.12. This is partly due to the fact that we simply compute $\sigma_{{\rm obs},i}$ from the variance of each extinction bin, which does not represent the proper error. Thus our analysis here should be interpreted as a qualitative attempt to find a possible parameter space to explain the anomaly in terms of the FIR contamination; it would be quite difficult to make more quantitative analysis, given several crude approximations in our theoretical modeling and the poor angular-resolution and uncertain dust temperature correction in the SFD map.

Bearing this remark in mind, let us consider the constraints on $y_{\rm avg} - y_{\rm rms}$ plane from the observed anomaly shown in the top-left panel of Figure 5.12. Fairly acceptable fits are obtained over the bluish region. Just for illustration, we select two widely separated points A and B with $(y_{\rm avg}, y_{\rm rms}) = (15, 300)$ and $(3.8, 4.0)$, respectively, and plot the corresponding analytical predictions in the other three panels. Even though their $y_{\rm avg}$ is different by an order of magnitude, the two sets of parameters account for the observed anomaly reasonably and equally well.

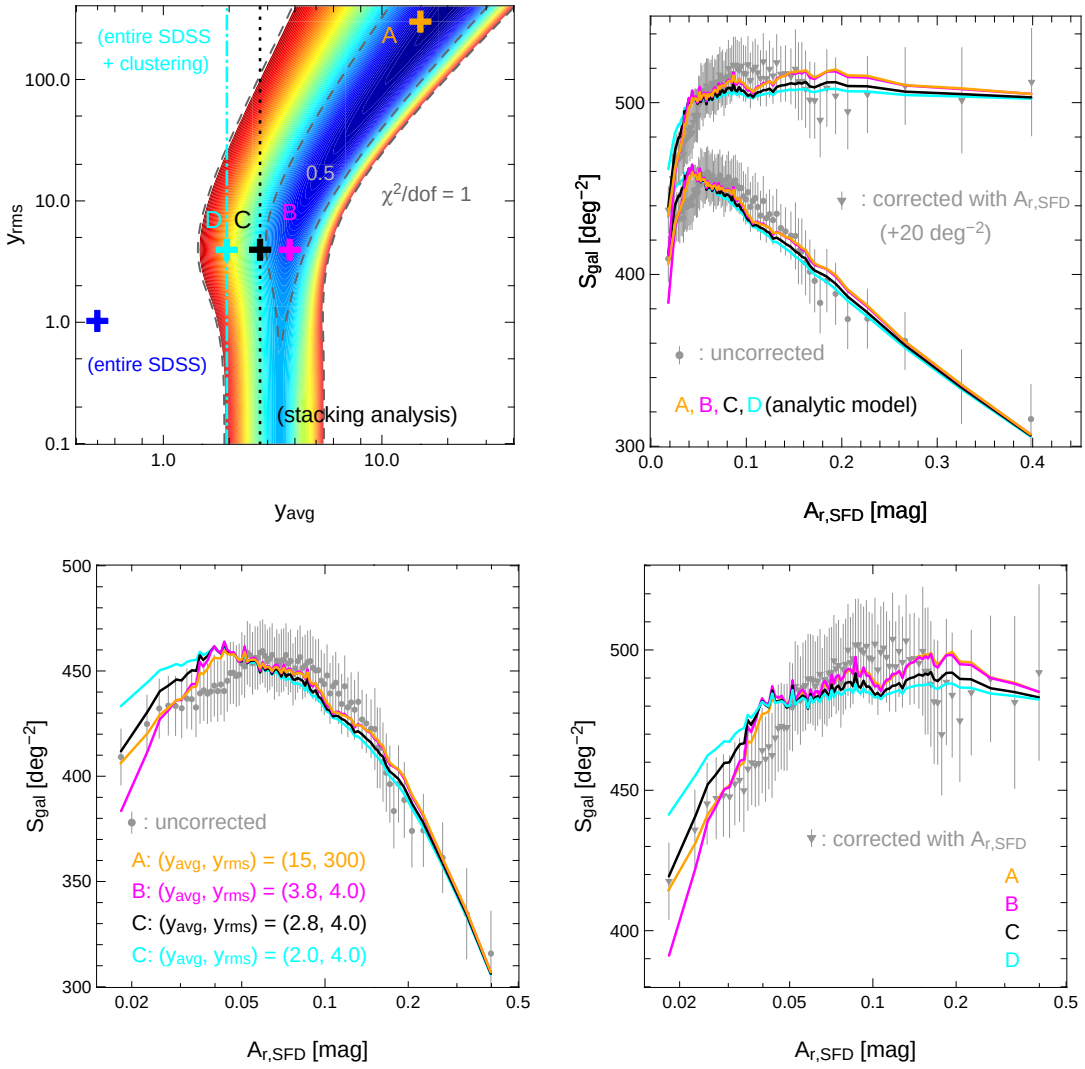

Figure 5.12: Fit to the observed anomaly using the analytical model. *Top left panel*; constraints on $y_{\rm avg}$ and $y_{\rm rms}$ through the chi-squared analysis with equation (5.22). The black dashed curves correspond to $\chi^2/{\rm d.o.f} = 1$ and $\chi^2/{\rm d.o.f} = 0.5$ constraints. The orange (A) and magenta (B) crosses are representative values that best explain the observed anomaly. The black dotted line and cross (C) indicates the value of $y_{\rm avg}$ estimated by stacking analysis (Chapter 4). The blue cross shows the best-fit parameters for single galaxy of entire SDSS sample estimated in §5.3.1. The cyan dot-dashed line and cross (D) also indicates the value of $y_{\rm avg}$ estimated for entire SDSS sample, but including neighbor galaxies contribution (§5.5.3). *Top right panel*; the analytic model predictions plotted over the observational data. The solid lines indicate the analytic prediction by equation (5.18) and (5.19), adopting the values of $(y_{\rm avg}, y_{\rm rms})$ shown as the crosses in *top left*. The symbols are the observational results for the SDSS galaxies in r-band, the same as Figure 5.5. The plots for $S_{\rm gal}$ corrected with $A_{r,{\rm SFD}}$ are shifted by $+20{\rm deg}^{-2}$ just for clarity. *Bottom left*; the same as *top right*, but indicates $S_{\rm gal}$ uncorrected for extinction and the horizontal axis is log-scaled. *Bottom right*; the same as *bottom left*, but for $S_{\rm gal}$ corrected with $A_{r,{\rm SFD}}$.

5.5.2 Comparison with the stacking image analysis

We have shown that the anomaly in the surface number densities of SDSS galaxies on the SFD map is well reproduced by assuming their 100μm to r-band flux ratio is ~ 3.8 on average, where the 100μm flux includes the contribution of neighbor galaxies. On the other hand, the flux ratio of a single galaxy is estimated as ~ 0.5 (see §5.3.1).

Indeed these values should be compared with the result of the stacking image analysis. In the previous Chapter, we found that a galaxy of r-band magnitude m_r contributes to the extinction on average by

$$\Delta A_r^{\rm s}(m_r) = 0.10 \times 10^{0.34(18-m_r)} \ [\rm mmag], \tag{5.23}$$

by itself (single term), and

$$\Delta A_r^{\rm tot}(m_r) = 0.64 \times 10^{0.17(18-m_r)} \ [\rm mmag], \tag{5.24}$$

including the contribution from nearby galaxies (clustering term). The above extinction due to the 100μm emission from galaxies is translated into its 100μm to r-band flux ratio as

$$y = \frac{2\pi\sigma^2}{f_r \nu_r/\nu_{100\mu\rm m}} \frac{\Delta A_r}{k_r p}, \tag{5.25}$$

where σ is the Gaussian PSF width and f_r is the r-band flux. Thus integrated over the differential number density, equations (5.23) and (5.24) suggest that

$$\bar{y}_{\rm avg}^{\rm s} = \frac{\int dm_r \frac{dN}{dm_r} y_{\rm avg}^{\rm s}(m_r)}{\int dm_r \frac{dN}{dm_r}} = 0.239, \tag{5.26}$$

and

$$\bar{y}_{\rm avg}^{\rm tot} = \frac{\int dm_r \frac{dN}{dm_r} y_{\rm avg}^{\rm c}(m_r)}{\int dm_r \frac{dN}{dm_r}} = 2.77, \tag{5.27}$$

respectively.

These values are based on the direct measurement of the FIR contamination, and thus independent of the modeling of 100μm to optical relation. We also emphasis that they should automatically include possible contributions from those galaxies not identified by SDSS. Therefore the sum of the two terms can be reliably interpreted as the expected contribution of the SDSS galaxies to $y_{\rm avg}$ including neighbor galaxies, which is plotted in Figure 5.12. While we do not know the corresponding $y_{\rm rms}$, we have already found that the dependence of the anomaly on $y_{\rm rms}$ is rather weak, at least in our analytic model. Thus the empirical value of $y_{\rm avg}$ from the stacking analysis roughly explains the observed anomaly as plotted in the three panels of Figure 5.12.

We interpret this as a supporting evidence for the FIR model of the SFD anomaly given the fact that we assume a very simple relation between 100μm and optical luminosities, neglecting the galaxy morphology dependence that certainly leads to the FIR flux difference.

5.5.3 Estimates of clustering contribution of SDSS galaxies

We tried to independently estimate $y_{\rm avg}$, including an additional contribution of neighbor galaxies, using the SDSS galaxy distribution over the SFD map, instead of the stacking result discussed in §5.5.2. We first randomly assign the FIR flux of SDSS galaxies assuming $(y_{\rm avg}, y_{\rm rms}) = (0.5, 1.0)$ *for each SDSS galaxy itself neglecting the clustering term.* Second, we sum up the FIR fluxes of galaxies convolved with the PSF of the SFD map (the Gaussian width of $3'.1$) centered at each galaxy. Finally we compute $y_{\rm avg}$ and $y_{\rm rms}$ using the summed FIR fluxes after subtracting the average background flux.

Note that the resulting values of $y_{\rm avg}$ and $y_{\rm rms}$ should be different from the above input values because of the contribution of the clustering term. We find $y_{\rm avg} \approx 2$, but $y_{\rm rms}$ is not well determined because it turned out to be very sensitive to the choice of the background flux. This result indicates that the FIR flux of the SDSS galaxies explains only a half of those required to well reproduce the observed anomaly, $y_{\rm avg} = 3.8$.

Indeed, employing $y_{\rm avg} \approx 2$, our model still reproduces the anomaly qualitatively, but the predicted feature is substantially weaker than that of the observed one. The assigned FIR flux in this model, however, is based on the single galaxy contribution estimated in §5.3.1 ($y_{\rm avg} = 0.5$), thus would be sensitive to the FIR assignment model. Given the fact that the empirical value from the stacking analysis, which is independent of such models, is fairly successful in reproducing the anomaly, we suspect that the factor of two difference originates from the limitation of our crude modeling for FIR flux, instead of the basic flaw of the FIR explanation of the anomaly.

5.6 Discussion

5.6.1 Effects of spatial clustering of galaxies

Both the mock simulations and the analytic model discussed in the previous section completely ignore the spatial clustering of galaxies. We, therefore, examine the clustering effect on the anomaly in this subsection. The most straightforward method is to replace the Poisson distributed particles by dark matter particles from cosmological N-body simulation. For that purpose, we use a realization in the standard ΛCDM cosmology with $\sigma_8 = 0.76$ performed by Nishimichi et al. (2009).

We repeat similar mock observations as in §5.3.2, except that we assign r-band luminosity to each mock galaxy instead of their apparent magnitude. To be more specific, (i) we randomly assign r-band luminosities to all N-body dark matter particles according to the luminosity function of equation (5.7), (ii) convert their luminosities to apparent r-band magnitudes observed from a fixed observer position, and (iii) randomly select a fraction of the particles as mock galaxies so that they match the SDSS observed dN/dm_r (Figure 5.1). The symbols in the top-right panel of Figure 5.13 show the resulting surface number densities of the mock galaxies, adopting $y_{\rm avg} = 3.8$ and $y_{\rm rms} = 4.75$. The mock observation including the galaxy clustering effect shows stronger anomaly than the prediction of the analytic model with the identical $y_{\rm avg}$ and $y_{\rm rms}$ (dashed lines).

We repeat the same fitting analysis as shown in Figure 5.12, except that the data are now replaced by the mock result on the basis of the cosmological N-body simulation. The top-left panel of Figure 5.13 shows the resulting constraints on $y_{\rm avg}$ and $y_{\rm rms}$. As similar to the case for fit to the observational data (Figure 5.12), the values of $y_{\rm avg}$ and $y_{\rm rms}$ are

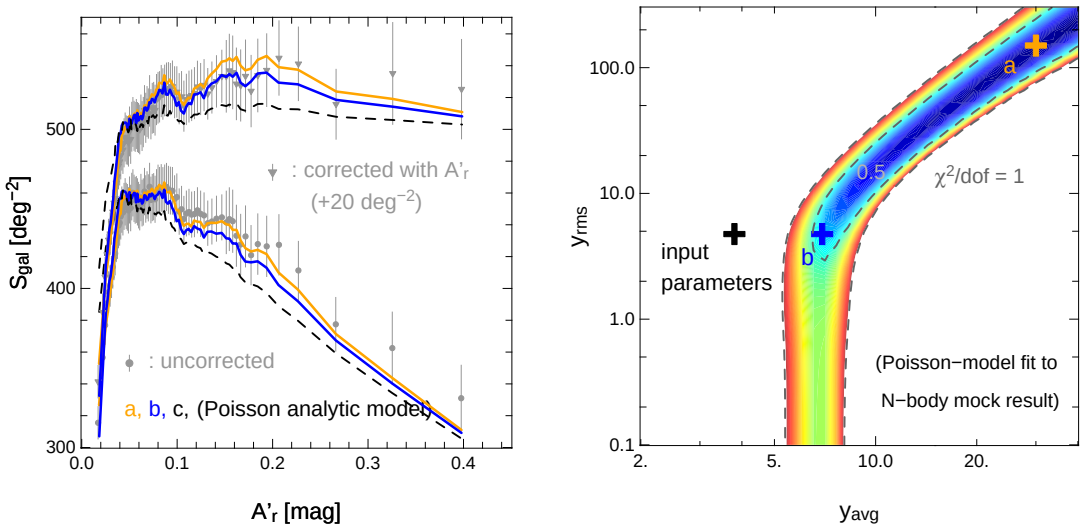

Figure 5.13: Poisson-analytic model fit to the anomaly in the mock simulation result on the basis of the cosmological N-body simulation that takes account of the effect of spatial clustering. *Left panel*; symbols indicate the surface number densities of the mock galaxies with spatial clustering, where we adopt $(y_{\rm avg}, y_{\rm rms}) = (3.8, 4.75)$. *Right panel*; constraints on $y_{\rm avg}$ and $y_{\rm rms}$ from fitting to the anomaly of the mock simulation by the analytic model that neglects the spatial clustering. Gray dashed curves correspond to χ^2/d.o.f $= 1$ and χ^2/d.o.f $= 0.5$ constraints. Black cross indicates the input values of $(y_{\rm avg}, y_{\rm rms}) = (3.8, 4.75)$ adopted in the mock simulation. Orange and blue crosses show the examples of $y_{\rm avg}$ and $y_{\rm rms}$ that well reproduce the mock simulation result, $(y_{\rm avg}, y_{\rm rms}) = (15, 300)$ and $(y_{\rm avg}, y_{\rm rms}) = (6.9, 4.75)$, respectively. The prediction of the analytic model corresponding to each cross is shown as dashed curves in the right panel.

not tightly constrained, and the large values are preferred, *e.g.* $(y_{\rm avg}, y_{\rm rms}) = (30, 150)$ (orange cross). The analytic model that neglects the spatial clustering, however, still reproduces the simulated anomaly very well, if we adopt $y_{\rm avg} \sim 7$ (blue cross), which is larger than the input value by a factor of $\sim$2. This result implies that the effect of galaxy clustering results in the overestimate of the real value of $y_{\rm avg}$, but it can be absorbed effectively by re-interpreting the best-fit values of $y_{\rm avg}$ in the Poisson (without clustering) model appropriately.

In order to quantitatively understand the relation between this bias and the strength of the galaxy spatial clustering, we have to incorporate the effect of spatial clustering in our analytic model. For that purpose, we measure the PDF of the number of the N-body mock particles in a pixel and replace the Poisson distribution in equation (D.2) with the measured one. The analytic model prediction, however, hardly changes by such a modification. Thus more sophisticated improvements seem to be needed to account for the spatial clustering effect, which is beyond the scope of this paper.

5.6.2 Testing the Peek and Graves correction map

In §5.5.2, we found that the observed anomaly of the SDSS galaxies is roughly explained by the contamination of galaxy FIR emission. Nevertheless, the observed and predicted surface number densities (Fig 5.12) do not match perfectly, which might be attributed to other possible systematics in the SFD map.

In order to check the possible systematic effect, we use the improved extinction map by Peek & Graves (2010, hereafter PG). They found that the SFD map *under-predicts* extinction up to ~ 0.1 mag in r-band, using the passively evolving galaxies as standard color indicators. Their method is complementary to our galaxy number count analysis in a sense that they directly measure the reddening by the Galactic dust. Since the resolution of the PG correction map to SFD is $4^\circ.5$, the FIR fluctuations due to the emission of galaxies are not expected to be removed. The PG correction map, however, may have removed other systematics than the FIR contamination, which are not considered in our analytic model at all. Figure 5.14 illustrates the difference between the PG and SFD maps, in which we select the SDSS DR7 survey area alone. Indeed, fairly broad differences are seen around $A_{r,{\rm SFD}} \sim 0.1$ mag.

To see if their correction affects the number count analysis and the anomaly in the original SFD map, we repeat the same analysis described in §6 using the PG map. The results are shown in Figure 5.15. Basically, we find a very similar correlation between $S_{\rm gal}$ and $A_{r,{\rm PG}}$, suggesting that the PG map still suffers from the FIR contamination of galaxies as expected. The resulting constraints on $y_{\rm avg}$ and $y_{\rm rms}$ is also similar to the case of the SFD map. We note, however, that our analytic model prediction exhibits slightly better agreement for the PG map than for the SFD map, This may indicates that possible systematic errors in the SFD map other than the FIR contamination are removed, at least partially, in the PG map.

5.6.3 Effects of the FIR contamination on cosmological analysis

The systematic errors in the SFD map due to the FIR contamination, which turned out to be of the order of $0.1 - 1$ mmag, would not significantly affect the observations of individual objects. The FIR contamination is, however, directly correlated with the large

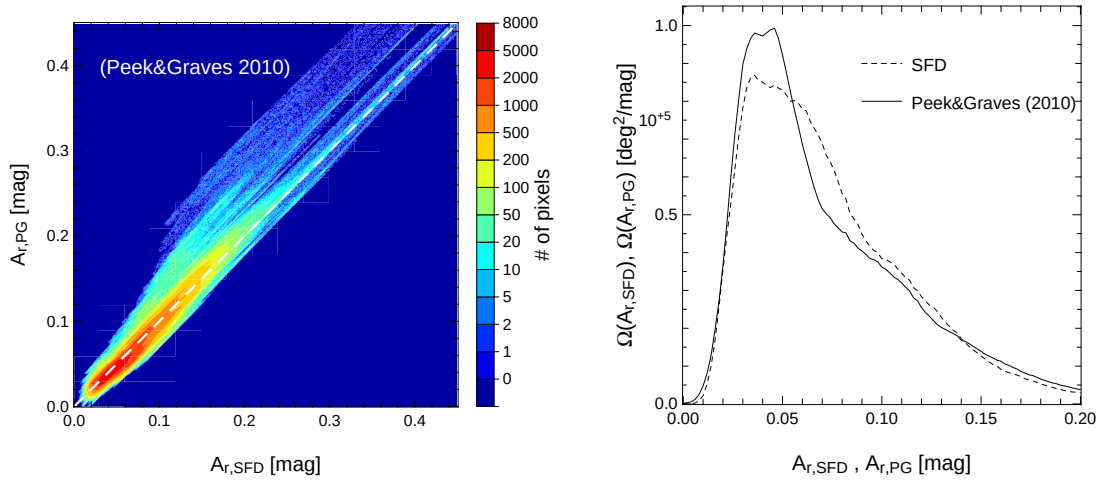

Figure 5.14: *Left panel*; Comparison of the SFD map with the corrected extinction map provided by Peek & Graves (2010). The numbers of pixels in the SDSS survey region are evaluated for intervals of 1 mmag for both $A_{r,\mathrm{SFD}}$ and $A_{r,\mathrm{PG}}$. *Right panel*; The distribution of sky area as a function of $A_{r,\mathrm{SFD}}$ (dashed line) and $A_{r,\mathrm{PG}}$ (solid line).

scale structure of the universe, these errors are potentially important for the cosmological studies using galaxy surveys.

One possible effect is an apparent enhancement of the spatial clustering of galaxies. Given that the SFD map is contaminated by the FIR emission of galaxies, dust extinction is overestimated in the regions where the surface number densities of the galaxies are large, *i.e.*, strong clustering regions. Therefore, the magnitudes of the galaxies in over-dense regions are overcorrected for dust extinction, and then the observed surface number densities are even more enhanced. Thus the signal of galaxy clustering, which is an important prove for cosmology, is expected to be systematically enhanced. The enhancement of the surface number densities expected from the FIR contamination of ~ 1 mmag would be small, of the order of 0.1%, therefore it may be not crucial for the most purposes. It would affect, however, the measurement of the galaxy clustering in a complicated fashion, potential systematics due to the FIR contamination should be carefully investigated.

For instance, Fang et al. (2011) investigated the effect of the extinction due to the dust associated with galaxies. The surface densities of galaxies in over-dense regions are suppressed by dust extinction associated with neighbor galaxies. As a result of this effect, they found that dust extinction of the order of 1 mmag distorts the correlation function of galaxies in redshift space, and potentially biases the measurement of the redshift distortion parameter, by up to $\sim 5\%$, which is non-negligible compared to the accuracy of current measurements. Interestingly, the expected effect of the dust extinction on the clustering of galaxies is quantitatively opposite to that of the FIR contamination, therefore the FIR contamination could also significantly affect the cosmological tests of the general relativity using the redshift distortion of galaxy clustering, which is one of the aims of the upcoming galaxy surveys, e.g., Euclid, LSST (Large Synoptic Survey Telescope), etc.

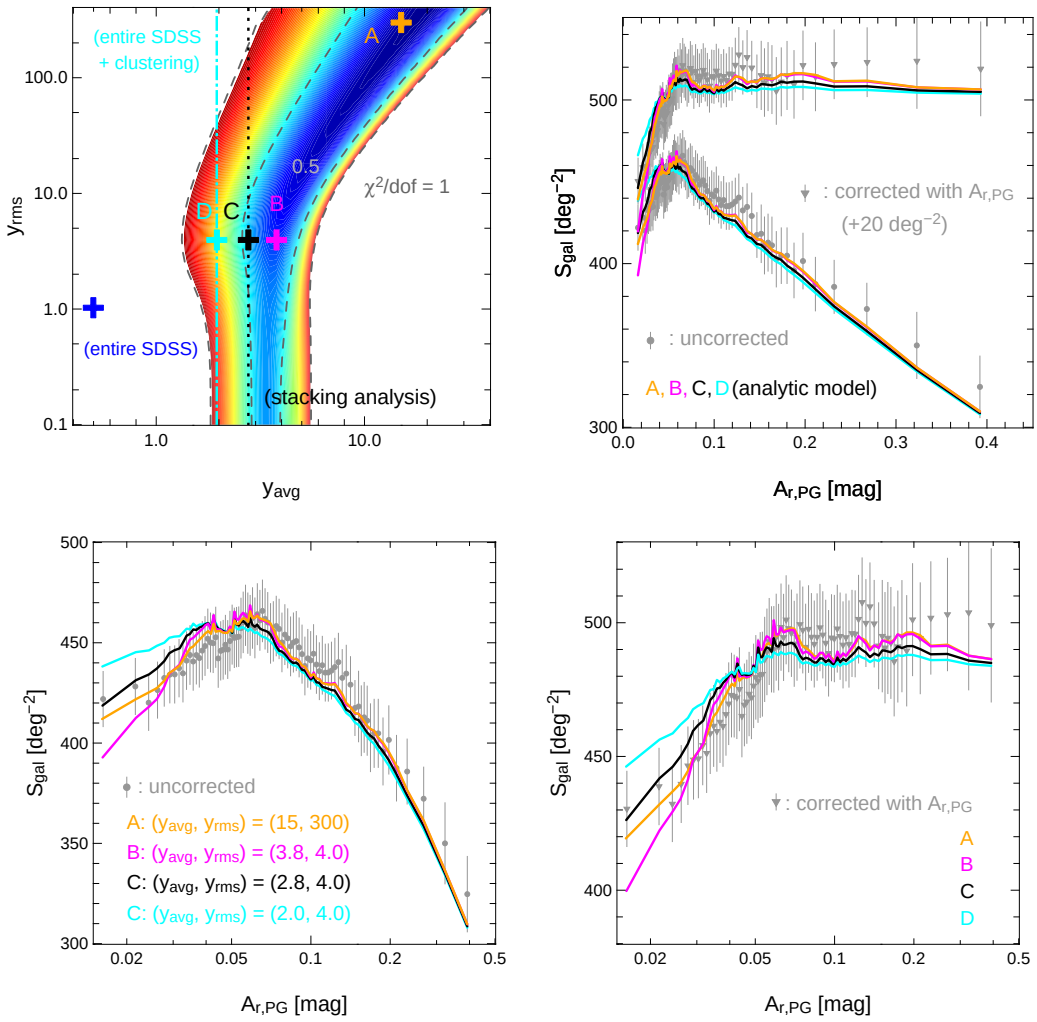

Figure 5.15: Fit to the observed anomaly using the analytical model, as the same as Figure 5.12, but for the corrected extinction map provided by Peek & Graves (2010), $A_{r,\mathrm{PG}}$. The reference values of y_{avg} and y_{rms} indicated as crosses are the same as Figure 5.12.

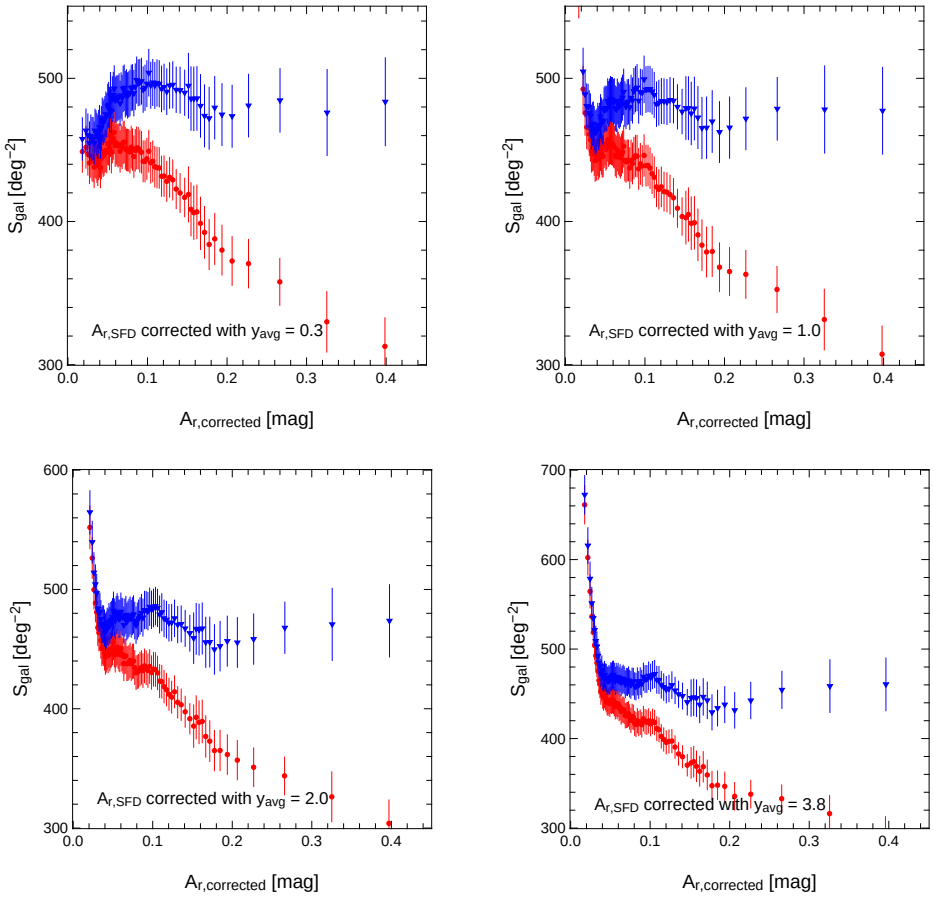

Figure 5.16: Surface number densities of the SDSS galaxies with $17.5 < m_{\rm r} < 19.4$ after subtracting their average FIR emission contamination, where $y_{\rm avg} = 0.3, 1.0, 2.0, 3.8$ are adopted for estimation of the FIR emission of the SDSS galaxies.

5.7 Limitation of the correction for the FIR emission of galaxies

We attempt to correct the SFD map by subtracting the average FIR contamination of SDSS galaxies. The corrected extinction at an angular position θ in the Galactic map is computed as

$$A_{r,\rm corrected}(\theta) = A_{r,\rm SFD}(\theta) - \sum_j \Delta A(\theta_j - \theta; m_r^j), \tag{5.28}$$

where θ_j is the position of the j-th galaxy with its r-band magnitude of m_r^j. We employ 4 different values for ΔA given the uncertainty of the interpretation of the best-fit value of $y_{\rm avg}$ discussed before. As shown in Figure 5.16, however, the above correction does not seem to remove the anomaly so well. This is possibly because we neglect the variance of the relation between optical-FIR fluxes, and corrected the SFD map assuming the deterministic relation using $y_{\rm avg}$.

For comparison, we apply the same method of correcting the FIR contamination to the mock Poisson simulations in subsection 5.3.2. We repeat the similar mock Poisson simulation to §5.3, but the contaminated mock extinction map, A'_r, is corrected by sub-

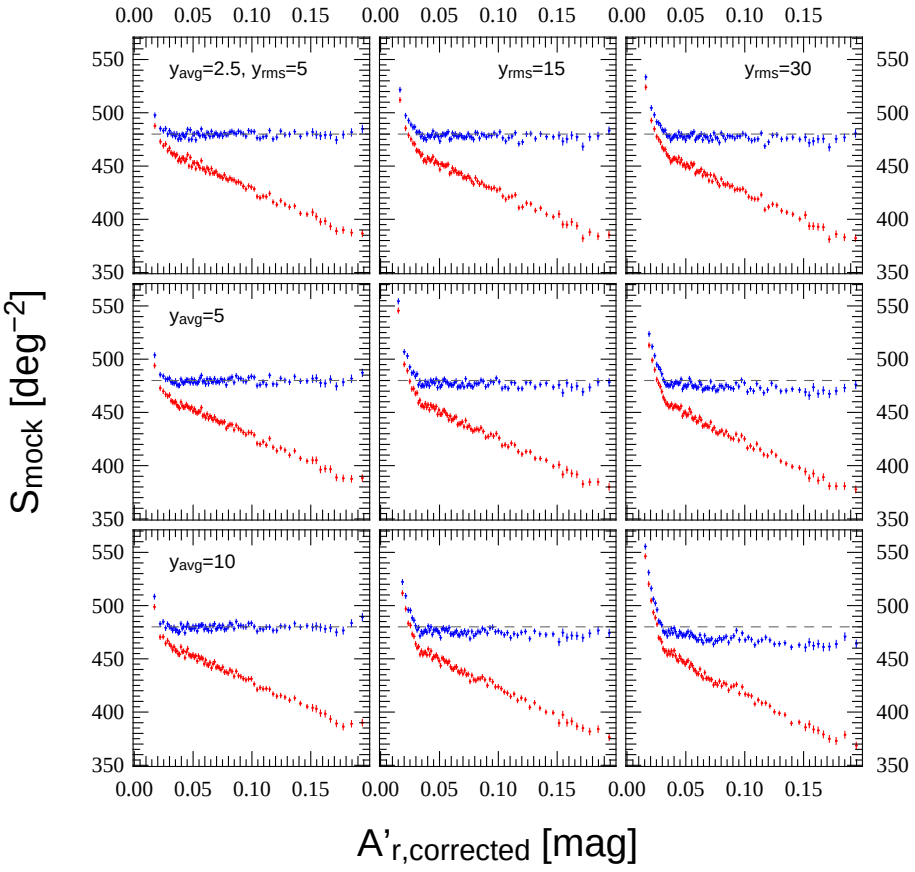

Figure 5.17: The surface number density of the Poisson mock simulation, subtracting the FIR contamination by the deterministic correction adopting the input value of $y_{\rm avg}$ alone. For $y_{\rm avg}$ and $y_{\rm rms}$, the same parameters as Figure 5.11 are adopted.

tracting the FIR flux of the mock galaxies. As we did for the SFD map above, here we adopt only the input value of $y_{\rm avg}$, and neglect its variance, thus assume $y_{\rm rms} = 0$.

Figure 5.17 shows the surface number density of the mock galaxies as a function of the average-corrected extinction, $A'_{r,\rm corrected}$. The anomaly is reasonably removed for the smallest value of $y_{\rm rms} = 5$, *i.e.,* the surface number density after extinction correction is independent of $A'_{r,\rm corrected}$. For the larger values of $y_{\rm rms} = 15$ and 30, however, the surface number densities are clearly overcorrected and decrease against $A'_{r,\rm corrected}$ where $A'_{r,\rm corrected} < 0.04$ mag, as qualitatively similar to what we found for the SFD map. These results indicate that the deterministic correction for the FIR contamination neglecting the variance of the FIR fluxes does not appropriately resolve the anomaly, even in the case that all the systematic errors are due to the FIR contamination and the exact value of $y_{\rm avg}$ is adopted for subtracting the FIR fluxes.

The possible reason of the negative correlation is that the our correction method overcorrects the FIR contamination in the low extinction region. In order to confirm that, we calculate the average values of y as a function of A'_r in the Poisson mock simulations. We again divide the entire sky area into subregions according to the contaminated extinction, A'_r, and then separately compute the average value of $y(A'_r)$ for the mock galaxies in each A'_r bin. Figure 5.18 shows the fractional difference between $y(A'_r)$ and the assumed value

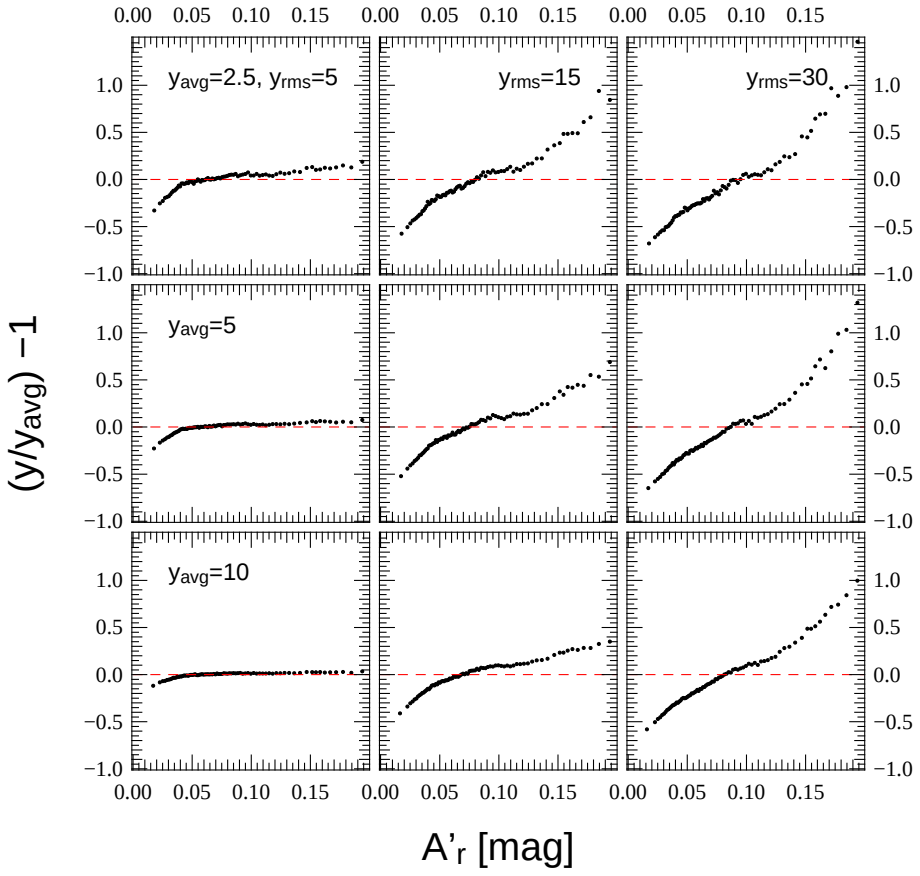

Figure 5.18: Fractional difference between y and the input value of $y_{\rm avg}$ as a function of A'_r in the Poisson mock simulation. For $y_{\rm avg}$ and $y_{\rm rms}$, the same parameters as Figure 5.11 are adopted.

of $y_{\rm avg}$. The result indicates that $y(A'_r)$ is systematically smaller than that for entire mock galaxies where $A'_r < 0.1$ in the cases for large $y_{\rm rms}$, thus the FIR contamination is indeed overcorrected if we adopt $y_{\rm avg}$ for those galaxies in the corresponding regions.

The relation between the FIR and optical flux for SDSS galaxies probably have a large variance due to its dependence on the morphology, luminosity, and redshift, although the value $y_{\rm rms}$ for SDSS galaxies is hardly constrained by the fitting analysis to the observed anomaly presented in subsection 5.5.1. This would be, at least a part of, the reason why our correction to the SFD map does not well work and exhibits the negative correlation similar to the cases for the Poisson mock simulations. The scatter of the FIR to optical relation is possibly reduced if it is individually estimated for each class of galaxies, divided according to their properties. We examine the feasibility to measure the dependence of the FIR emission on the morphology of galaxies using the stacking analysis below.

5.7.1 Dependence of the FIR to optical relation on galaxy colors

In order to investigate the morphology dependence of the FIR to optical relation, we perform the stacking analysis for the subsamples of galaxies divided by their morphologies. It is known that the color and morphology of galaxies are closely related, and the bimodal distributions of galaxies on color-color or color-magnitude diagram are useful to divide galaxies into red-early and blue-late type (e.g., Strateva et al., 2001; Blanton et al., 2005a; Zehavi et al., 2011). Strateva et al. (2001) indicated that SDSS galaxies are roughly divided into the two populations by $u - r = 2.22$, thus we use $u - r$ color of galaxies as the indicator of galaxy morphologies,

Figure 5.19 shows the differential number count as a function of $u - r$ for our sample, which is divided into five m_r bins with $\Delta m_r = 1.0$. We further divide each subsample of m_r into five subsamples according to $u - r$ as $-0.8 < u - r < 1.7$, $1.7 < u - r < 2.2$, $2.2 < u - r < 2.7$, $2.7 < u - r < 3.2$, and $3.2 < u - r < 6.7$. Then we repeat the stacking analysis for each 5 (m_r bin) $\times$ 5 ($u-r$ bin) = 25 subsamples, and decompose the detected signal into the single term, clustering term, and the constant offset term as in Chapter 4.

Figure 5.20 indicates the best-fit values of $\Sigma_{\rm g}^{\rm s0}$, $\Sigma_{\rm g}^{\rm c0}$, and $\Sigma_{\rm g}^{\rm s0} + \Sigma_{\rm g}^{\rm c0}$. The values of single term, $\Sigma_{\rm g}^{\rm s0}$, for the bluest two subsample are consistent each other, and decrease for redder galaxies. We also note that $\Sigma_{\rm g}^{\rm s0}$ for $u - r < 2.7$ scale as proportional to $10^{-0.4m_r}$, which indicates the FIR to optical flux ratio is constant. For the reddest subsample, $3.2 < u - r < 6.7$, the best-fit values are zero, therefore not shown in this plot. The systematic trend of $\Sigma_{\rm g}^{\rm s0}$ decreasing for redder galaxies is reasonable, since the morphology of galaxies is correlated with their star formation activity and thus the interstellar dust in the blue star-forming galaxies is more effectively heated by the ISRF, compared to the red quiescent ones. On the other hand, the values of single term, $\Sigma_{\rm g}^{\rm c0}$ does not significantly vary with the galaxy color, although the slight increasing trend for redder galaxies may be marginally recognizable, which could be attributed to the morphology-density relation of galaxies.

We attempt to correct the SFD map taking account for the color dependence of the FIR contamination due to SDSS galaxies. The best-fit values of $\Sigma_{\rm g}^{\rm s0}(m_r, u-r)$ is approximated as

$$\Sigma_{\rm g}^{s0}(m_r, u-r) = B_{u-r} \times 10^{\alpha_{u-r}(18-m_r)}, \tag{5.29}$$

where the best-fit values of B_{u-r} and α_{u-r} are computed for each $u - r$ subsamples. For

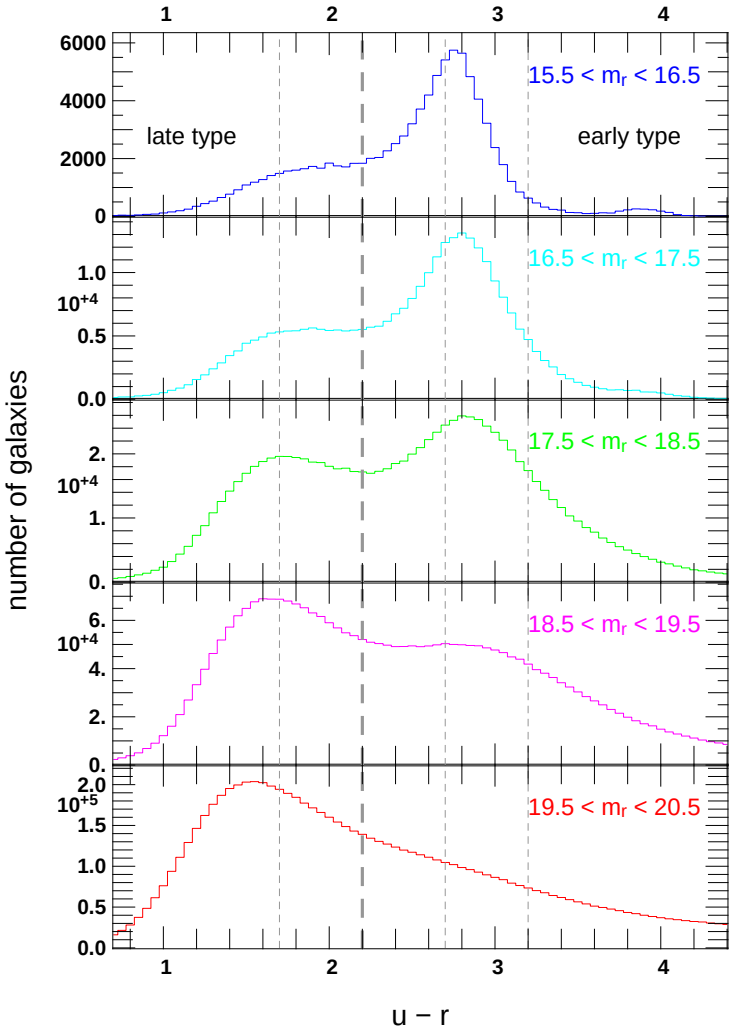

Figure 5.19: The differential number count of SDSS galaxies as a function of $u - r$. From top to bottom, each panel shows the number of galaxies with $20.5 < m_r < 19.5$, $19.5 < m_r < 18.5$, $18.5 < m_r < 17.5$, $17.5 < m_r < 16.5$, and $16.5 < m_r < 15.5$. The vertical dashed lines indicate the boundaries of our subsample used in the stacking analysis. The vertical solid line shows the color separator proposed by Strateva et al. (2001) so that the SDSS galaxies are divided into red early and blue late type.

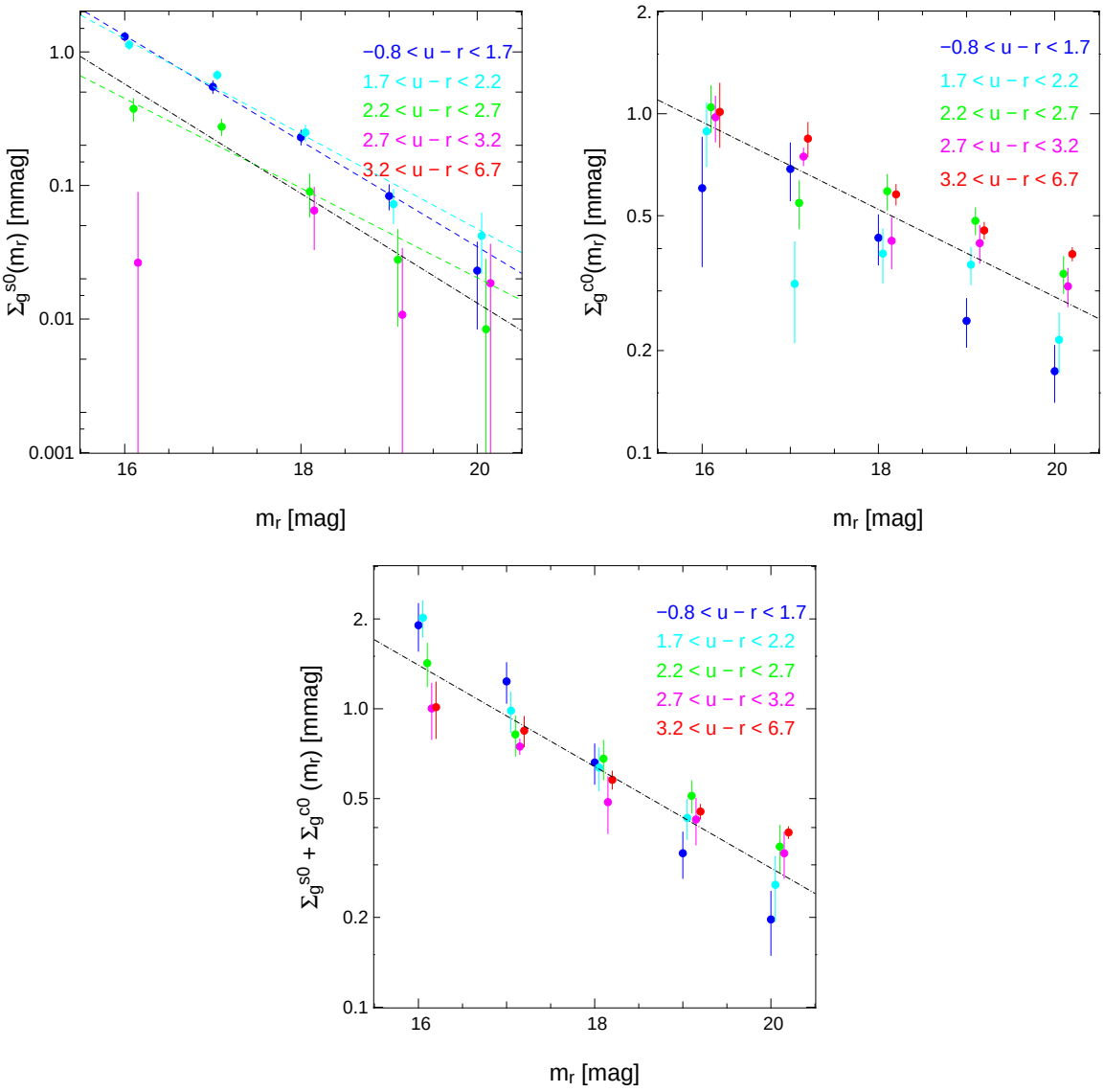

Figure 5.20: The best-fit values of Σ_g^{s0} (*top left*), Σ_g^{c0} (*top right*), and $\Sigma_g^{s0} + \Sigma_g^{c0}$ (*bottom*) for m_r and $u - r$ binned 25 subsamples. Blue, cyan, green, magenta, and red symbols indicate the best-fit values for $-0.8 < u - r < 1.7$, $1.7 < u - r < 2.2$, $2.2 < u - r < 2.7$, $2.7 < u - r < 3.2$, and $3.2 < u - r < 6.7$, respectively. The error bars are computed from 400 jackknife resampling. Dashed lines in the top left panel indicate the best-fit power law of equation (5.29), for $-0.8 < u - r < 1.7$, $1.7 < u - r < 2.2$, and $2.2 < u - r < 2.7$. Dot-dashed (black) lines in each panel indicate the best-fit power law for the entire sample, neglecting the color dependence shown Figure 4.11. The best-fit values of Σ_g^{s0} for $3.2 < u - r < 6.7$ are zero for all m_r bin, therefore not shown here.

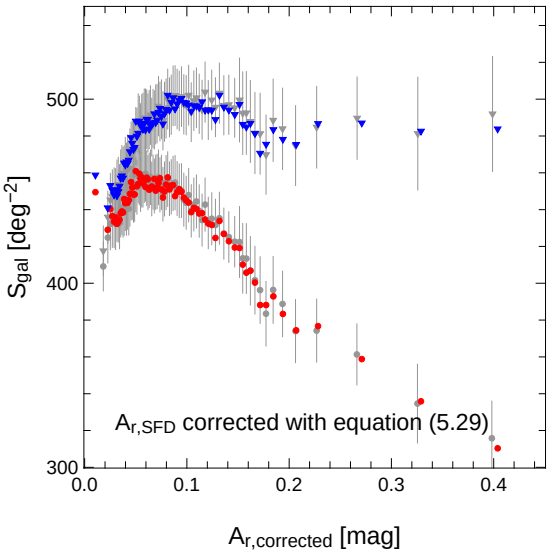

Figure 5.21: Surface number densities of the SDSS galaxies with $17.5 < m_{\rm r} < 19.4$ after subtracting their FIR emission contamination from the SFD map, taking account for its dependence on their colors, following equation (5.29) (red circles, blue triangles). Gray symbols with the error bars indicate the surface number densities without any correction for the FIR contamination, the same as Figure 5.5.

$2.7 < u - r < 3.2$ and $3.2 < u - r < 6.7$ color-bins, we set $\Sigma_{\rm g}^{s0}(m_r, u - r)$ as zero. We compute the FIR fluxes of SDSS galaxies following equation (5.29), and individually subtract those contribution from the SFD map. The anomaly of the SFD map is still not well removed as shown in Figure 5.21. The possible reasons include (1). the FIR to optical flux relation of SDSS galaxies is much more complicated than considered here, (2). optical faint galaxies that are not identified by SDSS significantly contribute to the FIR contamination. Those contribution cannot be corrected for in our current method, and (3). unknown systematic errors other than the FIR contamination are also responsible for the anomaly. In principle, the first possibility can be directly examined by repeating the stacking analysis according to the properties of galaxies other than their colors, while it would be difficult in practical, since the statistical significance of the stacked signal and the reliability of profile decomposition are limited by the resolution of IRAS. The current high resolution data by AKARI satellite will be very promising for this direction.

5.7.2 Future prospects for the all-sky images by AKARI

The AKARI satellite (Murakami et al., 2007) performed the all-sky imaging survey in FIR, covering the wide range of wavelengths, 9μm to 160μm. The angular resolution of the AKARI all-sky image is 10″ FWHM for 9, 18μm (IRC: InfraRed Camera) and FWHM 1′ for 65 to 160μm (FIS: Far-Infrared Surveyor), which are much better than the FIR all-sky data by IRAS that we have used throughout this thesis. Taking advantages of multi-wavelength and high resolution imaging data, the upcoming dust map using AKARI data will achieve significant improvements in the removal of zodiacal light and the accuracy of the color temperature correction, which is limited by the poor resolution of DIRBE in the SFD map construction (Ootsubo et al. 2014).

On the other hand, the detection limits of point sources at 90μm is ~ 0.5Jy, whereas the amount of the FIR contamination in the SFD map, $\Delta A_{r,\mathrm{SFD}} \sim 1$ mmag, corresponds to 0.1Jy. Therefore it would be not sufficient only to subtract the AKARI point sources, at least, in order to remove all the FIR contamination associated with SDSS galaxies. Nevertheless, the high angular resolution of the AKARI data will enable us to detect the FIR emission of galaxies with much higher statistical significance, and improve the reliability of the interpretation of the detected signal, including the decomposition into single and clustering term. Therefore the extensive studies of the FIR emission of SDSS galaxies will become possible, which will be helpful for constructing the new dust map free from the systematic due to extragalactic light contaminations based on the AKARI data.

5.8 Summary

In this chapter, we have revisited the origin of the anomaly of surface number density of SDSS galaxies with respect to the Galactic extinction, originally pointed out by Yahata et al. (2007). We first computed the anomaly using the SDSS DR7 photometric catalogs, and then developed both numerical and analytic models to explain the anomaly. We take account of the contamination of galaxies in the IRAS 100μm flux that was assumed to come entirely from the Galactic dust.

Our main findings are summarized as follows.

- Both numerical simulations and analytic model reproduce the observed anomaly quite well. Thus we quantitatively confirmed the validity of the hypothesis that the observed anomaly in the SFD Galactic extinction map is mainly due to the FIR emission from galaxies, originally proposed by Yahata et al. (2007).

- The comparison of the analytic model and the observed anomaly constrains mainly the average 100μm to optical flux ratio for SDSS galaxies. The resulting value is in a reasonable agreement with that obtained from the stacking image analysis of the SDSS galaxies (Chapter 5).

- We also independently estimated the FIR contribution of single SDSS galaxy based on IRAS/SDSS overlapped catalogue data assuming a simple relation between FIR and optical luminosities. Summing up such FIR flux according to the SDSS galaxy distribution, however, we find that those contribution only explains roughly half of that required to reproduce the observed anomaly. This result may be due to the limitation of our modeling of the FIR to optical relation.

While our current analytic model still needs to be improved, the fact that the empirically determined value of y_{avg} nicely reproduces the observed anomaly indicates that the FIR emission of SDSS galaxies is the major origin of the anomaly.

In particular, we note that subtracting the average FIR contamination of the SDSS galaxies from the SFD extinction map does not properly remove the observed anomaly. This may imply that it is essential to consider the dependence of FIR emission on galaxy morphology and/or the effect of galaxy clustering, both of which we have neglected in the current analytical model. Such morphology dependence of FIR luminosities of SDSS galaxies needs to be extensively investigated by stacking analysis, fully exploiting the

multi-band photometries of SDSS DR7, and using the recent high resolution and multi-wavelength data of AKARI, WISE, etc.

The FIR contamination that explains the anomalous behavior in the surface number density of the SDSS galaxies is just statistical and tiny, on the order of (0.1∼1) mmag of extinction in r-band, which is much less serious than naively expected from the anomaly. Nevertheless the galaxy FIR emission is correlated with the large scale structure of the universe. Thus it may systematically bias the cosmological analysis. The present methodology is in principle applicable to check the reliability, and even to improve the accuracy of the future Galactic extinction map that should play a key role in all astronomical observations, in particular for the purpose of precision cosmology.

Chapter 6

Implication of stacking analysis for spatial extent and temperature of dust around galaxies

In this Chapter, we present an application of the stacking analysis presented in Chapter 4. We propose the method to constrain the spatial extent of dust around galaxies through the measurement of dust temperature from FIR stacking image analysis, which would provide a information to diagnose the spatial extent of dust around galaxies, which has been implicitly assumed to be confined in galactic disks so far.

6.1 Suggestion of extended dust around galaxies from SDSS angular correlation analysis

Dust plays important roles in cosmic star formation and evolution of the galaxies. The basic ingredients of dust grains are metals produced through past stellar activity, and thus the main reservoir of dust is conventionally thought to be mainly confined in interstellar space within galaxies. Zwicky (1962), however, suggested the existence of dust filling the intracluster space within the Coma cluster, which motivated the investigation of the abundance and spatial distribution of dust in different environments, including the color-excess of background objects due to dust optical-UV reddening (Zaritsky, 1994; Chelouche et al., 2007; McGee & Balogh, 2010; Muller et al., 2008), and the FIR dust emission from individual objects (Stickel et al., 1998, 2002; Kaneda et al., 2009; Kitayama et al., 2009), and from stacking analysis (Montier & Giard, 2005; Gutierrez & Lopez-Corredoira, 2014).

Recently, Ménard et al. (2010a: hereafter MSFR) investigated the distribution of dust around galaxies by measuring the angular correlation between the spatial distribution of SDSS photometric galaxy ($z \sim 0.35$) and the colors of distant SDSS quasars ($1 < z < 2$). Their result is shown in Figure 6.1. They found that mean g-i reddening profile around the SDSS galaxies is well approximated by a single power-law:

$$\langle E_{g-i} \rangle(\theta) = (1.5 \pm 0.4) \times 10^{-3} \left(\frac{\theta}{1'.0} \right)^{-0.86 \pm 0.19}, \tag{6.1}$$

where θ is the angular separation between foreground galaxies and background quasars. Furthermore they discovered that the above power-law extends even for $\theta > 10'$. The

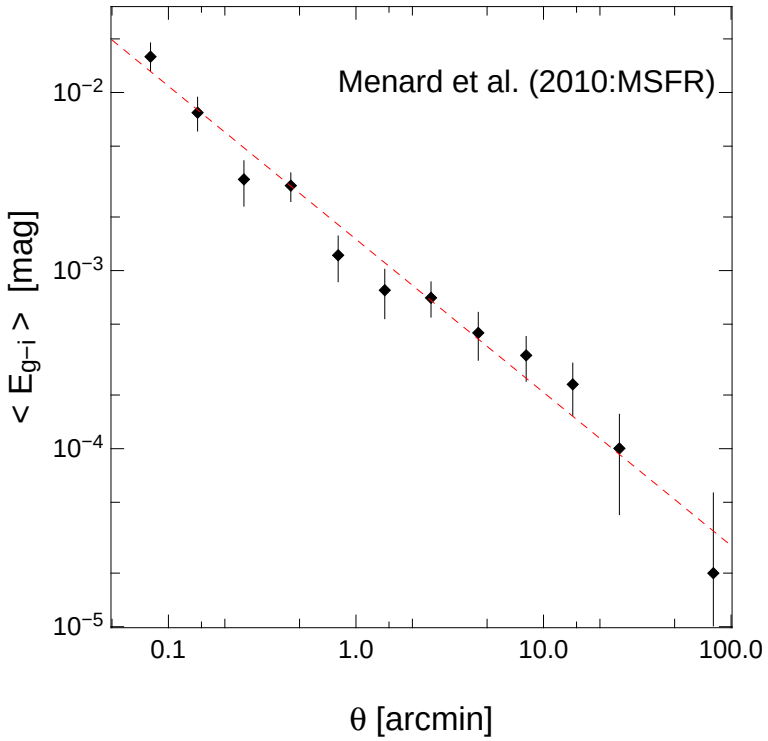

Figure 6.1: Radial profile of dust reddening around SDSS galaxies with $17 < m_i < 21$ (Ménard et al., 2010a). The dashed line indicates the best power-law fit of equation (6.1).

angular scale corresponds to several Mpc at the mean redshift $\langle z \rangle = 0.36$ of their SDSS galaxy sample. This is far beyond the typical scale of galactic disks, and even larger than the virial radius of typical galaxy clusters.

MSFR appear to interpret their result as an evidence for a dust component surrounding an individual galaxy beyond a few Mpc, which we refer to as *the extended dust model*. The interpretation, however, is rather subtle. The mean reddening profile from their measurement $\propto \theta^{-0.8}$ is close to that of the angular correlation function of galaxies. This raises a possibility that the detected dust reddening may be equally explained by the summation of the dust component associated with the central part of galaxies according to the spatial clustering of those galaxies, which will be referred to as *the clustered dust model*.

In practice, it is rather difficult to distinguish between the extended and clustering dust models on the basis of the statistical correlation analysis as performed by MSFR. Therefore a complementary and independent methodology to constrain the nature of the dust is needed. This is exactly what we attempt to propose in this Chapter.

For that purpose, we measure the dust far-infrared (FIR) emission of the SDSS galaxies by stacking analysis. We return to the 100μm intensity map by SFD, rather than the extinction map, and perform the stacking analysis of the same sample as the MSFR. If the detected FIR emission originates from the same dust component as the MSFR reddening measurement, the emission to absorption ratio gives a constraint on dust temperature, which would offer complementary information to distinguish between the extended and clustered dust models mentioned above.

In the following analysis, we assume the standard ΛCDM cosmology with $\Omega_{\rm m} = 0.3$,

$\Omega_\Lambda = 0.7$, and $h = 0.7$.

6.2 Data

We select our galaxy sample adopting the same sky are selection and photometry flag selection as the previous chapters. Then we impose the same magnitude cut, $17 < m_i < 21$, as the MSFR sample for a direct comparison with their results, where the magnitudes of the galaxies are corrected for Galactic extinction using the SFD map. Our final sample collects 2.88×10^7 galaxies.

For far-infrared data, we use the all-sky diffuse 100μm map provided by SFD, which is denoted as $I_{\rm corr}$ in equation (3.10). Hereafter, we adopt a Gaussian with $\sigma = 3'.1$ for the point spread function (PSF) of SFD/IRAS map, as measured by similar stacking analysis in Chapter 4.

6.3 Stacking image analysis of FIR emission from SDSS galaxies

6.3.1 Stacked radial profiles

Following the procedures in Chapter 4, we stack the SFD/IRAS 100μm map over $40' \times 40'$ squares centered on each SDSS galaxy. Each image is randomly rotated around the center. The resulting stacked image shows clear circular signature of dust emission associated with those galaxies.

The radial profile of the stacked image is shown in Figure 6.2, where the error bars reflect the *rms* in each radial bin ($\Delta\theta = 0.5'$). The radial profile is Gaussian-like around the central region, but exhibits an extended tail beyond the PSF width, $\sigma = 3'.1$, which corresponds to roughly 1Mpc for the mean redshift $\langle z \rangle \sim 0.36$ of the SDSS galaxies.

We suspect that our measurement is equivalent to the large-scale correlated of dust reddening detected by MSFR. We interpret the detected signal in terms of the clustered dust model, and adopt the radial profile:

$$I_{\rm tot}(\theta) = I_{\rm s}(\theta) + I_{\rm c}(\theta) + C, \tag{6.2}$$

where $I_{\rm s}$ and $I_{\rm c}$ represent the contributions from the central single galaxy (single term) and from the clustered neighbor galaxies (clustering term), respectively [1], and C is the background level of the foreground Galactic dust emission. The Galactic foreground, C, should be uncorrelated with the SDSS galaxies, and thus is assumed to be constant. Since the PSF of SFD/IRAS map is well approximated by Gaussian, $I_{\rm s}(\theta)$ is written as

$$I_{\rm s}(\theta) = I_{\rm s0} \exp\left(-\frac{\theta^2}{2\sigma^2}\right), \tag{6.3}$$

where $\sigma = 3'.1$ is the Gaussian width of PSF.

[1] These definitions of $I_{\rm tot}$, $I_{\rm s}$, and $I_{\rm c}$ are equivalent to $\Sigma_{\rm g}^{\rm tot}$, $\Sigma_{\rm g}^{\rm s}$, and $\Sigma_{\rm g}^{\rm c}$ used in Chapter 4, respectively, except that $\Sigma_{\rm g}$ denotes the SFD map extinction in units of [mag], whereas I in this paper denotes the intensity in units of [MJr/sr].

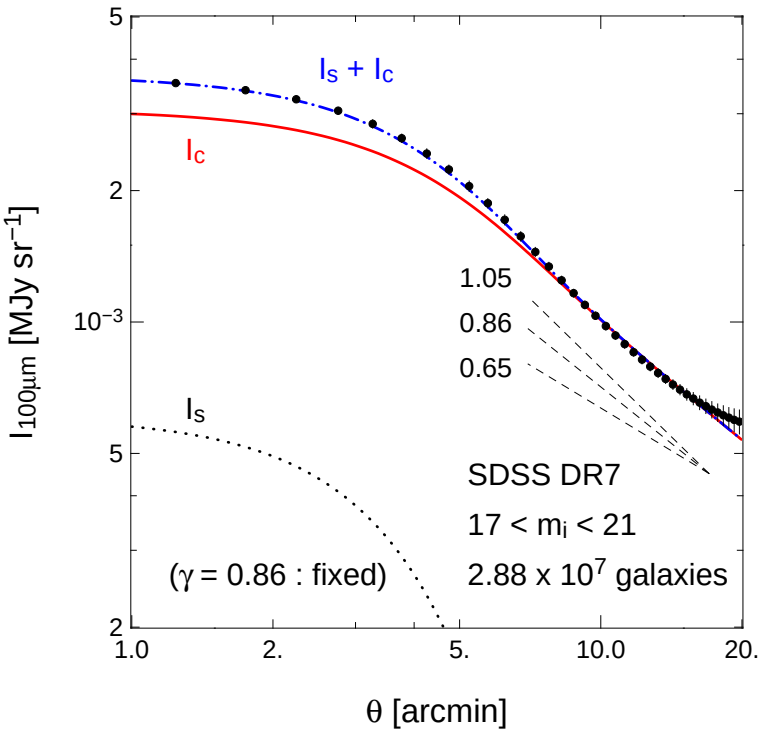

Figure 6.2: Radial profile of the FIR stacked image of SDSS galaxies. The symbols indicate the radial average of the stacked image and the error bars show rms in each radial bin. The offset level due to the Galactic dust is computed assuming $\gamma = 0.86$, and the resulting value of $C = 1.4$[MJy sr^{-1}] is subtracted from the stacked data. The lines indicate the best-fits for $I_{\rm s}$ (black dotted), $I_{\rm c}$ (red solid), and $I_{\rm tot} - C$ (blue dot-dashed); see equation (6.2). Just for reference, we plot the power-laws of $\gamma = 0.65$, 0.86 and 1.05 in dashed lines, which covers the ranges of the MSFR result in equation (6.1).

The clustering term $I_{\rm c}$ is written in terms of $I_{\rm s}$ and angular two-point correlation function (2PCF) of galaxy, $w(\theta)$, as

$$I_{\rm c}(\theta) = \int dm' \frac{dN(m')}{dm} \int d\varphi I_{\rm s}(\theta - \varphi; m') w(\varphi; m'), \tag{6.4}$$

where $dN(m')/dm'$ is the differential number count of galaxies (whether or not detected by SDSS) as a function of m'. We assume that the single term is written as the function of m_i, therefore the dependences on other physical quantities are neglected. We assume the angular 2PCF is described as a single power-law in this angular scale (Connolly et al., 2002; Scranton et al., 2002);

$$w(\theta; m') = A(m') \left(\frac{\theta}{\theta_0} \right)^{-\gamma}, \tag{6.5}$$

where the amplitude A is a function of m_i, but the index γ is assumed to be independent of m_i. In this case, equation (6.4) reduces to

$$I_{\rm c}(\theta) = I_{\rm c0} \exp\left(-\frac{\theta^2}{2\sigma^2} \right) \ {}_1F_1 \left(1 - \frac{\gamma}{2}; 1; \frac{\theta^2}{2\sigma^2} \right), \tag{6.6}$$

where

$$I_{\rm c0} = 2\pi\sigma^2 \left(\frac{\varphi_0}{\sqrt{2}\sigma} \right)^{\gamma} \Gamma\left(1 - \frac{\gamma}{2} \right) \int dm' I_{\rm s0}(m') A(m') \frac{dN(m')}{dm'}. \tag{6.7}$$

We fit the radial profile of the stacked image using equations (6.2), (6.3), and (6.6). In doing so, we do not use equation (6.7), but treat $I_{\rm c0}$ simply as one of the fitting parameters empirically determined from the observed profile. We estimate the statistical errors using the jackknife resampling method by dividing the entire SDSS sky area into 400 patches of equal area.

The detected emission profile at small θ is affected due to the IRAS PSF, and should not be directly compared with the MSFR measurement. Therefore, we use the clustering term, which is relevant for $\theta \gg \sigma$, for the dust temperature constraint in the following Section. In fact, the PSF effect on the clustering term vanishes at large θ and equation (6.6) reduces to the power-law as

$$I_c(\theta) = \frac{I_{\rm c0}}{\Gamma\left(1 - \gamma/2\right)} \left(\frac{\theta}{\sqrt{2}\sigma} \right)^{-\gamma}. \tag{6.8}$$

Since we (implicitly) assume here that the mean reddening profile of MSFR, equation (6.1), is explained in the clustered dust model, the value of γ in equation (6.5) should match the MSFR result. In order to confirm the validity of the assumption, we first choose $I_{\rm s0}$, $I_{\rm c0}$, C, and γ as free parameters, and fit to the observed profile imposing $I_{\rm s0} \geq 0$ and $I_{\rm c0} \geq 0$. The resulting best-fit value, $\gamma = 1.07 \pm 0.16$, is consistent with that of MSFR, $\gamma = 0.86 \pm 0.19$ (the other best-fit values include $I_{\rm s0} = 0$[MJy sr^{-1}], $I_{\rm c0} = (3.5 \pm 0.4) \times 10^{-3}$[MJy sr^{-1}], and $C = 1.399 \pm 0.035$[MJy sr^{-1}]). Indeed as Figure 6.2 illustrates, the difference among the predicted profiles for $0.65 < \gamma < 1.05$ is very small for the angular scales of our interest $\theta \gg \sigma$. The departure from the power-law for $I_{\rm c} < 6 \times 10^{-4}$[MJy sr^{-1}] is not a problem because it simply reflects the sensitivity to the subtracted offset C.

Thus we fix $\gamma = 0.86$ in what follows, and obtain the best-fit parameters as $I_{\rm s0} = (6.1 \pm 4.0) \times 10^{-4}$[MJy sr^{-1}], $I_{\rm c0} = (3.1 \pm 0.7) \times 10^{-3}$[MJy sr^{-1}], and $C = 1.399 \pm 0.035$[MJy sr^{-1}]. The best-fit profile for each component is shown in Figure 6.2.

The stacked FIR emission profile corresponding to the clustering term for $\gamma = 0.86$ is finally given as

$$\langle I_{100\mu{\rm m}} \rangle(\theta) = \frac{(7.0 \pm 1.6) \times 10^{-3}}{\rm MJy\ sr^{-1}} \left(\frac{\theta}{1'.0} \right)^{-0.86}, \tag{6.9}$$

at large θ, which plays a major role in the discussion presented in Section 6.3.3.

We note that while the statistical error of C is much larger than the best-fit values of $I_{\rm s0}$ and $I_{\rm c0}$ themselves, it does not affect the detection significance of the dust emission from SDSS galaxies. In fact, the variance of C simply comes from that of the Galactic dust over the SDSS survey area; the majority of the 400 jackknife subsamples indicates similar signatures of the dust emission, except for the difference of C.

The good agreement between the observed stacked profile and the prediction from the summation of individual SDSS galaxies is already interpreted to be supporting the clustered dust model. Nevertheless we will present an independent and complementary analysis to constrain the spatial extent of dust in the rest of this section.

6.3.2 Predictions in the clustered dust model

While the dust extinction is mainly sensitive to properties of dust grains, the dust emission depends on their temperature as well. Therefore, if the measured extinction and emission come from the same dust distribution, their ratio is a sensitive measure of the dust temperature. In this subsection, we will explicitly show theoretical expressions for the reddening and emission of dust in the clustered dust model. Since we are interested in the scales far beyond the galactic disk scale, we consider the clustering term alone.

The angular profile of dust extinction and emission around a galaxy is calculated by integrating the dust surface density $\Sigma_{\rm d}(r_p, z)$ of nearby galaxies at z separated by the projected distance $r_p = d_A(z)\theta$ from the central galaxy, where $d_A(z)$ is the angular diameter distance at z. Assuming that the 3-dimensional correlation function of galaxies follows a single power-law:

$$\xi(r, z) = \left(\frac{r}{r_0(z)} \right)^{-\alpha}, \tag{6.10}$$

the 2-dimensional projected dust surface density responsible for the clustering term is given by

$$\begin{aligned} \Sigma_{\rm d}(r_p, z) &= M_{\rm d}(z) \bar{n}(z) \int_{-\infty}^{\infty} \xi\big(\sqrt{r_p^2 + \chi^2}, z\big) d\chi \\ &= M_{\rm d}(z) \bar{n}(z) w_p(r_p, z), \end{aligned} \tag{6.11}$$

where $M(z)$ is the average mass of dust associated with a galaxy at z, $\bar{n}(z)$ is the average comoving number density of galaxies at z, and the 2-dimensional projected correlation function is defined as

$$w_p(r_p, z) = r_p \left(\frac{r_p}{r_0(z)} \right)^{-\alpha} \Gamma\left(\frac{1}{2}\right) \Gamma\left(\frac{\alpha - 1}{2}\right) \Big/ \Gamma\left(\frac{\alpha}{2}\right), \tag{6.12}$$

and $\Gamma(x)$ is Gamma function. For simplicity, we assume that the dust mass per one galaxy, $M_{\rm d}(z)$, depends on z alone, neglecting its dependence on the morphology of galaxies. Thus, equation (6.11) reduces to a single power-law:

$$\Sigma_{\rm d}(r_p, z) = \Sigma_{\rm d0}(z) \left(\frac{r_p}{r_{p,0}}\right)^{-\gamma}, \tag{6.13}$$

where $\gamma = \alpha - 1$, and

$$\Sigma_{\rm d0}(z) = M_{\rm d}(z)\bar{n}(z)r_0(z) \left(\frac{r_{p,0}}{r_0(z)}\right)^{-\gamma} \Gamma\left(\frac{1}{2}\right)\Gamma\left(\frac{\gamma}{2}\right) \Big/ \Gamma\left(\frac{1+\gamma}{2}\right). \tag{6.14}$$

Since we adopt the clustered dust model, the power-law index γ is set to that of the galaxy angular correlation function, equation (6.5), specifically $\gamma = 0.86$ in what follows. Thus the redshift evolutions of the dust mass $M_{\rm d}$, the number density $\bar{n}$, and the correlation length r_0 of galaxies are effectively absorbed in the evolution of $\Sigma_{\rm d0}(z)$, as long as γ is time-independent as assumed here.

Under the above assumptions, the angular extinction profile of dust at redshift z is written as

$$\begin{aligned} E_{g-i}(\theta, z) &= \frac{2.5}{\ln 10}\left[\tau\left(\theta, \frac{\lambda_g}{1+z}\right) - \tau\left(\theta, \frac{\lambda_i}{1+z}\right)\right] \\ &= \frac{2.5}{\ln 10}\left[\kappa_{\rm ext}\left(\frac{\lambda_g}{1+z}\right) - \kappa_{\rm ext}\left(\frac{\lambda_i}{1+z}\right)\right] \Sigma_{\rm d}\big(d_A(z)\theta, z\big), \end{aligned} \tag{6.15}$$

where $\kappa_{\rm ext}(\lambda)$ is the extinction cross-section per unit dust mass at a wavelength of λ, and λ_g, λ_i are the rest-frame wavelengths of SDSS g and i-bands, respectively. The average angular extinction profile around SDSS galaxies is then given by

$$\begin{aligned} \langle E_{g-i}\rangle(\theta) = \frac{2.5}{\ln 10}&\left[\int_0^\infty \frac{dN}{dz}dz\right]^{-1} \\ &\times \int_0^\infty \left[\kappa_{\rm ext}\left(\frac{\lambda_g}{1+z}\right) - \kappa_{\rm ext}\left(\frac{\lambda_i}{1+z}\right)\right] \Sigma_{\rm d0}(z) \left(\frac{d_A(z)\theta}{r_{p,0}}\right)^{-\gamma} \frac{dN}{dz}dz, \end{aligned} \tag{6.16}$$

where dN/dz is the redshift distribution of SDSS galaxies. Following MSFR, we adopt an approximation (Dodelsonet al., 2002):

$$\frac{dN}{dz} \propto z^2 e^{-(z/0.187)^{1.26}}, \tag{6.17}$$

and we obtain the number-weighted mean redshift of the sample as

$$\langle z\rangle = \frac{\int z(dN/dz)dz}{\int (dN/dz)dz} = 0.36. \tag{6.18}$$

One can similarly compute the angular FIR emission profile around SDSS galaxies. Since the dust emission at $\lambda = 100\mu$m is well approximated by blackbody, the corresponding surface brightness at redshift z is given as

$$I_{100\mu{\rm m}}(100\mu{\rm m}, \theta, z) = \frac{1}{(1+z)^4} B_\nu\left(\frac{100\mu{\rm m}}{1+z}, T_{\rm d}\right) \kappa_{\rm abs}\left(\frac{100\mu{\rm m}}{1+z}\right) \Sigma_{\rm d}\big(d_A(z)\theta, z\big), \tag{6.19}$$

where $\kappa_{\rm abs}$ is the absorption cross section per unit dust mass, B_ν is the blackbody spectrum per unit frequency, $T_{\rm d}$ is the dust temperature, which we assume to be independent of z, and the same for all SDSS galaxies, and $1/(1+z)^4$ comes from the cosmological dimming effect.

The average angular emission profile of SDSS galaxies, which corresponds to $I_{\rm c}(\theta)$ observed by the stacking analysis, is given as

$$\langle I_{100\mu{\rm m}}\rangle(\theta) = \left[\int_0^\infty \frac{dN}{dz}dz\right]^{-1} \int_0^\infty \frac{1}{(1+z)^4} B_\nu\left(\frac{100\mu{\rm m}}{1+z}, T_{\rm d}\right) \times \kappa_{\rm abs}\left(\frac{100\mu{\rm m}}{1+z}\right)\Sigma_{\rm d0}(z)\left(\frac{d_A(z)\theta}{r_{p,0}}\right)^{-\gamma}\frac{dN}{dz}dz. \quad (6.20)$$

Because both equations (6.20) and (6.16) follow the single power-law with the same index, the ratio of the emission to the extinction is independent of θ, and written in terms of $\kappa_{\rm ext}$, $\kappa_{\rm abs}$, and $T_{\rm d}$. This is what we expect in the clustered dust model as indicated also from the observed profiles, equations (6.1) and (6.9).

The observed profile of the emission to reddening ratio is shown in Figure 6.3. The filled circles are plotted using the residual of the emission profile, from which the best-fit single term and the offset level assuming $\gamma = 0.86$ are subtracted. The red solid curve shows the ratio of the best-fit clustering term, $I_{\rm c}(\theta)$, with $\gamma = 0.86$ to equation (6.1), and shaded region indicates its uncertainty that comes from the statistical error of $I_{\rm c0}$ and the amplitude of equation (6.1). The uncertainty of the power-law index in equation (6.1) is not considered here. At small θ, the emission profile is suppressed due to the SFD/IRAS PSF effect, whereas the ratio converges to a constant at large scale. The emission to reddening ratio at large θ limits is given by equations (6.1) and (6.9) as $\langle I_{100\mu{\rm m}}\rangle/\langle E_{g-i}\rangle = 4.7 \pm 1.6$ [MJy sr^{-1}mag^{-1}], which corresponds to the shaded regions in Figure 6.4 below.

We also consider to what extent this result is sensitive to the choice of the power-law index γ, which is fixed as 0.86 in the analysis above. We repeat both the fitting to the observed profile and the theoretical calculation of equation (6.16) and (6.20), varying the value of γ from 0.65 to 1.05. Figure 6.3 shows the observed emission to reddening ratio assuming $\gamma = 0.65$, 0.86 and 1.05. The average ratio changes approximately ~ 20 per cent (and its fractional uncertainty is similar to that for the case of $\gamma = 0.86$, although it is not shown in Figure 6.3). We also make sure that the theoretical value from equation (6.16) and (6.20) changes by 10 per cent according to the corresponding change of γ. Consequently, we find that the constraint of dust temperature below is affected at most by $\sim$ 1K within this range of γ.

6.3.3 Constraints on dust temperature

The solid and dashed lines in Figure 6.4 indicate the expected emission to extinction ratio as a function of $T_{\rm d}$. For $\kappa_{\rm ext}$ and $\kappa_{\rm abs}$, we adopt the values from the dust model by Weingartner & Draine (2001) [2] for Milky Way ($R_V = 3.1$) and SMC dust, for solid and dashed lines, respectively.

Here the redshift dependence of $\Sigma_{\rm d0}(z)$ is neglected and assumed to be constant just for simplicity. Incidentally we made sure that the z-dependence of $\Sigma_{\rm d0}(z)$ does not signifi-

[2]Data is taken from Web-site of B. T. Draine, http://www.astro.princeton.edu/ draine/dust/dustmix.html.

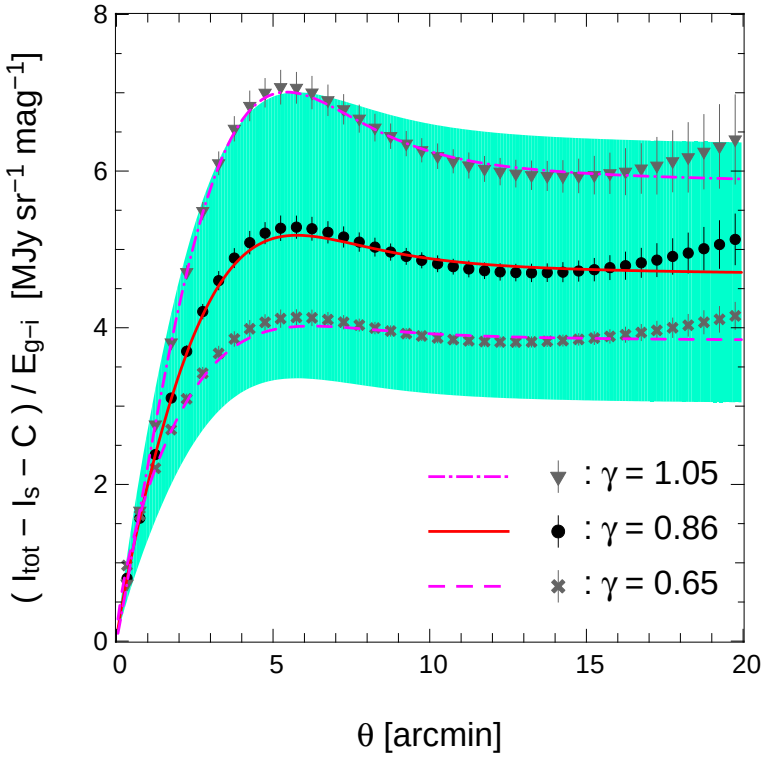

Figure 6.3: Radial profile of 100μm emission to reddening ratio. Filled circles (black) indicate the observed 100μm emission profile of the stacking analysis divided by the MSFR reddening profile, where the best-fit single term $I_{\rm s}(\theta)$ and the offset level C assuming the 2PCF index as $\gamma = 0.86$ are subtracted. Red solid curve is the best-fit profile of the clustering term $I_{\rm c}(\theta)$ with $\gamma = 0.86$, divided by $E_{g-i}(\theta)$ of MSFR. Shaded region indicates the uncertainty of the emission to reddening ratio where the statistical error of $I_{\rm c0}$ and the MSFR measurement is taken into account. Crosses (filled triangles) and dashed (dot-dashed) curve indicate the same as filled circles and solid curve, but for $\gamma = 0.65$ (1.05).

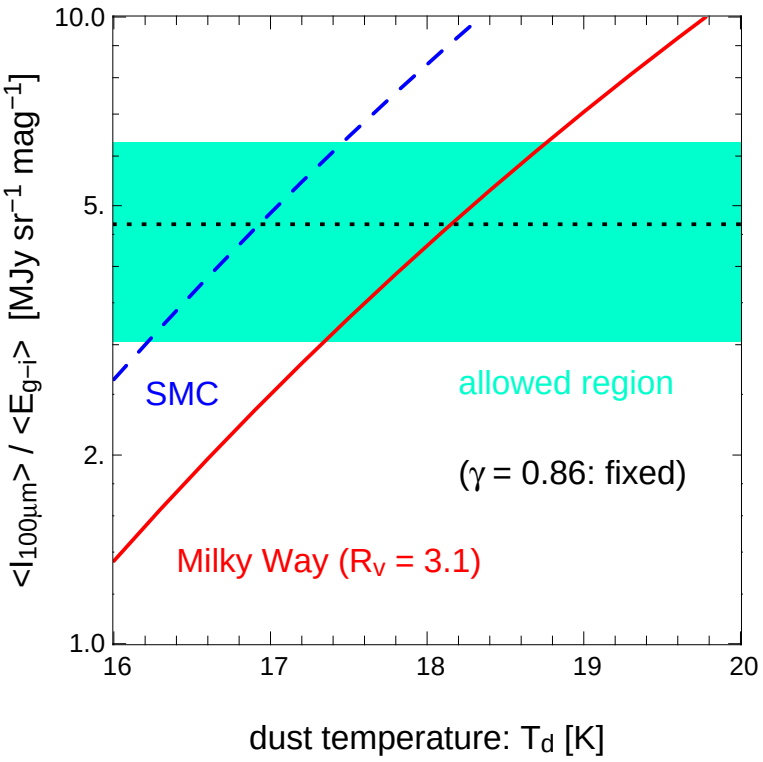

Figure 6.4: Constraints on the FIR emission to extinction ratio from MSFR and the stacking results (shaded region). Solid and dashed lines indicate the prediction for Milky Way ($R_V = 3.1$) and SMC dust model (Weingartner & Draine, 2001), respectively. The power-law index of galaxy 2PCF is fixed as $\gamma = 0.86$. If $\gamma = 0.65$ and 1.05 is assumed, the allowed region is shifted by -20 and 20 per cent, respectively.

cantly change the result; if we assume $\Sigma_{\rm d0}(z) \propto (1+z)^p$ for instance, the model prediction of $\langle I_{100\mu{\rm m}}\rangle/\langle E_{g-i}\rangle$ changes by ∓ 15 per cent for $p = \pm 1$, and the dust temperature constraint changes by ± 0.2K. The recent measurement of dust mass function by Dunne (2011) found that the cosmic dust mass density in sub-mm galaxies rapidly increases with redshift up to $z \sim 0.5$. Thus the constraint on the dust temperature below may be slightly underestimated.

Figure 6.4 indicates that the dust model predictions and the observed region are consistent if $T_{\rm d} = 18.2^{+0.6}_{-0.9}$K for MW dust, and $T_{\rm d} = 17.0^{+0.5}_{-0.8}$K for SMC, thus the obtained constraints are almost insensitive to the choice of dust model.

Given several approximations adopted in our simple models, the quoted statistical errors may underestimate the real uncertainty of the dust temperature. Nevertheless it is encouraging that the derived dust temperature is in good agreement with that of the typical interstellar dust around the central parts of galaxies (Schlegel, Finkbeiner, & Davis , 1998; Clemens et al., 2013). This result may support, at least in consistent with, the clustered dust model.

The dust temperature in the extended dust model is highly uncertain due to the lack of direct observations of dust in intra-cluster and intergalactic environments. The observation of M31 reported 15K near the edge of its disk (Draine, 2014), therefore the dust temperature in the outskirt is naturally expected to be much lower. Indeed, if we assume

the heating source of intergalactic dust is dominated by the cosmic UV background, which is lower than the ISRF in the solar neighborhood by two orders of magnitude (e.g., Madau & Pozzetti, 2000; Gardner et al., 2000; Xu et al., 2005), equation (2.42) follows the dust temperature of $\simeq$ 10K, much lower than that from our constraint. On the other hand, Yamada & Kitayama (2005) suggested a possibility that the dust temperature reaches $\sim$ 30K, if collisional heating by hot plasma and injection of dust grains into intrahalo space is sufficiently efficient. In this respect, we cannot exclude the extended dust model at this point. Nevertheless further improvements in model predictions and the observations in future would put more stringent constraints on the spatial extent of dust through the measurement of dust temperature as we proposed in this Chapter.

The radial dust profile expected from the clustered dust model can be independently computed when the galaxy correlation function and the dust optical depth within single galactic disk are given. Comparing the expected profile with equation (6.1), we further discuss the validity of the clustered dust model in what follows.

Muñoz-Mateos et al. (2009) derived the radial dust profile of the nearby galaxies from the SINGS (*Spitzer* Infrared Nearby Galaxies Survey) sample, combining with the UV images observed by GALEX (Galaxy Evolution Explorer). They found that the median value of the far-UV extinction at $\sim$ 30kpc from the centers of galaxies as $A_{\rm FUV} \sim 1$ mag, which corresponds to $E_{g-i} \sim 0.2$ mag adopting the conventional Galactic reddening laws (Cardelli et al., 1989; Fitzpatrick, 1999).

Just for simplicity, we approximate the galaxies as the circular disks with the radius of $r_{\rm disk}$ hereafter. We also assume that all the galaxies are located at the median redshift of MSFR sample, $\langle z \rangle \sim 0.36$, and the extinction due to the galactic dust, $E^{\rm disk}_{g-i}$, is constant within those disks. Under these approximations, the dust reddening profile expected by the clustered dust model is given by

$$E^{\rm clu}_{g-i}(\theta) = E^{\rm disk}_{g-i} \pi \left(\frac{r_{\rm disk}}{d_A(z=0.36)} \right)^2 \bar{n} w_{\rm gg}(\theta), \tag{6.21}$$

where $\bar{n}$ denotes the average surface number density of the galaxies, and $w_{\rm gg}(\theta)$ is the angular auto-correlation function of the galaxies. MSFR computed $w_{\rm gg}(\theta)$ for their galaxy sample and found that the dust-to-galaxy ratio defined as

$$\beta_{g-i}(\theta) \equiv \frac{\langle E_{g-i} \rangle(\theta)}{w_{\rm gg}(\theta)}, \tag{6.22}$$

is ~ 0.015 mag, almost independent of θ, where $\langle E_{g-i} \rangle(\theta)$ is given by equation (6.1). This follows

$$w_{\rm gg}(\theta) \simeq 0.1 \left(\frac{\theta}{1'.0} \right)^{-0.86}. \tag{6.23}$$

Adopting equation (6.23) and $\bar{n} = 1.8$ arcmin^{-2}, equation (6.21) reduces to

$$E^{\rm clu}_{g-i}(\theta) = 1.1 \times 10^{-3} \left(\frac{E^{\rm disk}_{g-i}}{0.2} \right) \left(\frac{r_{\rm disk}}{30{\rm kpc}} \right)^2 \left(\frac{\theta}{1'.0} \right)^{-0.86}. \tag{6.24}$$

This result is in reasonable agreement with equation (6.1), which would favor the clustered dust model. The SINGS sample, for which the fiducial values adopted for $E^{\rm disk}_{g-i}$ and $r_{\rm disk}$

are originally derived, is mainly consists of spiral galaxies, therefore those values might be larger than the representative ones for the entire SDSS galaxies. However, this result indicates, at least, that a non-negligible fraction of the dust reddening found by MSFR would be explained by the sum of the dust confined in galactic disks.

6.4 Summary

The spatial distribution of dust is of fundamental importance in understanding the star formation and metal circulation in the universe. It is also crucial in correcting for the magnitude of distant objects due to the resulting reddening/extinction (Aguirre, 1999; Ménard et al., 2010b; Fang et al., 2011).

In Chapter 4, we have detected the FIR dust emission from SDSS galaxies via their stacking image analysis, and found that the amount of dust emission is largely responsible for the observed anomaly in the surface density of SDSS galaxies as a function of the SFD extinction (Yahata et al., 2007, Chapter 5). Our model implicitly assumed that the dust of each galaxy is locally confined in the galactic disk scale, and that the observed FIR emission within the large PSF width (FWHM= $6'.1$) is simply a sum of contributions of individual galaxies (the clustering dust model). In contrast, the dust around a galaxy may be indeed spatially extended up to $\sim$ 1Mpc (the extended dust model), as claimed by Ménard et al. (2010a) and more recently by Peek, Ménard & Corrales (2014) through the correlation of background object colors against the separation of foreground galaxies.

In order to distinguish between the two models, we attempt to constrain the temperature of dust by combining the absorption (detected through reddening of quasars) and emission (detected through the stacking of galaxies) features. Assuming that the nature of galactic dust is described by those of MW and SMC, we find that the dust temperature is approximately 18K. The temperature is consistent with that of the galactic dust in the central region, but too high for the conventional prediction for the intra-cluster dust.

Given several simplification and approximations that we adopted in the present analysis, the associated error-bars of the derived dust temperature is fairly uncertain. The main purpose of the present paper is to propose a new observational method to diagnose the nature of galactic dust. Therefore we do not argue that our present result rules out the extended dust model, but conservatively conclude that it favors the clustering dust model at this point.

Our proposed method can be improved in many ways; the redshift evolution of the temperature and amount of dust may be considered from theoretical models, the distribution of dust temperature for different galaxies may be taken into account, the amount of dust emission should depend on the morphology of stacked galaxies, and the stacking analysis may be repeated in other wavelengths. In particular, the current result is significantly limited by the poor angular resolution of *IRAS*. In those respects, the higher-angular-resolution and multi-band far-infrared data by AKARI (Murakami et al., 2007) are very promising.

Chapter 7

Summary and Conclusions

Since dust grains scatter and absorb the light in ultra-violet to near infrared regime, dust extinction has been one of the major systematics for the extragalactic observations. The fluxes and colors of extragalactic objects, and the large scale structure of the universe is accessible only after the dust extinction is accurately corrected for.

A dominant origin of the dust extinction is the Galactic dust. Currently, the SFD map (Schlegel, Finkbeiner, & Davis , 1998) is the most-widely used for the correcting for the Galactic dust extinction throughout the entire fields of astronomy. It has been suggested, however, that the SFD map suffers from the systematics, possibly due to the contamination of FIR emission from galaxies (Yahata et al., 2007).

In this thesis, we presented further investigation of the FIR contamination of the galaxies. In Chapter 4, we first directly detected the FIR emission of SDSS galaxies in the SFD map using the stacking analysis, validating the hypothesis of the FIR contamination first proposed by Yahata et al. (2007). The systematics due to SDSS galaxy emission is of the order of 10^{-3} in r-band extinction, which is roughly consistent with the value suggested by Yahata et al. (2007).

In Chapter 5, we next confirmed the anomaly of the SFD map using the updated SDSS DR7 data, and independently modeled the anomaly of the surface number density in the vicinity of the FIR contamination, in both numerical and analytical fashion. We found that the amount of FIR contamination required to *quantitatively* reproduce the observed anomaly is consistent with the values measured by the stacking analysis above. This indicates that the observed anomaly is well explained by the hypothesis of FIR contamination.

The systematics due to FIR contamination is quite small, therefore it would not significantly affect the measurement of individual objects. Since the FIR contamination, however, is correlated with the spatial distribution of galaxies, it would statistically and systematically affect the cosmological implications from galaxy surveys or CMB (Cosmic Microwave Background), if the SFD map is used to correct for the Galactic dust foreground. The effects of the FIR contamination could be important, in particular, for the future large galaxy surveys, e.g, Euclid, LSST, etc. We therefore attempted to correct the SFD map by subtracting the FIR emission from SDSS galaxies, following the empirical relation between their optical flux and FIR emission measured by the stacking analysis. We found that, however, our correction does not work well for the purpose of removing the anomaly. This probably implies that more sophisticated estimate of FIR emission from galaxies, including its dependence on morphology, luminosity, and redshift, is essentially

important.

Another possible origin of the dust extinction is the intergalactic dust, which is ejected from galactic disks and smoothly fills the intergalactic space. If a significant amount of such intergalactic dust exists, its extinction systematically affects the measurement of distant objects.

In Chapter 6, we focused on the recent result by (Ménard et al., 2010a, MSFR). MSFR detected the reddening of distant quasars up to few Mpc from the foreground galaxies, using the angular cross-correlation analysis. This scale is far beyond the typical galactic disks, therefore their measurement may imply that the dust is universally expelled from interstellar space and extending out to intergalactic space.

On the other hand, since the reddening profile measured by MSFR is similar to that of angular correlation function of galaxies, we propose that MSFR measurement might be equally explained by the statistical sum of the dust, which is confined within the galactic disk scale, due to galaxy spatial clustering. Our hypothesis is confronted with the stacking analysis result for the same galaxy sample as MSFR. Combined with the reddening measurement by MSFR, the detected FIR emission provides the information of the dust temperature. We put the constraint on the dust temperature as $\sim 18 \pm 1$K, which is consistent with the typical temperature of interstellar dust. This results may be supporting our hypothesis, but further investigation is needed to overcome the underlying uncertainties in our constraint, which comes from our simplified model calculation.

Stacking analysis of galaxies provides a unique opportunity for investigating statistical relations among galaxy properties in different wavelength and to infer the angular cross-correlation of galaxies, much beyond the magnitude limit for individual galaxy surveys. Combining various sky maps in different wavelengths, e.g., AKARI, WISE, Planck (Tauber et al., 2010), etc., stacking analyses will enable us to extensively study the dust content of galaxies.

Appendix A

IRAS Point Spread Function

In subsection 4.2.2, we decompose the stacked radial profiles into single and clustering terms, assuming the Gaussian PSF. Since the IRAS PSF is known to be very complex, we need to check the validity of this assumption. For the purpose of determining the PSF directly, we perform similar stacking analysis with SDSS stars.

More specifically, we select spectroscopic stars brighter than $m_r = 17.0$ (12823 stars in total) from the SDSS DR7 catalog. We first stack the SFD map centered on those SDSS stars as we did for SDSS galaxies and quasars, but we find no significant signature. This is mainly because the bright point sources in the IRAS catalogue are already removed from the SFD map. Therefore we go back to the original ISSA $100\mu m$ diffuse map, and perform the stacking analysis. The resulting stacked average radial profile of the SDSS stars is shown in Figure A.1. The data points are well approximated by a single Gaussian. The best-fit Gaussian shown in the dashed curve has a width of $\sigma = 2'.42$, which is slightly smaller than that found in subsection 4.2.2. This is understood because since the SFD map is constructed by further smoothing the original ISSA map. Thus we conclude that our assumption of the Gaussian PSF is valid.

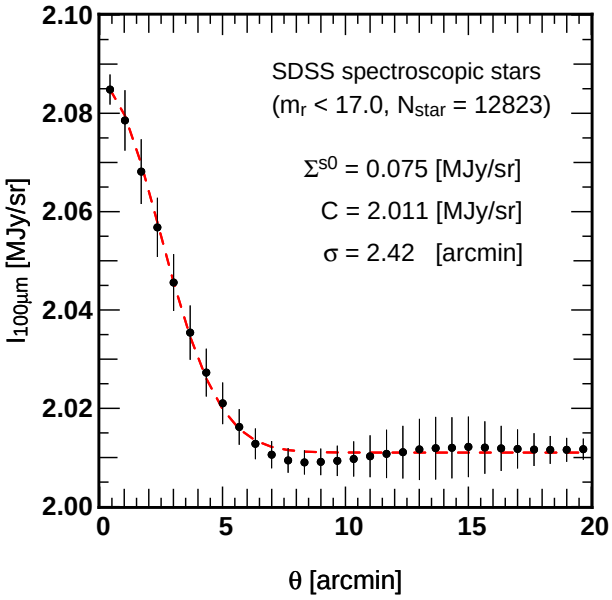

Figure A.1: Radial profiles of stacked star images. The dashed curve indicates the best-fit Gaussian profile.

Appendix B

Discussion on the origin of the correlation between the Galactic foreground and SDSS galaxies

In Chapter 4, we presented the stacking analysis of the SFD map centered on the SDSS photometric galaxies, and performed the model fit to the radial profiles of the stacked images. Our model for the radial profile is described by equations (4.5), (4.10), and (4.12), where we assumed that the radial profiles are decomposed into the contributions of central galaxy (single term; $\Sigma_{\rm g}^{\rm s0}$), neighbor galaxies (clustering term; $\Sigma_{\rm g}^{\rm c0}$), and the Galactic dust emission (C). As a result of the profile fit, we found that the best-fit values of C systematically decreases against the apparent magnitude of the galaxies, m_r, on contrary to the expectation (see Figure 4.13). In this Appendix, we present the several attempts to clarify the origin of this anomalous correlation.

In the case that the spatial distribution of the SDSS galaxies is completely uniform, i.e., if those galaxies are Poisson distributed, C should not indicate any systematic dependence on properties of the galaxies. Therefore the origin of the systematic trend of C could be related to the inhomogeneities of the spatial distribution of galaxies.

Figure B.1 shows the 2-dimensional projected over-densities of the SDSS galaxies, $\delta_{\rm gal} \equiv n_{\rm gal}/\bar{n}_{\rm gal} - 1$, for five magnitude bins with $\Delta m_r = 1.0$. Here we computed the surface number densities, $n_{\rm gal}$, for each grid divided by $\Delta\alpha = 3^\circ.6, \Delta\delta = 1^\circ.8$. The surface density of the brightest sample ($15.5 < m_r < 16.5$) exhibits the large fluctuations, in particular, $\delta_{\rm gal}$ is significantly large where $210^\circ < \alpha < 250^\circ$ and $\delta < 30^\circ$. Comparison with the SFD map (the bottom right panel of Figure B.1) reveals that this over-dense region of the brightest sample coincidentally corresponds to the relatively high extinction region in the SFD map. Similar structures are also visible for the fainter magnitude bins, but the density contrast becomes weaker for fainter sample. Thus the stacking analysis over the bright galaxies likely to be biased to high extinction regions, which could be the origin of the correlation between C and m_r.

We repeat the stacking analysis and the radial profile fit excluding the over-dense regions shown as the dashed lines in the upper top panel of Figure B.1. The best-fit values of C, however, still indicate the correlation with m_r, as shown in top left panel of Figure B.2, while the best-fit values $\Sigma_{\rm g}^{\rm s0}$ and $\Sigma_{\rm g}^{\rm c0}$ are almost identical to those for the entire sky, except for $\Sigma_{\rm g}^{\rm s0}(m_r < 18.0)$. Thus we conclude that the over-dense regions excluded here is not the dominant origin of the anomalous trend.

We next suspected that the systematic trend of C might be due to the contamination of the Galactic stellar objects in our SDSS galaxy sample. Since the number densities of stars relative to that of SDSS galaxies is larger for brighter magnitudes, the contamination of stars would be more significant for brighter galaxy sample. On the other hand, the spatial distribution of stars is correlated with that of the Galactic dust, therefore the stacking analysis over brighter galaxy sample would return systematically larger values of C.

Since the effect of the star contamination is expected to be small for high galactic latitudes, we repeat the stacking analysis excluding the regions with low galactic latitudes, as $b > 30°$, $b > 45°$, $b > 60°$ (dashed lines in the top right panel of Figure B.1). The results are shown in the middle panels of Figure B.2. Although the strength of the correlation varies, the systematic trend of C still remains for all the cases. Thus we find that the stellar contamination would not explain the correlation between C and m_r.

We also tested to what extent the photometry flag selection, which is adopted through this thesis, affect the correlation between C and m_r. The results for the galaxy sample without any photometry flag selection are shown in the bottom panels of Figure B.2, however, the systematic trend of C is still clearly seen.

Thus we could not identify the origin of the correlation between C and m_r so far. This anomalous correlation could be due to the inhomogeneities of the survey completeness of SDSS. The offset level of the Galactic foreground would be larger for fainter objects, if the completeness of the original SDSS photometric sample is systematically worse for fainter objects in high extinction regions, possibly due to the Galactic extinction itself and/or other observational problems correlated with the Galactic foreground. Although the survey completeness would not significantly varies over the SDSS survey area, it may partially explain the correlation between C and m_r, given that the difference of C between the brightest and the faintest sample is subtle, $\sim$ 1 mmag, and needs to be further investigated.

We emphasize that the best-fit values for the FIR emission of galaxies, $\Sigma_{\rm g}^{\rm s0}$ and $\Sigma_{\rm g}^{\rm c0}$, are hardly affected by the choice of the survey area as we presented above, while the offset values of C significantly varies. Thus we expect that the dependence of C on m_r is not due to the FIR emission of galaxies themselves, and the result for $\Sigma_{\rm g}^{\rm s0}$ and $\Sigma_{\rm g}^{\rm c0}$ would be reliable.

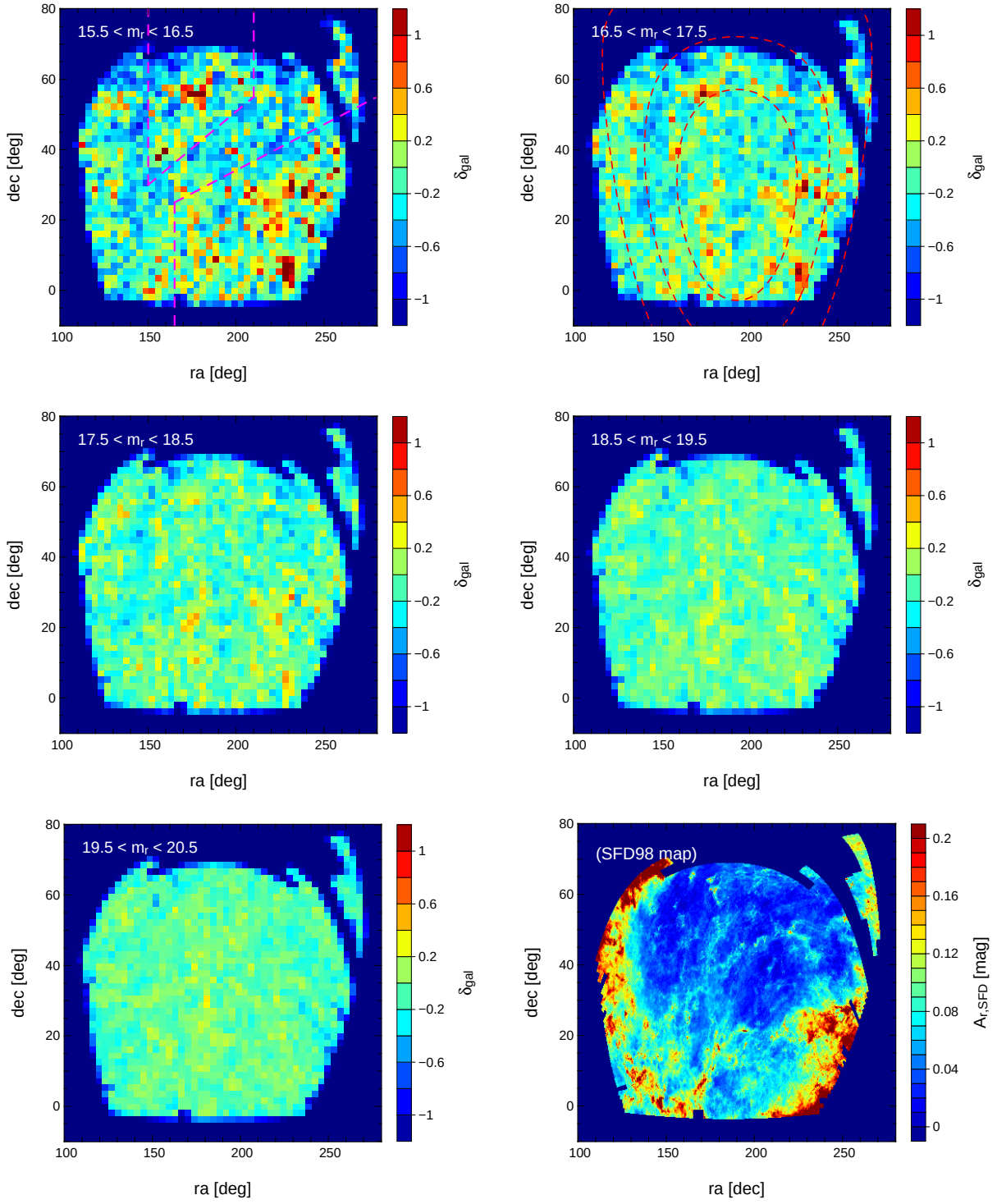

Figure B.1: Over-densities of the SDSS galaxies for magnitude bin of $\Delta m_r = 1.0$ mag. The dashed lines in the top left panel (magenta) show the over-dense regions excluded in the stacking analysis corresponding to the top panels of Figure B.2. The red dashed lines in the top right panel (red) indicate the galactic latitude $b = 30°, 45°, 60°$. The bottom right panel shows the r-band extinction of the SFD map over the SDSS survey area.

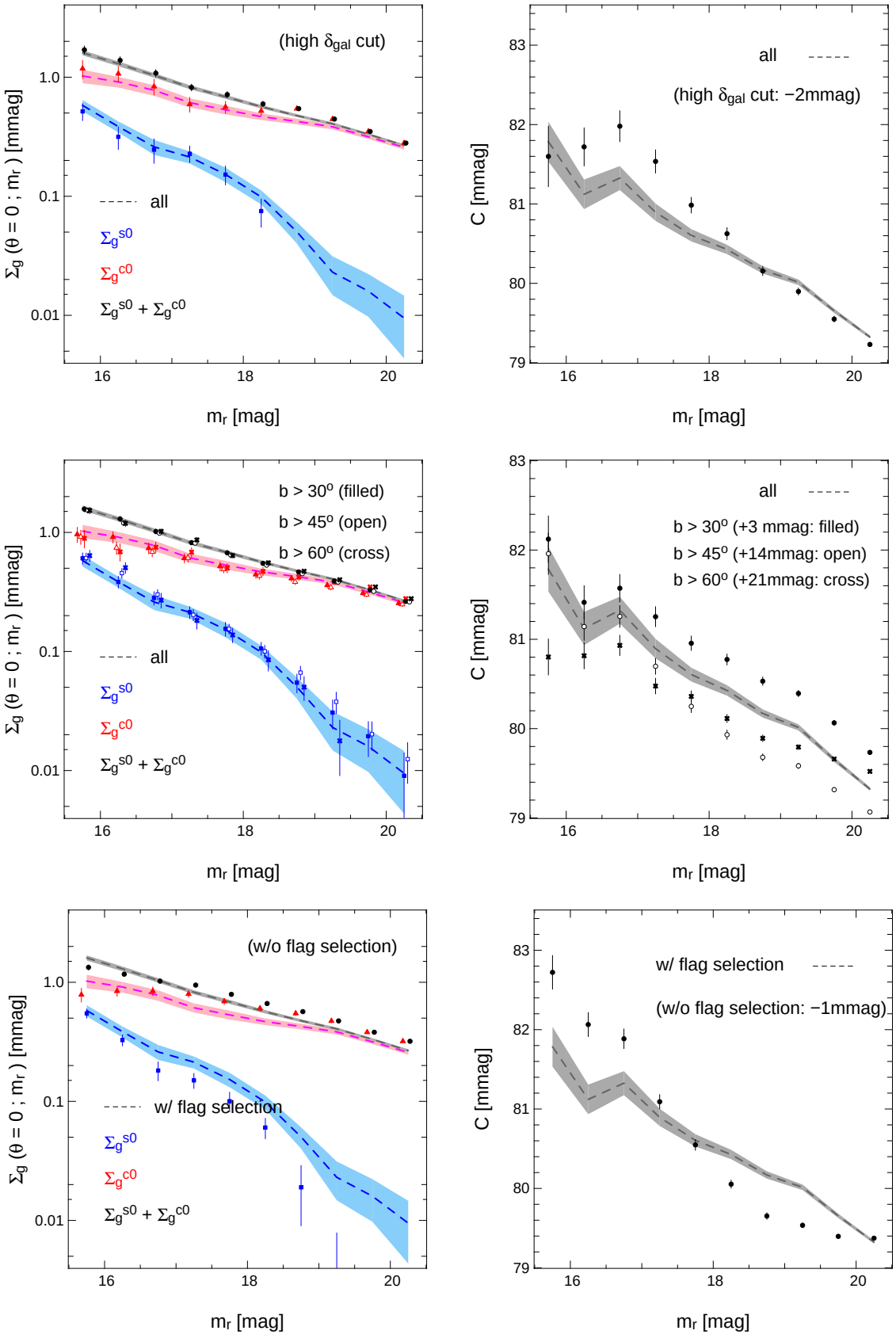

Figure B.2: The best-fit parameters of the radial profile fit excluding the over-dense regions of the brightest sample (top panels), and low galactic latitudes (middle panels). The bottom panels indicate the results for the galaxy sample without any photometry flag selection. Left panels indicate the best-fit values of Σ_g^{s0}, Σ_g^{c0}, and $\Sigma_g^{s0} + \Sigma_g^{c0}$. Right panels indicate the best-fit values of C, which are shifted for the ease of visual comparison. The shaded regions indicate the best-fit parameters for the entire galaxy sample with photometric flag selections, as the same as Figure 4.11.

Appendix C

Point Spread Function in Analytic Formulation

In the mock simulation (§5.3), we assign the FIR *fluxes* to the mock galaxies by modeling the PDF of FIR to optical luminosity ratio, y. On the other hand, their contribution to the contamination in the SFD map is determined by their *intensities* as

$$\Delta A_r = pk_r \frac{f_{100\mu\mathrm{m}}}{2\pi\sigma_{\mathrm{eff}}^2}, \tag{C.1}$$

where σ_{eff} is the Gaussian width of the effective PSF, thus the impact of the FIR contamination directly depends on σ_{eff} even for the mock galaxies with the same 100μm fluxes, $f_{100\mu\mathrm{m}}$. Due to the smoothing effects by the pixelization and interpolation of the SFD map, the effective PSF is degraded from that applied in the mock simulations (FWHM $= 5'.2$), which is aimed to mimic the purely instrumental PSF. Therefore, in order to precisely reproduce the mock simulation results by our analytic model (§5.4), we have to carefully evaluate the appropriate σ_{eff} to be applied in equation (D.30). In this appendix, we derive σ_{eff} as a function of the intrinsic PSF width, σ_{int}.

First we calculate the intensity of a single galaxy with a given 100μm flux and position, taking into account of the two smoothing effects. Hereafter, we assume that the pixels of the SFD map are squares with the sides, $\theta_{\mathrm{pix}} = 2'.372$. We denote the pixel of the SFD map, in which the galaxy is located, as Ω_0, and its neighbor pixels as Ω_1 to Ω_8. We define the 2-dimensional Cartesian coordinate system $\theta = (\theta_x, \theta_y)$, whose origin is at the center of Ω_0. The configuration of Ω_0 to Ω_8 is illustrated in the left panel of Figure C.1. The intensity of the galaxy with 100μm flux, f, in the pixel Ω_i $(i = 0, ..., 8)$ is given as

$$I_i(\theta_{\mathrm{g}}) = \frac{f}{2\pi\sigma_{\mathrm{int}}^2\Omega_{\mathrm{pix}}} \int_{\Omega_i} \exp\left(-\frac{|\theta - \theta_{\mathrm{g}}|^2}{2\sigma_{\mathrm{int}}^2}\right) d\theta, \tag{C.2}$$

where θ_{g} denotes the position of the galaxy, and $\Omega_{\mathrm{pix}} = \theta_{\mathrm{pix}}^2$ is the area of the pixels. Since the value of the SFD map extinction is evaluated by the linear CIC interpolation, the intensity of the galaxy depends on θ_{g}, but also the position where the value is evaluated, θ, and calculated as

$$I_{\mathrm{CIC}}(\theta, \theta_{\mathrm{g}}) = \left(1 - \frac{\theta_x}{\theta_{\mathrm{pix}}}\right)\left(1 - \frac{\theta_y}{\theta_{\mathrm{pix}}}\right) I_{i_1}(\theta_{\mathrm{g}}) + \left(1 - \frac{\theta_x}{\theta_{\mathrm{pix}}}\right)\frac{\theta_y}{\theta_{\mathrm{pix}}} I_{i_2}(\theta_{\mathrm{g}})$$

$$+\frac{\theta_x}{\theta_{\rm pix}}\frac{\theta_y}{\theta_{\rm pix}}I_{i_3}(\theta_{\rm g})+\frac{\theta_x}{\theta_{\rm pix}}\left(1-\frac{\theta_y}{\theta_{\rm pix}}\right)I_{i_4}(\theta_{\rm g}), \tag{C.3}$$

where $(i_1, ..., i_4)$ are the indices of the nearest 4 pixels to θ:

$$(\Omega_{i_1},\Omega_{i_2},\Omega_{i_3},\Omega_{i_4})=\begin{cases}(\Omega_0,\Omega_1,\Omega_2,\Omega_3) & (0<\theta_x<\frac{\theta_{\rm pix}}{2},0<\theta_y<\frac{\theta_{\rm pix}}{2})\\ (\Omega_0,\Omega_5,\Omega_4,\Omega_3) & (0<\theta_x<\frac{\theta_{\rm pix}}{2},-\frac{\theta_{\rm pix}}{2}<\theta_y<0)\\ (\Omega_0,\Omega_5,\Omega_6,\Omega_7) & (-\frac{\theta_{\rm pix}}{2}<\theta_x<0,-\frac{\theta_{\rm pix}}{2}<\theta_y<0)\\ (\Omega_0,\Omega_1,\Omega_8,\Omega_7) & (-\frac{\theta_{\rm pix}}{2}<\theta_x<0,0<\theta_y<\frac{\theta_{\rm pix}}{2}).\end{cases} \tag{C.4}$$

Since the resulting effective PSF also depends on θ and $\theta_{\rm g}$, we compute the PSF width appropriately averaged over θ and $\theta_{\rm g}$ in the following. In our analytic model (§5.4), we compute the expected $\Omega'(A')$ and $N'_{\rm gal}(A')$ under the presence of the FIR contamination of galaxies. We note that the effective PSF widths are slightly different for $\Omega'(A')$ and $N'_{\rm gal}(A')$. This is because the extinction contaminated by the FIR intensities, A', is always evaluated at the position of the galaxies, *i.e.,* $\theta=\theta_{\rm g}$, for $N'_{\rm gal}(A')$, while this is not the case for $\Omega'(A')$. Therefore we separately derive the effective PSF widths for $\Omega'(A')$ and $N'_{\rm gal}(A')$. We denote these effective PSF widths as $\sigma_{{\rm eff},\Omega}$ and $\sigma_{{\rm eff},N}$.

Now let us calculate $\sigma_{{\rm eff},\Omega}$. Since θ and $\theta_{\rm g}$ are independent for computing $\Omega'(A')$, we calculate the intensity of galaxies averaged over θ and $\theta_{\rm g}$ as

$$\bar{I}=\frac{1}{\Omega_{\rm pix}^2}\int_{\Omega_0}d\theta\int_{\Omega_0}d\theta_{\rm g}I_{\rm CIC}(\theta,\theta_{\rm g}). \tag{C.5}$$

We define $\sigma_{{\rm eff},\Omega}$ as

$$\frac{f}{2\pi\sigma_{{\rm eff},\Omega}^2}\equiv\bar{I}, \tag{C.6}$$

and this leads to

$$\sigma_{{\rm eff},\Omega}=\frac{4}{\sqrt{\pi}}\frac{\Omega_{\rm pix}}{\sigma_{\rm int}}\frac{1}{6F(s)-5F(0)-2F(-s)+F(-2s)}, \tag{C.7}$$

where

$$F(x)=\int{\rm erf}(x)dx=x\ {\rm erf}(x)+\frac{e^{-x^2}}{\sqrt{\pi}}, \tag{C.8}$$

$s=\theta_{\rm pix}/\sqrt{2}\sigma_{\rm int}$, and ${\rm erf}(x)$ denotes the error function.

Similarly, considering that $\theta=\theta_{\rm g}$, we define $\sigma_{{\rm eff},N}$ as

$$\frac{f}{2\pi\sigma_{{\rm eff},N}^2}\equiv\frac{1}{\Omega_{\rm pix}}\int_{\Omega_0}I_{\rm CIC}(\theta_{\rm g},\theta_{\rm g})d\theta_{\rm g}. \tag{C.9}$$

Equation (C.9) is reduced to

$$\sigma_{{\rm eff},N}=\frac{\Omega_{\rm pix}}{\sqrt{8\pi\mathcal{R}}}, \tag{C.10}$$

where

$$\begin{aligned}\frac{2\mathcal{R}}{\sigma_{\rm int}^2} &= \left[J_1\left(-\frac{\theta_{\rm pix}}{2}\right)-J_2\left(-\frac{\theta_{\rm pix}}{2}\right)\right]^2+2J_1\left(-\frac{\theta_{\rm pix}}{2}\right)J_2\left(\frac{\theta_{\rm pix}}{2}\right)\\ &\quad -2J_2\left(-\frac{\theta_{\rm pix}}{2}\right)J_2\left(\frac{\theta_{\rm pix}}{2}\right)+J_2\left(\frac{\theta_{\rm pix}}{2}\right)J_2\left(\frac{\theta_{\rm pix}}{2}\right),\end{aligned} \tag{C.11}$$

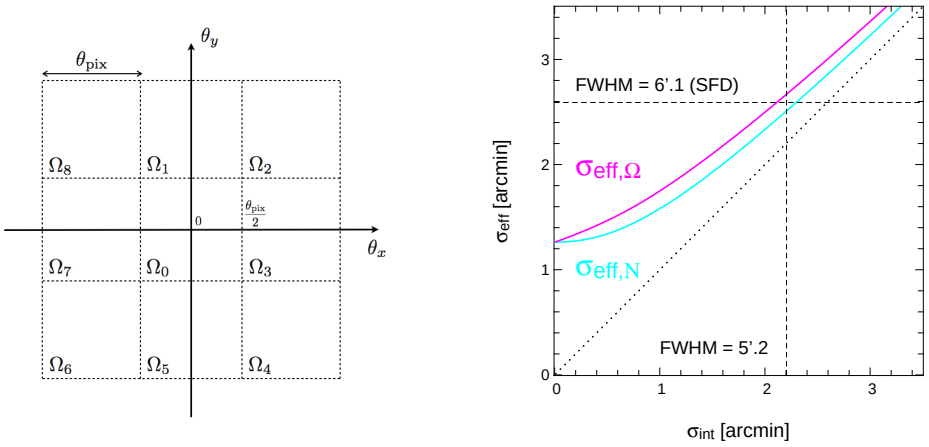

Figure C.1: *left panel;* Configuration of the SFD map pixels for calculating the effective PSF width. *right panel;* The effective Gaussian PSF widths, $\sigma_{\rm eff,\Omega}$ (magenta) and $\sigma_{{\rm eff},N}$ (cyan), as functions of the intrinsic PSF width $\sigma_{\rm int}$. The vertical and horizontal dashed lines indicate the Gaussian PSF width applied in the mock simulation (§5.3), and the resolution of the SFD map, respectively.

$$J_1(x) = \left[F(b+s) - F\left(b+\frac{s}{2}\right) - F(b) + F\left(b-\frac{s}{2}\right)\right], \tag{C.12}$$

$$J_2(x) = \frac{1}{s}\left[G(b+s) - G\left(b+\frac{s}{2}\right) - G(b) + G\left(b-\frac{s}{2}\right)\right] - \frac{1}{2}\left[F\left(b+\frac{s}{2}\right) - F\left(b-\frac{s}{2}\right)\right] + \frac{1}{2s}\left[\mathrm{erf}(b+s) - \mathrm{erf}\left(b+\frac{s}{2}\right) - \mathrm{erf}(b) + \mathrm{erf}\left(b-\frac{s}{2}\right)\right], \tag{C.13}$$

$$G(x) = \int x\ \mathrm{erf}(x)dx = \frac{1}{2}\left[x^2\mathrm{erf}(x) + \frac{1}{\sqrt{\pi}}xe^{-x^2} - \frac{1}{2}\mathrm{erf}(x)\right], \tag{C.14}$$

and $b \equiv x/\sqrt{2}\sigma_{\rm int}$.

The right panel of Figure C.1 shows the equations (C.7) and (C.10) as functions of $\sigma_{\rm int}$, which are adopted to equation (D.30) in the analytic model presented in Appendix D. In numerical simulations in §5.3, we adopted $\sigma_{\rm int} = 2'.21$, which reproduces the effective resolutions $\sigma_{\rm eff,\Omega}$ and $\sigma_{{\rm eff},N}$ both similar to the SFD angular resolution FWHM $= 6'.1$.

Appendix D

Details of the analytic formulation of the anomaly neglecting spatial clustering of galaxies

An analytic model that we present in Chapter 5 neglects the spatial clustering of galaxies, but it is, at least partially, incorporated by the assigned value of 100μm flux for each r-band selected galaxy. The interpretation is slightly subtle, but we would like to emphasize that the neglect of the spatial clustering in our analytic model is not serious in practice as discussed in §5.6.

Assume that galaxies are randomly distributed over the pixel, and denote the expected number of the galaxies of the *true* (albeit unobservable) apparent magnitude $m_{\rm true}$ being $m_{\rm min} < m_{\rm true} < m_{\rm max}$ by $\overline{N}$. Then the probability that the pixel has N galaxies obeys the Poisson distribution:

$$P_{\rm Poisson}(N|\overline{N}) = \frac{\overline{N}^N \exp(-\overline{N})}{N!}. \tag{D.1}$$

Here we assume that the area of all the pixels of the dust map is equal. Then the joint probability is the product of the conditional probability that the total FIR contamination in the pixel is ΔA, given that there are N galaxies and that the probability that the pixel has N galaxies:

$$P_{\rm joint}(\Delta A, N) = P_N(\Delta A) P_{\rm Poisson}(N|\overline{N}). \tag{D.2}$$

The conditional probability $P_N(\Delta A)$ can be computed recursively. When there is no galaxy in a pixel ($N = 0$), ΔA should vanish:

$$P_0(\Delta A) = \delta_D(\Delta A), \tag{D.3}$$

where δ_D is the 1-dimensional Dirac delta function. We compute $P_1(\Delta A)$ from the differential number count of galaxy magnitude and the PDF of the FIR to r-band flux ratio as discussed later in detail. Then $P_N(\Delta A)$ for $N \geq 2$ should satisfy the following recursive equation:

$$P_N(\Delta A) = \int_0^{\Delta A} dx P_1(x) P_{N-1}(\Delta A - x). \tag{D.4}$$

Finally the PDF of the total contamination in a pixel, $P(\Delta A)$, is given as

$$P(\Delta A) \;=\; \sum_{N=0}^{\infty} P_{\rm joint}(\Delta A, N) = \sum_{N=0}^{\infty} P_N(\Delta A) P_{\rm Poisson}(N|\overline{N}). \tag{D.5}$$

Note therefore that $P_{\rm joint}(\Delta A, N)$ and $P(\Delta A)$ are computed in a straightforward fashion once the two inputs, $P_1(\Delta A)$ and $\overline{N}$, are specified from the observed data.

Next let us proceed to compute $\Omega'(A')$ and $N'(A')$ according to this model. Since SFD subtracted the mean FIR contamination in a pixel in constructing the map, we also subtract its theoretical counterpart:

$$\overline{\Delta A} = \int_0^\infty d(\Delta A)\Delta A P(\Delta A), \tag{D.6}$$

from the FIR contamination ΔA in each pixel. So the extinction contaminated by the galaxy emission is now given by

$$A' = A + \Delta A - \overline{\Delta A}. \tag{D.7}$$

Therefore, the probability that a pixel with the *true* extinction A is observed as A' due to the FIR contamination is given by $P(\Delta A) = P(A' - A + \overline{\Delta A})$. Finally we obtain the expected observed distribution function of sky area, $\Omega'(A')$ as

$$\begin{aligned}\Omega'(A') &= \int_0^\infty dA \int_0^\infty d(\Delta A)\Omega(A)P(\Delta A)\delta_D\big(A' - (A + \Delta A - \overline{\Delta A})\big) \\ &= \int_0^{A'+\overline{\Delta A}} dA\Omega(A)P(A' - A + \overline{\Delta A}).\end{aligned} \tag{D.8}$$

We can similarly derive the expression for $N'_{\rm gal}(A')$, the number distribution of the galaxies located in the pixels of the extinction A', as follows.

Since we assume that the area of each pixel is the same and equal to $\Omega_{\rm pixel}$, the number of pixels that have the *true* extinction in the range of A and $A + dA$ is

$$N_{\rm pixel}(A)dA = \frac{\Omega(A)dA}{\Omega_{\rm pixel}}. \tag{D.9}$$

Thus the expected number distribution of galaxies in a pixel that suffers from the FIR contamination of ΔA is

$$\overline{N}(\Delta A) = \sum_{N=0}^{\infty} N P_{\rm joint}(\Delta A, N). \tag{D.10}$$

Therefore, the number distribution of galaxies, $N'_{\rm gal}(A')$, is given as

$$\begin{aligned}N'_{\rm gal}(A') &= \int_0^\infty dA \int_0^\infty d(\Delta A)N_{\rm pixel}(A)\overline{N}(\Delta A)\delta_D\big(A' - (A + \Delta A - \overline{\Delta A})\big) \\ &= \int_0^{A'+\overline{\Delta A}} d(\Delta A)N_{\rm pixel}(A' - \Delta A + \overline{\Delta A})\overline{N}(\Delta A).\end{aligned} \tag{D.11}$$

While the above expression is correct for those galaxies with $m_{\rm min} < m_{\rm true} < m_{\rm max}$, we cannot measure their true magnitude $m_{\rm true}$ in reality, and one has to take into account the selection effect carefully. Consider a galaxy of $m_{\rm true}$ is located in a pixel of the contaminated extinction of A'. Then its observed (uncorrected) magnitude is

$$m_{\rm uncorr}(A') = m_{\rm true} + A, \tag{D.12}$$

because its magnitude suffers from the true Galactic extinction A alone, instead of A'. This yields the *corrected* magnitude relying on the contaminated extinction A':

$$m_{\rm corr}(A') \;=\; m_{\rm uncorr}(A') - A' = m_{\rm true} + A - A' = m_{\rm true} - (\Delta A - \overline{\Delta A}) \quad \text{(D.13)}$$

leading to the *over-correction* by the amount of $\Delta A - \overline{\Delta A}$.

Therefore, those galaxies with $m_{\rm min} < m_{\rm corr}(A') < m_{\rm max}$ indeed correspond to

$$m_{\rm min} + (\Delta A - \overline{\Delta A}) < m_{\rm true} < m_{\rm max} + (\Delta A - \overline{\Delta A}). \quad \text{(D.14)}$$

In other words, the selection incorrectly excludes galaxies with $m_{\rm min} < m_{\rm true} < m_{\rm min} + \Delta A - \overline{\Delta A}$, and includes those with $m_{\rm max} < m_{\rm true} < m_{\rm max} + \Delta A - \overline{\Delta A}$ because of the contamination of FIR galaxy emission.

Given their differential number count with respect to magnitude, the number of such galaxies can be computed as

$$N_{\rm ex,corr}(\Delta A) \;=\; \int_{m_{\rm min}}^{m_{\rm min}+\Delta A-\overline{\Delta A}} \frac{dn(<m)}{dm} dm, \quad \text{(D.15)}$$

$$N_{\rm in,corr}(\Delta A) \;=\; \int_{m_{\rm max}}^{m_{\rm max}+\Delta A-\overline{\Delta A}} \frac{d\overline{n}(<m)}{dm} dm. \quad \text{(D.16)}$$

We adopt a power-law fit with a slope γ (see Fig. 5.1) for the differential number counts of galaxies in a pixel that contains N and $\overline{N}$ galaxies:

$$\frac{dn(<m)}{dm} \;=\; \frac{N\gamma 10^{\gamma m}\ln 10}{10^{\gamma m_{\rm max}} - 10^{\gamma m_{\rm min}}}, \quad \text{(D.17)}$$

$$\frac{d\overline{n}(<m)}{dm} \;=\; \frac{\overline{N}\gamma 10^{\gamma m}\ln 10}{10^{\gamma m_{\rm max}} - 10^{\gamma m_{\rm min}}}. \quad \text{(D.18)}$$

The excluded number should be normalized for the actual number of galaxies, N, instead of $\overline{N}$, in the pixel. Nevertheless the included number is not correlated to N in the Poisson distributed assumption, and thus should be normalized for $\overline{N}$.

Therefore we obtain finally the number distribution of galaxies after correcting for the contaminated extinction A' as

$$\begin{aligned} N'_{\rm gal,corr}(A') &= \int_0^\infty dA \int_0^\infty d(\Delta A) N_{\rm pixel}(A)[\overline{N}(\Delta A) - N_{\rm ex,corr}(\Delta A) + N_{\rm in,corr}(\Delta A)] \\ &\quad \times \delta_D\big(A' - (A + \Delta A - \overline{\Delta A})\big) \\ &= \int_0^{A'+\overline{\Delta A}} d(\Delta A) N_{\rm pixel}(A' - \Delta A + \overline{\Delta A})[\overline{N}(\Delta A) - N_{\rm ex,corr}(\Delta A) + N_{\rm in,corr}(\Delta A)]. \end{aligned} \quad \text{(D.19)}$$

Similarly, the number distribution of galaxies *before* correcting for the contaminated extinction A', *i.e.,* with $m_{\rm min} - A < m_{\rm true} < m_{\rm max} - A$, is given as

$$\begin{aligned} N'_{\rm gal,uncorr}(A') \;&=\; \int_0^\infty dA \int_0^\infty d(\Delta A) N_{\rm pixel}(A)[\overline{N}(\Delta A) - N_{\rm ex,uncorr}(A) + N_{\rm in,uncorr}(A)] \\ &\times\; \delta_D\big(A' - (A + \Delta A - \overline{\Delta A})\big), \end{aligned} \quad \text{(D.20)}$$

where

$$N_{\rm ex,uncorr}(A) = \int_{m_{\rm max}-A}^{m_{\rm max}} \frac{dn(<m)}{dm} dm, \tag{D.21}$$

and

$$N_{\rm in,uncorr}(A) = \int_{m_{\rm min}-A}^{m_{\rm min}} \frac{d\overline{n}(<m)}{dm} dm. \tag{D.22}$$

In order to proceed further, we need an expression for the PDF of the FIR contamination due to a single galaxy, $P_1(\Delta A)$. The mock simulations presented in §5.3 convert the r-band magnitude, m_r, of each mock galaxy into its 100 μm flux from the FIR/optical luminosity ratio y as

$$f_{100\mu{\rm m}}(m_r, y) = y f_0 10^{-0.4 m_r}, \tag{D.23}$$

where $f_0 = 3631$Jy, and y is assumed to obey the log-normal PDF $P_{\rm ratio}$ given by equation (5.4). In the present analytic model, we further assume that the differential number count of galaxies in r-band obeys

$$P_{\rm mag}(m_r) = \frac{\gamma_r 10^{\gamma_r m_r} \ln 10}{10^{\gamma_r m_{r,\rm max}} - 10^{\gamma_r m_{r,\rm min}}}, \tag{D.24}$$

where $m_{r,\rm max}$ and $m_{r,\rm min}$ denote the upper and lower limits of the magnitude, and γ_r is the power-law index.

Once $P_{\rm mag}(m_r)$ and $P_{\rm ratio}(y)$ are given, the PDF of 100μm flux from a single galaxy is computed as

$$P_{\rm flux}(f) \;=\; \int dy \int dm_r \; P_{\rm mag}(m_r) P_{\rm ratio}(y) \delta_D\big(f - f_{100\mu{\rm m}}(m_r, y)\big). \tag{D.25}$$

With the PDFs of equations (D.24) and (5.4), $P_{\rm flux}(f)$ reduces to

$$P_{\rm flux}(f) \;=\; K \left(\frac{f}{f_0}\right)^{-1-\frac{5}{2}\gamma_r} \left[{\rm erf}\big(s_{\rm max}(f)\big) - {\rm erf}\big(s_{\rm min}(f)\big)\right], \tag{D.26}$$

where ${\rm erf}(x)$ denotes the error function, and K, $s_{\rm max}$ and $s_{\rm min}$ are defined as

$$K \;\equiv\; \frac{5\gamma_r 10^{\frac{5}{2}\mu\gamma_r}}{4 f_0 (10^{\gamma_r m_{r,\rm max}} - 10^{\gamma_r m_{r,\rm min}})} \exp\left[\frac{25}{8}\sigma^2\gamma_r^2 (\ln 10)^2\right], \tag{D.27}$$

$$s_{\rm max}(f) \;\equiv\; \frac{1}{\sqrt{2\sigma^2}}\left[0.4 m_{r,\rm max} - \mu + \log_{10}\left(\frac{f}{f_0}\right) - \frac{5}{2}\sigma^2\gamma_r \ln 10\right], \tag{D.28}$$

$$s_{\rm min}(f) \;\equiv\; \frac{1}{\sqrt{2\sigma^2}}\left[0.4 m_{r,\rm min} - \mu + \log_{10}\left(\frac{f}{f_0}\right) - \frac{5}{2}\sigma^2\gamma_r \ln 10\right]. \tag{D.29}$$

Incidentally, $P_{\rm flux}(f)$ turns out to be well approximated by a log-normal function also, but we use equation (D.26) to be precise. Considering that the mock galaxies with flux larger than $f_{\rm lim}$ are removed and do not contaminate, $P_1(\Delta A)$ is calculated as

$$P_1(\Delta A) = \delta_D(\Delta A) \int_{f_{\rm lim}}^{\infty} P_{\rm flux}(f) df + \frac{1}{C}\Theta(C f_{\rm lim} - \Delta A) P_{\rm flux}\left(\frac{\Delta A}{C}\right), \tag{D.30}$$

where $C \equiv k_r p/\Omega_{\rm pix,eff}$ is a conversion factor from the FIR flux to the r-band extinction. We adopt $\Omega_{\rm pix,eff} = 2\pi\sigma_{\rm eff}^2$ as the effective area of a pixel, where $\sigma_{\rm eff}$ is the Gaussian width corresponding to the effective angular resolution, which is given in Appendix C. We adopt equation (C.7) for calculating $\Omega'(A')$, and (C.10) for $N'(A')$.

Acknowledgements

I would like to express my deepest gratitude to my supervisor, Yasushi Suto, who introduced me to the research of the Galactic extinction map, for all his warm supports. He always encouraged and supported me, and provided me with highly sophisticated views of science. It was very fruitful and stimulating to have discussions with him. I also appreciate Jun'ichi Yokoyama, Naoki Yoshida, Takashi Hosokawa, and Masamune Oguri, who showed me keen insights as physicists.

I am gratefully acknowledge my collaborators, Atsushi Taruya, Issha Kayo, Takahiro Nishimichi and Kazuhiro Yahata. Atsushi Taruya and Issha Kayo spared much time for discussions with me, and gave me many invaluable advices. Takahiro Nishimichi provided me with his cosmological N-body simulation data and many helpful comments. Kazuhiro Yahata helped me to understand the SDSS data structure and gave me many advices for our analysis.

I am also thankful to all the current and former members of the UTAP (University of Tokyo Theoretical AstroPhysics) and RESCEU (Research Center for the Early Universe) for their supports, educations, and providing inspiring environment. I would like to express special thanks to Ayuki Kamada, Masato Shirasaki, Gen Chiaki, and Akira Oka, who shared much time with me chatting over various topics on astrophysics. Thierry Sousbie sometimes taught me how to use the graphics software, Yorick.

I would also acknowledge Brice Ménard, Guangtun Zhu, Bruce T. Draine, and David Spergel for fruitful discussions during my stay at Johns Hopkins University and Princeton University. I deeply thank Kengo Tomida for his warm support at Princeton University. I thank Michael Kotson and Alice Giroul, who were summer students from MIT and The University of Glasgow, for their collaboration and a fun time we spend during the periods.

Finally, I would like to express my special thanks to all my friends, my former roommates, and my family for all their warm supports.

Funding for the creation and distribution of the SDSS Archive has been provided by the Alfred P. Sloan Foundation, the Participating Institutions, the National Aeronautics and Space Administration, the National Science Foundation, the U.S. Department of Energy, the Japanese Monbukagakusho, and the Max Planck Society. The SDSS Web site is http://www.sdss.org/. This work was supported by World Premier International Research Center Initiative (WPI Initiative), MEXT, Japan.

Data analysis were in part carried out on common use data analysis computer system at the Astronomy Data Center, ADC, of the National Astronomical Observatory of Japan.

References

Abazajian, K., et al. 2003, AJ, 126, 2081

Abazajian, K., et al. 2004, AJ, 128, 502

Abazajian, K. N., et al. 2009, AJ, 182, 543

Adelman-McCarthy, J. K., et al. 2006, ApJS, 162, 38

Aguirre, A. N. ApJL, 1999, 512, 19

Arce, H. G., & Goodman, A. A. 1999a, ApJ, 517, 264

Arce, H. G., & Goodman, A. A. 1999b, ApJL, 512, L135

Bennett, C. L, *et al.* 2003, ApJ, 583, 1

Berry, M., Ivezić, Ž., Sesar, B., et al. 2012, ApJ, 757, 166

Binney, J., & Merrifield, M. 1998, *Galactic Astronomy* (Princeton, NJ: Princeton University Press)

Blanton, M. R., et al. 2005, ApJ, 629, 143

Blanton, M. R., et al. 2005, ApJ, 631, 208

Bohlin, R. C., Savage, B. D., & Drake, J. F. 1978, ApJ, 1978, 224, 132

Bohren, C., F., & Huffman, D., R. 1983, *Absorption and Scattering of Light by Small Particles* (New York: Wiley)

Burstein, D., & Heiles, C. 1978, ApJ, 225, 40

Burstein, D., & Heiles, C. 1982, AJ, 87, 1165

Cambrésy, L., et al. 2001, A&A, 375, 999

Cambrésy, L., Jarrett, T. H., & Beichman, C. A. 2005, A&A, 435, 131

Cardelli, J. A., Clayton, G. C., & Mathis, J. S. 1988, ApJL, 329, L33

Cardelli, J. A., Clayton, G. C., & Mathis, J. S. 1989, ApJ, 345, 245

Chen, B., et al. 1999, A&A, 352, 459

Chelouche, D., Koester, B. P., & Bowen, D. V. 2007 ApJ, 671, 97

Chilingarian, I. V., Melchior, A.-L., & Zolotukhin, I. Y. 2010, MNRAS, 405, 1409

Clemens, M. S., Negrello, M., De Zotti, G. et al. MNRAS, 2013, 433, 695

Connolly, A. J., et al. 2002, ApJ, 579, 42

Cooray, A., & Sheth, R. Phys. Rep., 2002, 372, 1

Dobashi, K., Uehara, H., Kandori, R., et al. 2005, PASJ, 57, 1

Dodelson, S., Natayanan, V. K., Tegmark, M., Scranton, R., et al. 2002, ApJ, 572, 140

Draine, B. T., & Lee, H. M. 1984, ApJ, 285, 89

Draine, B. T. 2004, Astrophysics of Dust in Cold Clouds, *The Cold Universe*, (Saas-Fee Advanced Course 32, Springer-Verlag), astro-ph/0304488

Draine, B. T., & Li, A. 2007, ApJ, 657, 810

Draine, B., T. 2011, *Physics of the Interstellar and Intergalactic Medium* (Princeton, NJ: Princeton University Press)

Draine, B., T, et al, 2014, ApJ, 780,172

Dunne, L, et al. 2011, MNRAS, 417, 1510

Faber, S. M., et al. 1989, ApJS, 69, 763

Fang, W., et al. 2011, Phys. Rev. D, 84, 063012

Finkbeiner, D. P., Davis, M., & Schlegel, D. J. 2000, ApJ, 544, 81

Finkbeiner, D. P., et al. 2004, AJ, 128, 2577

Fitzpatrick, E. L. 1999, PASP, 111, 63

Fukugita, M., Ichikawa, T., Gunn, J. E., et al. 1996, AJ, 111, 1748

Fukugita, M., et al. 2004, AJ, 127, 3155

Gardner, J. P., Brown, T. M., & Ferguson, H. C., 2000, ApJ, 542, 79

Geller, M., J., & Huchra, J., P. 1989, Science, 246, 897

Green, G., M., Schlafly, E., F., Finkbeiner, D., P. et al. 2014, ApJ, 783, 114

Gunn, J. E., Carr, M., Rockosi, C., Sekiguchi, M., et al. 1998, AJ, 116, 3040

Gunn, J. E., Siegmund, W. A., Mannery, E. J., Owen, R. E., et al. 2006, AJ, 131, 2332

Gutierrez, C. M., & Lopez-Corredoira, M. 2014, astro-ph/1409.1125

Hamilton, T.S., Casertano, S., & Turnshek, D.A. 2010, ApJ, 678, 22

Hartmann, D., & Burton, W. B. 1997, *Atlas of Galactic Neutral Hydrogen* (Cambridge, UK: Cambridge University Press)

Heiles, C. 1975, A&A, 20, 37

Hogg, D. W., Finkbeiner, D. P., Schlegel, D. J., & Gunn, J. E. 2001, AJ, 122, 2129

Holwerda, B. W., Keel, W. C., Williams, B., Dalcanton, J. J., & de Jong, R. S., 2009, AJ, 137, 3000

Hubble, E., P. 1936, *The Realm of the Nebulae* (New Haven: Yale University Press)

van de Hulst, H., C. 1957, *Light Scattering by Small Particles* (New York: John Wiley & Sons)

Ivezić, Ž., Lupton, R. H., Schlegel, D., et al. 2004, Astronomische Nachrichten, 325, 583

Jarrett, T. H., et al. 2000, AJ, 119, 2498

Kaneda, H., Yamagishi, M., Suzuki, T., & Onaka, T. 2009, ApJ, 698, 125

Kashiwagi, T., Yahata, K., & Suto, Y., 2013, PASJ, 65, 43

Kashiwagi, T., et al. 2015, ApJ, 799, 132

Kashiwagi, T., & Suto, Y. 2015, submitted to MNRAS

Kitayama, T., et al. 2009, ApJ, 695,1191

Kohyama, T. et al. ApJ, 719, 873

Krügel, E. 2003, *The Physics of Interstellar Dust* (The Institute of Physics, Bristol, UK: IOP Series in Astronomy and Astrophysics)

Landy, S. D., & Szalay, A. S. 1993, ApJ, 412, 64

Laor, A., & Draine, B., T. 1993, ApJ, 402, 441

Letawe, Y., Letawe, G., & Magain, P. 2010, MNRAS, 403, 2088

Lee, Y. S., et al. 2008, AJ, 136, 2022

Li, A. & Draine, B. T. 2001, ApJ, 554, 778

Madau, P., & Pozzetti, L. 2000, MNRAS, 312, 9

Mathis, J., S., Rumpl, W., & Nordsieck, K., H. 1977, ApJ, 217, 425

Mathis, J., S., Mezger, P., G., & Panagia, N. 1983, A&A, 128, 212

McGee, S. L., & Balogh, M, L. 2010 MNRAS, 405, 2069

Ménard, B., Scranton, R., Fukugita, M., & Richards, G. 2010, MNRAS, 405, 1025

Ménard, B., Kilbinger. M., & Scranton, R. 2010b, MNRAS, 406, 1815

Mie, G. 1908, Annalen der Physik, 330, 377

Montier, L. A., & Giard, M. 2005, A&A, 439, 35

Mörtsell, E. 2013, A&A, 550, 80

Muller, S., et al. 2008, ApJ, 680, 975

Muñoz-Mateos, J. C., Gil de Paz, A., Boissier, S. et al. 2009, ApJ, 701, 1965

Murakami, H., et al. 2007, PASJ, 59, 369

Nishimichi, T., et al. 2009, PASJ, 61, 321

O'Donnell, J. E. 1994, ApJ, 422, 158

Padmanabhan, N., et al. 2008, ApJ, 674, 1217

Peek, J. E. G., & Graves, G. J. 2010, ApJ, 719, 415

Peek, J. E. G., Ménard, B., & Corrales, L. 2014, astro-ph/1411.3333

Pier, J. R., et al. 2003, AJ, 125, 1559

Richards, G. T., et al. 2004, ApJS, 155, 257

Richards, G. T., et al. 2009a, ApJS, 180, 67

—. 2009b, AJ, 137, 3884

Rowles, J., & Froebrich, D. 2009, MNRAS, 395, 1640

Saunders, W., et al. 2000, MNRAS, 317, 55

Savage, B. D., & Mathis, J. S. 1979, ARA&A, 17, 73

Schlafly, E. F., et al. 2010, ApJ, 725, 1175

Schlafly, E. F., & Finkbeiner, D. P. 2011, ApJ, 737, 103

Schlafly, E., F, Green, G., Finkbeiner, D. P. et al. 2014, ApJ, 789, 15

Schlegel, D. J., Finkbeiner, D. P., & Davis, M. 1998, ApJ, 500, 525

Scranton, R., et al. 2002, ApJ, 579, 48

Scranton, R., et al. 2005, ApJ, 633, 589

Serjeant, S., & Harrison, D. 2005, MNRAS, 356, 192

Smith, J. A., Tucker, D. L., Kent, S., et al. 2002, AJ, 123, 2121

Stanek, K., Z. 1998, astro-ph/9802093

Stickel, M., et al. 1998, A&A, 329, 55

Stickel, M., Klaas, U., Lemke, D., & Mattila, K. A&A, 2002, 383, 367

Stoughton, C., et al. 2002, AJ, 123, 485

Strateva, I., et al. 2001, AJ, 122, 1861

Strauss, M. A., et al. 2002, AJ, 124, 1810

Takeuchi, T. T., Yoshikawa, K., & Ishii, T. T. 2003, ApJL, 587, L89

Tauber, J. A., *et al.* 2010, A&A, 520, A1

Tian, H.-J., Liu, C., Hu, J.-Y., Xu, Y., & Chen, X.-L. 2014, A&A, 561, 142

Tucker, D. L., Kent, S., Richmond, M. W., et al. 2006, Astronomische Nachrichten, 327, 821

Weingartner, J. C., & Draine, B. T. 2001, ApJ, 548, 296

Wheelock, S. L. et al. 1994, IRAS Sky Survey Atlas: Explanatory Supplement, JPL Publication 94-11 (Pasadena: JPL)

Wright, E. L., et al. 2010, AJ, 140, 1868

Xu, C., K., Donas, J., Arnouts, S., et al. 2005, ApJ, 619, 11

Yahata, K. 2007, PhD thesis, The University of Tokyo

Yahata, K., et al. 2007, PASJ, 59, 205

Yamada, K., & Kitayama, T. 2005, PASJ, 57, 611

Yasuda, N., Fukugita, M., & Schneider, D. P. 2007, AJ, 134, 698

Yasuda, N., et al. 2001, AJ, 122, 1104

York, D. G., et al. 2000, AJ, 120, 1579

Zaritsky, D. 1994, AJ, 108, 1619

Zehavi, I., Zheng, Z., Weinberg, D. H., et al. 2011, ApJ, 736, 59

Zwicky, F. in McVittie G. C., ed., Proc. IAU Symp. 15, Problems of Extra-Galactic Research. Macmillan, New York, p. 347